Instanton Correlations

in the Finite Temperature QCD Vacuum

by

Fernando Pérez

B.S. Physics, Universidad de Antioquia, 1995.

M.Sc. Physics, Universidad de Antioquia, 1999.

A thesis submitted to the

Faculty of the Graduate School of the

University of Colorado in partial fulfillment

of the requirements for the degree of

Doctor of Philosophy

Department of Physics

2002

This thesis entitled:
Instanton Correlations
in the Finite Temperature QCD Vacuum
written by Fernando Pérez
has been approved for the Department of Physics

_____

Anna Hasenfratz

_____

Thomas A. DeGrand

Date _____

The final copy of this thesis has been examined by the signatories, and we find that
both the content and the form meet acceptable presentation standards of scholarly
work in the above mentioned discipline.

Pérez, Fernando (Ph.D., Physics)

Instanton Correlations
    in the Finite Temperature QCD Vacuum

Thesis directed by Professor Anna Hasenfratz

Instantons, discovered in 1975, are solutions to the Euclidean-space classical equations of Quantum Chromodynamics (QCD). They have been found to play a crucial role in many low energy phenomena driven by the strong interactions. Instantons are the leading candidate for explaining spontaneous chiral symmetry breaking, and they provide a mechanism for fermion propagation in the QCD vacuum.

At finite temperature, QCD is expected to undergo a transition into a chirally symmetric phase known as a quark-gluon plasma. In lattice calculations with dynamical fermions, the instantons are expected to form 'molecules', polarized in the time direction. In this work, we study finite temperature lattice configurations and find evidence for this structure by analyzing the two-point charge correlator. We also present tools that we developed for visualizing numerical data from lattice calculations.

Dedicated to Irene González.

For a lifetime of friendship which has changed me like no other.

Acknowledgements

To my fellow graduate students Chet Nieter and Archie Paulson, for their friendship in and out of physics. I would also like to thank Chet for the code used for generating artificial instanton configurations.

To Germán Vélez and Lucas Monzón, for they are proof that exceptional friendships make all the difference in life.

To my parents, for feeding my dreams with the best of examples, and for supporting those dreams in all situations.

And finally to my incredible wife Adriana, who has never stopped being by my side or believing in me.

Contents

Figures

Figure

Tables

Table

Chapter 1

Introduction

Quantum Chromodynamics (QCD) is the leading theory of the strong interactions; it describes hadrons as composite objects built out of elementary fermions called the *quarks* interacting via gauge bosons known as the *gluons*. While the mathematical formalism of QCD is well grounded in the framework of Yang-Mills gauge theories as an $SU(3)$ local gauge theory, we are today far from being able to extract full quantitative predictions from it. The dimensionless gauge coupling of QCD runs from small values at very high energies to large values at lower energies, limiting the range where perturbation theory studies are of use.

One of the most fascinating aspects of QCD is the structure of its vacuum. Because QCD is based on a non-abelian gauge group, even in the absence of fermion fields the vacuum is a very complex object built out of self-interacting gauge fields. These interactions allow the gauge fields to form very non-trivial structures with wide-ranging impact on hadron phenomenology.

In 1975, a particular configuration of gauge fields known today as the *instanton* was discovered by Belavin *et al.* [8]. Instantons, inherently non-perturbative objects, are 'lumps' of gauge fields, localized in space and time and protected by topological symmetries. They can be interpreted physically as tunneling solutions between topologically inequivalent vacua of the gauge background. The discovery of instantons prompted a flurry of research activity, as it was soon found that they had a strong influence on the behavior of fermions.

Today we understand the propagation of quarks in the gauge vacuum as a process of 'hopping' from one instanton to another. Instantons are the leading contender for the mechanism behind the spontaneous breaking of chiral symmetry. Indeed, many of the low-energy properties of QCD are thought to be in one form or another the consequence of the complex interplay between instantons and fermions.

The thermodynamics of QCD is also a very interesting topic. At low temperatures QCD exhibits a phenomenon known as *confinement*, which means that we never observe color charges by themselves (in particular, isolated quarks have never been observed). At very high temperatures, we expect however the theory to undergo a transition into a phase known as a quark-gluon plasma. In the QGP phase, color charges act as free particles and there are no bound hadrons, only a combined mixture of quarks and gluons with a number of interesting features.

While the QGP has not been experimentally observed yet, much progress has been made in recent years with the advent of the Relativistic Heavy Ion Collider (RHIC) facility at Brookhaven National Laboratory. The high-energy collisions between heavy ions at RHIC create conditions where we expect to see signatures of the QGP phase, and there is much work in progress to analyze this data.

We know that at zero temperature chiral symmetry is spontaneously broken in QCD (at zero quark mass), and as we said the instantons are the leading candidate for explaining this phenomenon. As we turn the temperature up and go into the QGP phase, chiral symmetry is restored. There are many hints which suggest that instantons may also be responsible for this restoration of chiral symmetry, through an interesting interplay with the fermions. In this work we will attempt to look at this question using numerical techniques.

In the last 20 years, a method known as Lattice QCD, which consists of representing the theory on a discrete Euclidean space time grid, has emerged as the only candidate for a full exploration of the non-perturbative regime of QCD. While this method allows us to maintain exactly the key gauge symmetry of the theory, it

breaks other symmetries (notably Lorentz invariance) and is computationally very expensive. For these reasons we are still far from being able to compute quantities from QCD to arbitrarily high precision, although much progress has been made in recent years.

In this thesis, we will use lattice calculations to explore the structure of the QCD vacuum at finite temperature. In particular we will look at whether the mechanisms suggested for driving the chiral transition via instantons are supported by the numerical evidence. Our work is organized as follows. In Chapter 2 we present an outline of the structure of QCD as a Yang-Mills quantum field theory; in Chapter 3 we present in detail the method of lattice QCD; in Chapter 4 we discuss instantons in the continuum; in Chapter 5 we present the issues which arise when dealing with topological objects on the lattice; in Chapter 6 we discuss the thermodynamics of QCD and the expected phenomena related to instantons at finite temperature; in Chapter 7 we discuss our analysis of the instanton structure in lattice calculations.

Since lattice calculations are done on a 4-dimensional grid, the resulting data is not particularly convenient to analyze. While one is often interested in aggregate quantities which depend only on one or two variables, there are a number of situations where it would be of interest to be able to look directly at the gauge and fermionic quantities on the 4-d lattice. In Chapter 8 we present a set of tools we developed for this purpose, and use them to look at some particularly interesting quantities connected to the rest of our work. Finally, in Chapter 9 we discuss our results and the outlook of this line of inquiry for future research.

Chapter 2

QCD - The Theory of Strong Interactions

The currently established theory which describes the fundamental interactions of the constituents of nature, excluding gravity, is known as the Standard Model. It has the structure of a Yang-Mills gauge theory and is a combination of the Glashow-Salam-Weinberg model for the electroweak interactions described by an $SU(2) \times U(1)$ group with the strong interactions based on an $SU(3)$ group. In this chapter we will present a brief outline of the QCD framework, mainly with the intent of establishing the terminology and notation.

2.1 Quarks

After the successes of physics in the 1940s and 50s in building nuclear models in terms of basic constituents (the proton and the neutron), evidence began to accumulate in favor of a similar picture for the nucleons themselves. Amongst other issues, the rapidly rising number of 'elementary' particles being produced in increasingly powerful particle accelerators in the 1950s was becoming a conceptual sore in the framework of physics. An idea similar to the organization of the periodic table in terms of a few basic blocks (nucleons and electrons) was needed.

In the early 1960s Gell-Mann and Zweig proposed that the observed spectrum of elementary particles could be described in terms of irreducible representations of an $SU(3)$ group. This idea gained strong support when the Ω^- particle was detected at Brookhaven National Laboratory in 1964 with precisely the expected

properties, and at that point Gell-Mann proposed to give the basic elements of the fundamental representation of $SU(3)$ physical reality, calling them *quarks* (a word taken from James Joyce's *Finnegan's Wake*). The quarks were proposed to be spin 1/2 particles with fractional electric charges of $\pm 1/3, \pm 2/3$ in units of e, as needed to account for the fact that nucleons (made from three quarks) were fermions with integer charges.

It soon became obvious that the quark model of hadrons would require another quantum number, because states with otherwise identical quantum numbers were found, in violation of Pauli's exclusion principle. This quantum number was called *color* and it was also governed by an $SU(3)$ group. However, in contrast to the original global $SU(3)$ flavor group of the quark model, the color $SU(3)$ was proposed[1] as a *local* gauge symmetry. Its eight generators appear physically as the gauge bosons, the carriers of the color interactions. Because they are really what 'glues' the nucleons together, these eight gauge bosons are known as the *gluons*.

Phenomenologically, the strong interactions exhibit an interesting balance of opposites. For a long time, deep inelastic scattering experiments hinted that the *short distance* behavior of QCD was similar to that of a theory of nearly free quarks, a behavior known as *asymptotic freedom*. At the opposite end of the distance scale, the observed behavior is strikingly different. Despite exhaustive experimental searches, no free quark, neither any object carrying color charge, has ever been found. It appears that at long distances, the QCD coupling is so strong that it prevents the constituent quarks from wandering on their own. This phenomenon is known as *confinement*.

These are some of the boundary conditions that any successful theoretical model of the strong interactions must satisfy. In the 1970s, phenomenological models based on asymptotic freedom and confinement as starting assumptions, were fairly

---

[1] Deep inelastic experiments gave evidence for asymptotic freedom, known to be a possible feature of Yang-Mills theories. Since the color symmetry had no other obvious physical significance, it was proposed as the local gauge symmetry for the quarks.

successful. One such theory, the MIT bag model, allowed fairly detailed predictions for some properties of the light hadrons ([14], [21]). The bag model postulated that the quarks behaved as weakly interacting relativistic fermions confined to a finite region of space. From there it was able to make quantitative predictions for light hadron spectroscopy. However, a full explanation of these features from first principles is required.

Today we have experimental evidence for the existence of six quarks instead of the original three in Gell-Mann's days, so the flavor $SU(3)$ structure is only an approximate description valid for the lighter hadrons. However, the color $SU(3)$ model remains as the leading theory of strong interactions, and we have confidence it will provide a description of the known phenomenology.

2.2   Mathematical Outline of QCD

QCD is a theory which describes the interactions of six spin $1/2$ fermions –the quarks– via gauge bosons known as gluons. The six quarks, in increasing mass order, are known as: up (u), down (d), strange (s), charm (c), bottom (b) and top (t). The Lagrangian for QCD has the usual form of any Yang-Mills theory based on a non-Abelian gauge group, $SU(3)$ in this case. $SU(3)$ has eight generators, and their standard form in the fundamental representation is known as the Gell-Mann λ matrices. These are Hermitian, traceless 3×3 matrices which satisfy the group algebra

$$[\lambda_a, \lambda_b] = 2if_{abc}\lambda_c, \tag{2.1}$$

where f_{abc} are the $SU(3)$ structure constants. The λ matrices are normalized according to

$$\mathrm{Tr}[\lambda_a\lambda_b] = 2\delta_{ab}. \tag{2.2}$$

Further details on the properties of $SU(3)$ can be found in any standard reference on the subject ([33], [59]).

To each of the generators λ_a we associate a set of local gauge fields $A_\mu^a(x)$ from which we construct

$$A_\mu(x) = \frac{1}{2} \sum_{a=1}^{8} \lambda_a A_\mu^a(x). \tag{2.3}$$

Using these we can then build the gluon field strength tensor as

$$F_{\mu\nu} = \partial_\mu A_\nu - \partial_\nu A_\mu - ig[A_\mu, A_\nu], \tag{2.4}$$

where g is the dimensionless bare coupling constant for QCD, the only free gauge parameter of the theory.

The fermionic part of the action will be built from quark fields. Each is a color $SU(3)$ triplet with the common labels (r, g, b) for the colors:

$$\psi(x) = \begin{pmatrix} \psi_r(x) \\ \psi_g(x) \\ \psi_b(x) \end{pmatrix}. \tag{2.5}$$

With these elements we can then write the full QCD Lagrangian as

$$\mathcal{L} = -\frac{1}{2} \operatorname{Tr}(F_{\mu\nu} F^{\mu\nu}) + \sum_{f=1}^{N_f} \bar{\psi}_f (p_\mu + g A_\mu) \gamma^\mu \psi_f - m_f \bar{\psi}_f \psi_f, \tag{2.6}$$

where N_f is the number of quark flavors under consideration at a given energy scale, and γ^μ are the usual Dirac matrices.

The full Standard Model Lagrangian will include this QCD Lagrangian, the electroweak terms, and the coupling terms between the quarks and the other sectors of the theory.

Table 2.1: Basic interactions in the Standard Model.

Name	Gauge Boson	Range	Strength
Weak Force	$W^{\pm}$, Z^0 (3)	$< 10^{-17}$ m	10^{-5}
Electromagnetism	Photon, γ (1)	Long: $F \sim r^{-2}$	1/137
Strong Force	Gluons, g (8)	10^{-15} m	1

Table 2.1 summarizes some details of the various components of the Standard Model. Of particular interest to us is the last column, which gives the order of magnitude of the dimensionless coupling constant for each interaction. The size of the QCD coupling means that perturbative expansions are of limited use.

Asymptotic freedom can be understood by looking at the high momentum (short distance) behavior of the QCD coupling constant. We will not go into the full details of a renormalization analysis of this constant here. Let us only state that for an $SU(3)$ Yang-Mills theory with one dimensionless coupling constant, one can show that at short distances the coupling constant runs to zero, providing effectively a free theory. A complete discussion of this topic can be found in any textbook on quantum field theory or QCD ([59], [33]).

A naïve approach would suggest that an extension of the asymptotic freedom argument is enough to explain confinement. Since the renormalization group analysis tells us that the QCD coupling runs asymptotically to zero at high energies, one could assume that in the opposite limit, it will run to large values at low energies (long distances). However, the asymptotic freedom argument is a perturbative one based on a small-coupling expansion of the β function. There is no reason to assume that this behavior is maintained monotonically at larger values of the coupling.

For a complete understanding of confinement, as well as other features of the theory, we need a way to directly probe the non-perturbative regime of QCD. In the next chapter we will present an outline of Lattice QCD, the only known method today which can tackle the full non-perturbative structure of Yang-Mills gauge theories.

Chapter 3

QCD on the Lattice

We have seen that QCD is a theory where perturbative studies are of limited utility, yet we do not have any known method for obtaining analytic solutions to the full QCD equations. The Lattice QCD approach was developed to address this problem, by discretizing the theory on a space-time grid and computing the required quantities at any value of the coupling constant. Since the introduction of a finite grid turns the continuous equations into a finite system, numerical methods can be used to compute the solutions with computers. In practice there remain a number of significant obstacles to be overcome even today, but the lattice approach has proved very useful, and remains to this day the only way to study the full non-perturbative regime of QCD.

In the rest of this chapter we will briefly present the basic elements of the lattice approach to QCD, following the lines of the introductory presentations [18], [34], [55] and [22]. More details can be found therein or in the comprehensive [66].

3.1   The Path Integral Formulation

Once we write the quantities we are interested in computing from our theory in the form of vacuum expectation values (VEVs) of operators, we need a way to explicitly calculate these expectation values. In order to set up a non-perturbative solution method for QCD, we begin by writing these in the language of Feynman path integrals.

We start with an operator $\mathcal{O}$, where $\mathcal{O}$ is any combination of operators expressed in terms of time-ordered products of gauge and quark fields. The VEV $\langle 0| \mathcal{O} |0 \rangle$ we are interested in, where $|0\rangle$ represents the vacuum state for the free theory, is given by

$$\langle 0| \mathcal{O} |0 \rangle = \frac{\int \mathcal{D}A_\mu \mathcal{D}\psi \mathcal{D}\bar{\psi}\, \mathcal{O}(\psi, \bar{\psi}, A) e^{-S}}{\int \mathcal{D}A_\mu \mathcal{D}\psi \mathcal{D}\bar{\psi}\, e^{-S}}, \tag{3.1}$$

where S is the action, the integral of the Lagrangian density

$$S = \int d^4x\, \mathcal{L}, \quad \mathcal{L} = \frac{1}{4}F_{\mu\nu}F^{\mu\nu} - \bar{\psi}M\psi, \tag{3.2}$$

and M is the Dirac operator. These expressions are valid in Euclidean space-time, where after a rotation of the time axis $(t \to i\tau)$ the oscillatory factors e^{iS} become the numerically more manageable e^{-S}.

We should mention that in Euclidean space, our vacuum expectation values have exactly the structure of thermal expectation values in statistical mechanics. A quantum field theory in Euclidean space-time (with N spatial and one time dimensions) can be connected to a classical statistical system in $N+1$ spatial dimensions in thermal equilibrium with a heat reservoir. This correspondence is in fact extremely useful [59], as it provides new sources of intuition and methods for quantum field theory from statistical mechanics, and vice-versa. In recent years, Wilson's renormalization group ideas (originally developed in the context of second order phase transitions, [85], [86]) have been extremely useful in quantum field theory, and in particular in lattice QCD ([23], [24], [20], [43]).

In Eq. (3.2) the fermionic fields, represented by the Grassman variables ψ and $\bar{\psi}$, can be integrated out exactly so that the above partition function becomes

$$Z = \int \mathcal{D}A_\mu \det M\, e^{\int d^4x\, \left(-\frac{1}{4}F_{\mu\nu}F^{\mu\nu}\right)}. \tag{3.3}$$

This expression, although exact, introduces a numerical difficulty: the term $\det M$ is a highly non-local expression whose evaluation is computationally expensive. One therefore often resorts to the approximation known as *quenching*, which consists of setting $\det M = \text{const}$ and whose physical meaning is to ignore vacuum polarization effects from the QCD vacuum.

Except for the possible approximation of quenching, Eq. (3.1) is an exact expression. But it represents an infinite-dimensional functional integral, an object whose measure is not well defined. The lattice approach consists of discretizing the space-time continuum as a 4-dimensional grid where the fermion and gauge fields live. On this finite grid, the measure of the Feynman Path Integral becomes a well defined object. We can then proceed to compute the resulting large but finite-dimensional integrals using numerical methods.

3.2   Gauge Symmetry

Since local gauge symmetry is one of the cornerstones of the very structure of QCD, it is important that any computational approach implements it exactly. As we will see, it is indeed possible to put QCD on a discrete lattice while fully respecting local gauge invariance. This is in contrast with Lorentz invariance, which is broken at any finite lattice spacing and is only restored in the continuum limit.

Since the geometrical role played by the gauge fields is to serve as connections between different space-time points (or physically, the gluons carry the interaction between fermions at different locations), it seems sensible to locate them on the links between lattice points. Indeed, the lattice formulation of QCD puts all quark fields on sites of the lattice, and all gluon fields on the links between those sites.

In the continuum, a fermion moving in space from x to y in the presence of

a gauge background $A_\mu(x)$ picks up a phase factor given by the path ordered product

$$\psi(y) = \mathcal{P}e^{\int_x^y igA_\mu(x)dx_\mu}\psi(x). \qquad (3.4)$$

The $\mathcal{P}$ symbol represents the path ordering operator, which defines the exponential so that matrices evaluated closer to y stand to the left and those closer to x stand to the right.

To each lattice gauge field, Wilson [87] proposed to associate a discrete version of Eq. (3.4)

$$U(x, x + \hat{\mu}) \equiv U_\mu(x) = e^{iagA_\mu(x + \frac{\hat{\mu}}{2})} \qquad (3.5)$$

where $\hat{\mu}$ is a unit vector in the μ direction and a is the lattice spacing. From this definition, U is a member of the $SU(3)$ group and it satisfies the path ordering condition

$$U(x, x - \hat{\mu}) \equiv U_{-\mu}(x) = e^{-iagA_\mu(x - \frac{\hat{\mu}}{2})} = U^\dagger(x - \hat{\mu}, x). \qquad (3.6)$$

Under a local gauge transformation $V(x) \in SU(3)$, the variables $\psi(x)$ and U transform as

$$\begin{aligned} \psi(x) &\rightarrow V(x)\psi(x), \\ \bar{\psi}(x) &\rightarrow \bar{\psi}(x)V^\dagger(x), \\ U_\mu(x) &\rightarrow V(x)U_\mu(x)V^\dagger(x + \hat{\mu}), \end{aligned} \qquad (3.7)$$

where $V(x)$ is in the same representation as the U. There are then two ways of constructing objects which are automatically gauge invariant:

(1) An open line made from a path-ordered product of links ($U_\mu(x)$ at various

x), terminated by a fermion and an antifermion at its endpoints, such as

$$\bar{\psi}(x)U_\mu(x)U_\nu(x+\hat{\mu})\ldots U_\rho(y-\hat{\rho})\psi(y). \qquad (3.8)$$

(2) Any closed loop. The simplest example of this (and the basic building block of the gauge action on the lattice) is the plaquette, a 1×1 loop of the form

$$W_{\mu\nu}^{1\times1} = \mathrm{Re}\ \mathrm{Tr}\ (U_\mu(x)U_\nu(x+\hat{\mu})U_\mu^\dagger(x+\hat{\nu})U_\nu^\dagger(x)). \qquad (3.9)$$

In $SU(N \geq 3)$ the trace of any closed loop is complex, with the two possible path orderings giving complex conjugate values.

In the above the trace over color indices is necessary in order to guarantee the gauge invariance of the final object. This can be seen by considering a single path ordered loop $U(y,y)$ which begins and ends at point y. From Eq. (3.7), it transforms as

$$U(y,y) \rightarrow V(y)U(y,y)V^\dagger(y), \qquad (3.10)$$

but once we take its trace, using the cyclic symmetry of the trace we obtain

$$\mathrm{Tr}\ U(y,y) \rightarrow \mathrm{Tr}\ U(y,y). \qquad (3.11)$$

Using closed loops and fermion-bracketed lines, we can then construct a representation of any physically interesting operator for our theory. This form guarantees that gauge invariance is inherently preserved even at non-zero lattice spacing a. This gives us considerable freedom in choosing how to represent the operators of the continuum theory. We must only ensure that whichever lattice form we choose reduces to the continuum form in the limit $a \rightarrow 0$. We can then adapt the lattice representation to improve the properties of our operators at finite a with respect to other symmetries of the continuum which *are* broken on the lattice.

3.3 The Lattice Action

First we take a look at the gauge part of the action. By expanding the plaquette to first order in a one can show that

$$\frac{1}{g^2} \sum_x \sum_{\mu < \nu} \text{Re Tr}(1 - W_{\mu\nu}^{1\times1}) \sim \int d^4x F_{\mu\nu} F^{\mu\nu} \tag{3.12}$$

and taking the specific numerical factors of $SU(3)$ into account we can then write the QCD gauge action as

$$S_G = \beta \sum_x \sum_{\mu < \nu} \text{Re Tr}(1 - W_{\mu\nu}^{1\times1}); \quad \beta = \frac{6}{g^2}. \tag{3.13}$$

The action S_G has the correct continuum limit but includes discretization errors of $O(a^2)$. This problem can be addressed systematically by adding suitably weighed terms to the action which respect the continuum limit which cancel the corrections at a given order[72].

The fermionic continuum action is given by

$$S_F = \int d^4x \bar{\psi}(x)[\gamma^\mu \partial_\mu + m]\psi(x). \tag{3.14}$$

Its simplest discretization, known as the naïve quark action, is

$$S_F^N = \sum_x \bar{\psi}(x) M_{xy}^N \psi(y) \tag{3.15}$$

where the interaction matrix M^N is

$$M_{xy}^N = m\delta_{xy} + \frac{1}{2a} \sum_\mu [\gamma_\mu U_{x,\mu} \delta_{x,y-\mu} - \gamma_\mu U_{x-\mu,\mu}^\dagger \delta_{x,y+\mu}], \tag{3.16}$$

and

$$U_{x,\mu} \equiv U_\mu(x) \in SU(3). \tag{3.17}$$

The action S_F, just like its gauge counterpart (3.13), is correct in the limit $a \to 0$ but it has discretization errors at any finite a.

Furthermore, S_F suffers from a particularly vexing problem commonly referred to as *fermion doubling*. This problem is immediately apparent when one considers the behavior of the two-point function or propagator:

$$G_N(x,y) \equiv \left\langle \bar{\psi}(x)\psi(y) \right\rangle. \tag{3.18}$$

The propagator is easiest to compute in momentum space, by Fourier transforming the action (3.15) with all $U_\mu(x) = 1$. The resulting (inverse) is, for the naïve discretization, given by:

$$G_N^{-1}(p) = i\gamma^\mu \frac{\sin(p_\mu a)}{a} + m, \tag{3.19}$$

which we need to compare with the continuum inverse propagator:

$$G_F^{-1}(p) = i\gamma^\mu p_\mu + m. \tag{3.20}$$

These two propagators coincide in the $p \to 0$ limit, but (3.19) has unfortunately other zeros at the edges of the Brillouin zone, at $p = \pm\pi/a$ (in each spatial dimension). This problem is illustrated in Fig. 3.1, where we plot the dispersion relation for both the continuum and the naïve actions. Physically, the result is that for each spatial dimension, we find not one but *two* modes which behave like a small momentum, continuum-like fermion. Therefore in normal four dimensional lattice calculations we end up with $2^4 = 16$ fermions instead of one.
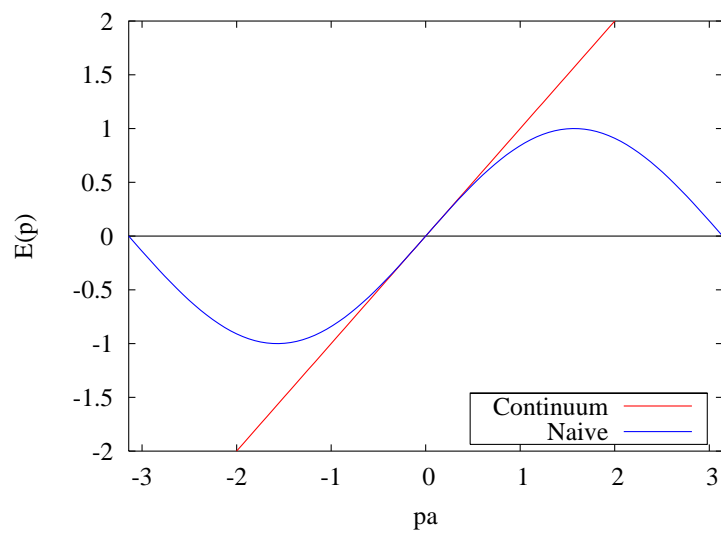
Figure 3.1: Dispersion relation for the continuum action and the naïve discretization, along a momentum axis. The extra zeros at the edges of the Brillouin zone appear as extra fermions.

There are multiple ways of addressing the fermion doubling problem. The simplest approach is known as the Wilson action, and while it has fairly severe side effects, it is still the most popular quark action for many applications. An additional term is added to the action which gives the doublers a mass much larger than ma so they effectively decouple from the system in the continuum limit $a \to 0$. The new term is a second derivative which gives us the action

$$S_F^W \quad = \quad S_F^N - \frac{r}{2} a^5 \sum_x \bar{\psi}_x \Box \psi_x, \tag{3.21}$$

$$\Box \psi_x \quad = \quad \frac{1}{a^2} \sum_\mu \psi_{x+\hat{\mu}} - 2\psi_x + \psi_{x-\hat{\mu}}, \tag{3.22}$$

where r is a free non-zero parameter (usually $r = 1$). For this action the propagator is

$$G_W^{-1}(p) \quad = \quad G_N^{-1}(p) + \frac{2r}{a^2} \sum_\mu \sin^2(p_\mu a/2) \tag{3.23}$$

$$\xrightarrow[p \to 0]{} \quad i\gamma^\mu p_\mu + m + \frac{ra}{2} \sum_\mu p_\mu^2 \tag{3.24}$$

and it has the right form for the low momentum ($p \sim 0$) mode. But for the doublers, an expansion around $\tilde{p} \approx \pi/a$ gives us

$$G_W^{-1}(\tilde{p}) = i\gamma^\mu p_\mu + m + \frac{2r}{a} + \ldots \tag{3.25}$$

so as $a \to 0$ the mass of the doublers increases and they decouple. This can be seen by plotting the dispersion relation for the Wilson action, shown in Fig. 3.2 for $r = 1$ (which should be contrasted to Fig. 3.1).

The Wilson action has $O(a)$ discretization artifacts and thus requires fine lattices. Additionally, it has the problematic side effect of explicitly breaking chiral symmetry even at zero quark mass. This is not an accident, but in fact a consequence of the Nielsen-Ninomiya no-go theorem [57], which in summary states that for a
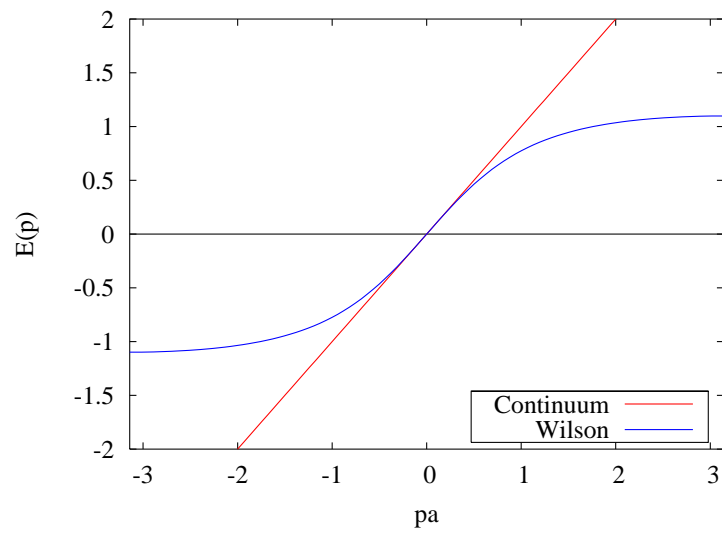
Figure 3.2: Dispersion relation for the continuum action and the Wilson discretization, along a momentum axis. The Wilson action shows no extra zeros in the Brillouin zone.

fermionic lattice action of the general form

$$S_F = a^4 \sum_{m,n} \bar{\psi}(m) D(m-n) \psi(n) \tag{3.26}$$

the following four conditions can *not* all be met simultaneously:

(1) $D(n)$ is local (bounded by $Ce^{-\gamma|n|}$)

(2) $\tilde{D}(p) = i\gamma^\mu p_\mu + O(ap^2)$ for $p \ll \pi/a$. (Correct continuum limit).

(3) $\tilde{D}(p)$ is invertible for $p \neq 0$. (No doublers).

(4) $\gamma_5 D + D\gamma_5 = 0$. ($D$ is chirally symmetric).

The Wilson action respects (1)-(3) but at the price of breaking chiral symmetry. There exist more complex actions which try to maintain properties (1)-(3) while breaking chiral symmetry in the mildest and most controlled ways possible, at the expense of explicit forms which are much more complicated and expensive to simulate. Most of these approaches rely on a discovery by Ginsparg and Wilson ([32]) which shows exactly how much of chiral symmetry can be preserved on the lattice.

3.4 The Lattice as a Regulator

QCD is a renormalizable quantum field theory, therefore in practical calculations we must devise a suitable scheme for controlling the UV divergences. On the lattice, the spacing a acts as a natural cutoff, as it restricts the momenta to the range $[-\frac{\pi}{a}, \frac{\pi}{a}]$. In this sense, lattice calculations are therefore 'complete', as they require no perturbative approximations or additional renormalizations.

At this point one may ask whether the introduction of the lattice spacing a into our calculations is an extraneous new parameter. In fact a renormalization

group analysis shows that a and the coupling g are related by

$$\Lambda_{QCD} = \lim_{a \to 0} \frac{1}{a} e^{-1/2\beta_0 g^2(a)} [\beta_0 g^2(a)]^{-\beta_1/2\beta_0^2} \tag{3.27}$$

where Λ_{QCD} is the dynamically generated mass scale of QCD, and (β_0, β_1) are the first two, scheme-independent coefficients of the β-function. In practice one specifies only g (or β), and must later calibrate the calculation to extract the physical value of the lattice spacing. In Sec. 3.6.1 we outline this procedure.

3.5 Simulations

3.5.1 Markov Chains and Monte Carlo Methods

The calculation of a quantity such as (3.1) on a space-time lattice with roughly 10^4 points involves on the order of 4×10^4 link variables. For the $SU(3)$ group, each of these variables is a function of 8 real parameters ($N^2 - 1$ for $SU(N)$), so we need to perform roughly 320000 integrations. Even with an efficient quadrature algorithm capable of computing these integrals accurately on a coarse 10 point grid, the functional integral on the lattice would be a sum of roughly 10^{320000} terms. This is simply impossible to perform in a finite amount of time.

The observation that most configurations in (3.1) will have a large action and will therefore contribute very little –if at all– to the integral, points to a solution. If instead of adding all the terms in the series we limit ourselves to a statistically significant sample, generated with a probability distribution given by the Boltzmann factor $e^{-S[U]}$, we can obtain a good approximation to the integral in a vastly shorter time. This is the technique known as *importance sampling*, and all the methods based on this idea are collectively known as *Monte Carlo methods*. We will now outline the basic ideas behind these methods and present some of the more relevant ones to lattice calculations. A more detailed presentation can be found in [66].

Let $C_1, C_2, \ldots$ denote a countable set of configurations of our system. Then,

consider a stochastic process in which a sequence of configurations is generated such that the transition probability for going from C_i to C_j is $P(C_i \rightarrow C_j) \equiv P_{ij}$. The state of our system at any time[1] is thus a random variable which depends only on the state immediately preceding it, as long as the transition probability is independent of the system's past history. Such a sequence is known as a *Markov chain*, and there are a number of theorems for Markov chains which provide the basis for Monte Carlo methods.

In particular, a Markov chain is called irreducible if, starting from an arbitrary configuration C_i, there is a finite probability of reaching any other configuration C_j in a finite number of steps N. That is, there is a finite N such that

$$P_{ij}^{(N)} = \sum_{\{i_k\}} P_{ii_1} P_{i_1 i_2} \ldots P_{i_{N-1} j} \neq 0. \tag{3.28}$$

For an irreducible chain[2] it can be shown that the limit $N \rightarrow \infty$ of (3.28) exists:

$$\lim_{N \rightarrow \infty} P_{ij}^{(N)} = \pi_j \tag{3.29}$$

where $\{\pi_j\}$ are numbers which satisfy

$$\pi_j = \sum_i \pi_i P_{ij}, \tag{3.30}$$

$$\sum_j \pi_j = 1. \tag{3.31}$$

Furthermore, the time average

$$\langle \mathcal{O} \rangle_N = \frac{1}{N} \sum_{i=1}^N \mathcal{O}(C_i) \tag{3.32}$$

---

[1]Time here refers to the discrete variable which indexes the configuration sequence, not to the physical time which the equations for our system may depend on.

[2]With a few additional conditions, see [66] for details.

approaches the ensemble average

$$\langle \mathcal{O} \rangle = \sum_i \pi_i \mathcal{O}(C_i) \tag{3.33}$$

with a statistical uncertainty of order $O(1/\sqrt{N})$.

These results allow us to define for an arbitrary configuration C a finite probability for the system to eventually reach it. This is the *equilibrium* probability for C :

$$P_{eq}(C) = \sum_{C'} P_{eq}(C')P(C' \to C) \,, \tag{3.34}$$

and the expectation value $\langle \mathcal{O} \rangle$ can then be computed as

$$\langle \mathcal{O} \rangle = \sum_C P_{eq}(C)\mathcal{O}(C) \tag{3.35}$$

where we've dropped the individual configuration subscripts.

In order to devise a calculation method based on this, we need to determine what the transition probability for our Markov process will be, so that the expectation value (3.35) generated from the Markov sequence of states is an approximation to (3.1). One can show that a sufficient (but not necessary) condition for a Markov process to sample the distribution $\exp(-S[C])$ is that the transition probability satisfies the *detailed balance* condition

$$e^{-S[C]}P(C \to C') = e^{-S[C']}P(C' \to C) \tag{3.36}$$

for every pair of configurations C and C'.

The detailed balance condition does *not* uniquely specify what the transition probability must be. This freedom can be exploited to design algorithms which can be efficient under various conditions or address specific problems of a simulation.

We will briefly review the most common methods used in lattice QCD calculations which, while satisfying detailed balance, try to tackle various aspects of the QCD problem differently.

3.5.2 Overview of Methods

<u>Heat Bath</u>

The heat bath method is the most straightforward implementation of the idea of importance sampling. Suppose we want to compute a one-dimensional integral

$$\langle F \rangle = \int_a^b dx \, F(x) P(x) \tag{3.37}$$

where $P(x)$ is a properly normalized probability distribution satisfying $\int_a^b dx P(x) = 1$. This problem can be recast in the form of one with a uniform distribution with a simple change of variables. If we define y through the following boundary value problem:

$$\frac{dy}{dz} = P(z) \tag{3.38}$$

$$y(a) = 0 \tag{3.39}$$

$$y(b) = 1, \tag{3.40}$$

we can then write

$$y(x) = \int_a^x dz \, P(z), \tag{3.41}$$

and (3.37) can be written as

$$\langle F \rangle = \int_0^1 dy \, F(x(y)). \tag{3.42}$$

This change amounts to turning y into a uniformly distributed variable in the $[0, 1]$ interval. In terms of y we can now compute the expectation value $\langle F \rangle$ through (3.42) by simply generating uniform random numbers on that interval.

This method is straightforward conceptually, but in practice not often useful as it requires being able to compute the change of variable integral (3.41). If that integral can be analytically computed (which is rarely the case), the method provides a convenient approach, but if one must resort to computing it numerically for each value of x then it proves to be of little practical value. For such cases other methods are in fact more appropriate.

Metropolis

This method is in principle applicable to any system, regardless of the analytical properties of the probability distribution describing it. If C is a configuration to be updated, a new configuration C' is computed with a transition probability $P_0(C \to C')$ which only needs to satisfy the microreversibility condition

$$P_0(C \to C') = P_0(C' \to C). \tag{3.43}$$

Once the new configuration is available, we must decide whether to update the system to it or to keep the old one. This decision is made as follows:

(1) If $e^{-S(C')} > e^{-S(C)}$, i.e. if the new action is lower than the old one, the new configuration C' is kept and the system is updated.

(2) Otherwise, a random number r uniformly distributed in $[0, 1]$ is chosen and the system is updated only if

$$r \leq \frac{e^{-S(C')}}{e^{-S(C)}} \tag{3.44}$$

Condition 1 allows the system to lower its action, heading towards the classical solution. But condition 2 also takes into account quantum fluctuations which raise

the action, albeit moderated with a probability distribution $e^{-S(C')}/e^{-S(C)}$. It is straightforward to prove that this algorithm satisfies the detailed balance condition (see [66] for details).

In practice, a configuration for a statistical system is updated by changing only one variable at a time. The reason for this, which at first appears to be slower than changing the entire system at once, is that global updates would cause in general large changes in the action, drastically lowering the acceptance rate and thus slowing down the algorithm. The algorithm can also slow down even for single-variable updates, if the action depends non-locally on the coordinates (because the calculation of $e^{-S(C')}/e^{-S(C)}$ becomes an expensive operation). This is particularly important for lattice QCD when fermions are to be considered, and is one of the reasons why algorithms allowing full lattice updates in one step were developed.

Molecular Dynamics

This algorithm is based on a microcanonical ensemble construction of the partition function for a statistical system. The key idea of the method is the connection between the Euclidean path integral formulation of a quantum field theory and the partition function for a mechanical statistical system in four spatial dimensions. For this new system, a Hamiltonian is constructed which evolves with a new 'time' variable, the simulation time.

We will outline the method considering a scalar theory whose action $S[\phi; \beta]$ depends on a scalar field ϕ and a coupling parameter β in the form

$$S[\phi; \beta] = \beta V[\phi] , \tag{3.45}$$

as is the case for pure gauge theories. As always, we are interested in computing an expectation value

$$\langle \mathcal{O} \rangle = \frac{1}{Z} \int \mathcal{D}\phi \, \mathcal{O}[\phi] e^{-S[\phi; \beta]}, \tag{3.46}$$

where

$$Z = \int \mathcal{D}\phi \, e^{-S[\phi;\beta]} \, . \tag{3.47}$$

At this point we assume that a discrete space-time lattice has been introduced to compute the above integrals as sums, and we will label all the degrees of freedom through a collective index i which denotes the lattice site coordinates.

In order to cast this into the language of classical statistical mechanics, we introduce a set of canonically conjugate momenta π_i with which we define a Hamiltonian for the system as

$$H[\phi, \pi; \beta] = \frac{1}{2} \sum_i \pi_i^2 + V[\phi], \tag{3.48}$$

and a partition function

$$\bar{Z} = \int \mathcal{D}\phi \mathcal{D}\pi \, e^{-\beta H[\phi,\pi]}. \tag{3.49}$$

With the introduction of a discrete lattice, the functional integration measure becomes

$$\mathcal{D}\phi \mathcal{D}\pi = \prod_i d\phi_i d\pi_i, \tag{3.50}$$

and we can compute $\langle \mathcal{O} \rangle$ as

$$\langle \mathcal{O} \rangle = \frac{1}{\bar{Z}} \int \mathcal{D}\phi \mathcal{D}\pi \mathcal{O}[\phi] e^{-\beta H[\phi,\pi]} \, . \tag{3.51}$$

This form, while providing the value for $\langle \mathcal{O} \rangle$ we are seeking, has the structure of a *thermal* expectation value for a statistical system in contact with a heat reservoir.

At this point we can use the standard result from statistical mechanics [58] which, in the thermodynamic limit, connects expectation values computed in the

canonical and microcanonical ensembles:

$$\langle \mathcal{O} \rangle_{\text{can}}(\beta) = \langle \mathcal{O} \rangle_{\text{mic}}(E = \bar{E}(\beta)), \tag{3.52}$$

where

$$\langle \mathcal{O} \rangle_{\text{mic}}(E) = \frac{1}{Z_{\text{mic}}(E)} \int \mathcal{D}\phi \mathcal{D}\pi \mathcal{O}[\phi] \delta(H[\phi, \pi] - E), \tag{3.53}$$

$$Z_{\text{mic}}(E) = \int \mathcal{D}\phi \mathcal{D}\pi \delta(H[\phi, \pi] - E). \tag{3.54}$$

The connection between the coupling parameter β and the energy value $\bar{E}$ at which we fix microcanonical calculations can be obtained via the equipartition theorem to be

$$\frac{N}{2\beta} = \langle T_{\text{kin}} \rangle_{\text{mic}}(\bar{E}), \tag{3.55}$$

where T_{kin} is the kinetic energy of the system and N is the total number of degrees of freedom.

Now that we have rewritten our thermal expectation values as fixed-energy ones, we make the assumption that if the motion generated by the Hamiltonian (3.48) is ergodic, then we can integrate the equations of motion induced by it and replace ensemble averages by time averages over the resulting phase-space trajectories on the $E = \bar{E}$ energy shell.

Note that this algorithm has two key assumptions built into it, which are in fact rather problematic:

(1) The number of degrees of freedom is infinite (the canonical-microcanonical ensemble equivalence of expectation values is only valid in the thermodynamic limit),

(2) The motion generated by the Hamiltonian (3.48) is ergodic.

Furthermore, the integration of the equations of motion will necessarily introduce a finite time-step in the calculation, which is a source of systematic errors.

These difficulties led to the development of the Hybrid Monte Carlo method.

Hybrid Monte Carlo

The Hybrid Monte Carlo (HMC) method is based on combining an extension to the Molecular Dynamics method known as the Hybrid algorithm with a Metropolis acceptance step. The Hybrid algorithm [29] addresses problem 2 cited above by replacing the momenta $\{\pi_i\}$ by random variables with a probability density

$$P(\{\pi_i\}) = \left(\prod_i \frac{1}{\sqrt{2\pi}} \right) e^{-\frac{1}{2}\sum_i \pi_i^2} . \tag{3.56}$$

Instead of integrating the equations of motion as in the molecular dynamics method along a single trajectory of fixed energy $\bar{E}$, the integration is occasionally interrupted and a new set of momenta distributed according to (3.56) is introduced. This injects ergodicity into the system; however the problem of the systematic errors arising from integrating the equations of motion with a finite time step remains.

The next refinement consists of using the phase space configurations generated as a result of the Molecular Dynamics integration (with the Hybrid stochastic correction) as trial configurations for a Metropolis accept/reject step. If we start with a configuration which has energy $H[\phi, \pi]$ and after integrating for a certain number of time steps the configuration has energy $H[\phi', \pi']$, then the new one will be accepted with probability

$$p = \min\{1, e^{-H[\phi',\pi']}/e^{-H[\phi,\pi]}\} . \tag{3.57}$$

Of course, since the system is conservative, if we could integrate the equations of motion exactly the energy would be perfectly constant along any trajectory and the new configuration would always be accepted by the Metropolis test. However, for

any finite time step we have in general $\delta H \neq 0$, and the role of the Metropolis test is then to remove the systematic errors while satisfying the detailed balance condition.

A detailed description of the HMC algorithm suitable for implementation purposes can be found in [66].

3.5.3 Monte Carlo Methods for Systems with Fermions

As previously discussed, lattice calculations are often implemented using the quenched approximation. This is done mainly because the computational cost of not doing so is extremely high, but also because for certain problems the quenched approximation is indeed sufficient. On the other hand, there is nothing *in principle* which prevents explicitly including fermions in simulations. Since the QCD action is quadratic in the fermionic fields, we can always integrate them out from the exponential and include their contribution via the resulting determinant.

In order to outline how this can be done, let us begin by rewriting the full action for Wilson fermions (3.21). After absorbing the lattice spacing into dimensionless quantities, the interaction matrix is explicitly given by:

$$M_{ij}^W[U] = (m_q + 4r)\delta_{ij} - \frac{1}{2}\sum_\mu [(r - \gamma_\mu U_{i,\mu})\delta_{i,j-\mu} + (r + \gamma_\mu U_{i-\mu,\mu}^\dagger)\delta_{i,j+\mu}], \quad (3.58)$$

so the fermionic part of the action is explicitly

$$S_F^W[U,\psi,\bar\psi] = \sum_{i,j,f} \bar\psi_i^f M_{ij}^W[U]\psi_j^f, \qquad (3.59)$$

and the full action reads:

$$S[U,\psi,\bar\psi] = S_G[U] + S_F^W[U,\psi,\bar\psi]. \qquad (3.60)$$

Let $\langle \mathcal{O}[U,\psi,\bar\psi] \rangle$ be the expectation value of an operator which depends

both on the gauge fields U and the fermionic variables $(\psi, \bar{\psi})$. Its explicit form is

$$\langle \mathcal{O} \rangle = \frac{\int \mathcal{D}\bar{\psi}\mathcal{D}\psi\mathcal{D}U\,\mathcal{O}[U,\psi,\bar{\psi}]e^{-S[U,\psi,\bar{\psi}]}}{\int \mathcal{D}\bar{\psi}\mathcal{D}\psi\mathcal{D}e^{-S[U,\psi,\bar{\psi}]}}. \tag{3.61}$$

The quadratic form in (3.61) can be explicitly integrated for fermionic variables (represented by Grassman numbers) as

$$\int \mathcal{D}\bar{\psi}\mathcal{D}\psi e^{-S_F^W} = (\det M^W)^{N_f}, \tag{3.62}$$

where N_f is the total number of active flavors. We can then write

$$\langle \mathcal{O} \rangle = \frac{\int \mathcal{D}U\,\langle \mathcal{O} \rangle_{S_F}\,e^{-S_{\text{eff}}[U]}}{\int \mathcal{D}U e^{-S_{\text{eff}}[U]}}, \tag{3.63}$$

with

$$\langle \mathcal{O} \rangle_{S_F} = \frac{\int \mathcal{D}\bar{\psi}\mathcal{D}\psi\,\mathcal{O}[U,\psi,\bar{\psi}]e^{-S_F^W[U,\psi,\bar{\psi}]}}{\int \mathcal{D}\bar{\psi}\mathcal{D}\psi\mathcal{D}e^{-S_F^W[U,\psi,\bar{\psi}]}}, \tag{3.64}$$

$$S_{\text{eff}} = S_G[U] - \ln(\det M^W[U])^{N_f}. \tag{3.65}$$

With a proper choice of the Wilson parameter r, M^W can be shown to be positive definite for even N_f. This enables us to write

$$\left(\det M^W[U]\right)^{N_f} = (\det Q[U])^{N_f/2}, \tag{3.66}$$

with

$$Q[U] = (M^W[U])^\dagger M^W[U]. \tag{3.67}$$

Using (3.66) we can then express (3.65) as

$$S_{\text{eff}}[U] = S_G[U] - \frac{N_f}{2}\ln\det Q[U]. \tag{3.68}$$

At this point suppose we try to calculate $\langle \mathcal{O} \rangle$ with (3.63) with any algorithm which includes a Metropolis acceptance test. If we are comparing two background gauge field configurations U and U' then we will need to compute the difference in the action $S_{\text{eff}}[U'] - S_{\text{eff}}[U]$. This requires computing the ratio

$$\rho(U, U') = \frac{\det Q[U']}{\det Q[U]}. \tag{3.69}$$

And therein lies the difficult problem with fermions in lattice simulations: the determinant is a global quantity and $Q[U]$ is a large matrix, so the exact computation of $\rho(U, U')$ on anything but the smallest lattices would slow down any simulation to a crawl, since it would have to be done at each step of the process.

A number of ideas have been proposed to address this vexing problem. Since dynamical fermion simulations are not the focus of this thesis, we will only outline here the general approach behind these methods. The idea is to introduce sets of auxiliary fields (ϕ, ϕ^*), which can be used to construct approximate expressions for $\det Q$.

Once these auxiliary fields have been introduced, one can set up a Hybrid Monte Carlo calculation for fermions in a manner similar to what we described in Sec. 3.5.2. Basically, we introduce the canonical momenta π_i, π_i^* and P_l conjugate to ϕ_i, ϕ_i^* and A_l respectively, where A_l are the group gauge variables. This gives us a Hamiltonian controlling the dynamics of our new statistical system in the Monte Carlo simulation time τ:

$$H = \frac{1}{2} \sum_l P_l^2 + \sum_i \pi_i^* \pi_i + S_G[U] + S_{AUX}[U, \phi, \phi^*], \tag{3.70}$$

where S_{AUX} is the contribution to the action from the auxiliary fields.

At this point, we can then follow the HMC outline presented above; more details can be found in [66] and references therein. We should note that simulations with dynamical fermions tax the limits of existing computer technology, and the

development of better algorithms is thus an active area of research.

3.6   Measurements on the Lattice

In this section we will describe how the calculations performed according to the methods we have previously presented can be used to compute quantities of physical interest.

3.6.1   Comparing with the Continuum

Computers deal only with pure numbers, not with physical, dimensionful quantities. Therefore all calculations done on the lattice treat and return dimensionless values. When we compute a mass m on the lattice, we are in fact obtaining the dimensionless product $\hat{m} = ma$, where a is the lattice spacing. As discussed in Sec. 3.4, there is an internal (renormalization-driven) connection between the coupling constant β and the lattice spacing. This means that once we have numbers coming out from a lattice calculation done at a certain value of β, we must *calibrate* the calculation. This means obtaining the physical value of the lattice spacing a and other input parameters (such as the quark masses), which in turn will determine the scale for all other numbers extracted from the calculation.

The calibration process is performed by choosing a set of physical quantities with known values and comparing them to their lattice values. Ideally this would set the scale uniquely and every other quantity could then be written in MeV, but as usual, there are problems which arise from the various approximations made on the lattice [22]. The string tension is one observable often chosen for this calibration process, because it has a fairly clean and direct expression in terms of lattice quantities through the measurement of the Wilson loop.

One particular difficulty of matching lattice results with physical numbers is illustrated by Eq. (3.4). For any arbitrary operator $\mathcal{O}$ we are measuring (such as the string tension) with mass dimension $d_{\mathcal{O}}$, let us write $\hat{\mathcal{O}}(g_0)$ to denote the

dimensionless value measured on the lattice. If we work with the assumption that a continuum limit exists at all, so that as $a \to 0$ the quantities take their physical values (once properly calibrated), then dimensional analysis tells us that

$$\mathcal{O}(g_0(a), a) = \left(\frac{1}{a}\right)^{d_\mathcal{O}} \hat{\mathcal{O}}(g_0) \xrightarrow[a \to 0]{} \mathcal{O}_{\text{physical}}. \tag{3.71}$$

For the calibration to be reliable (in the sense that the process is reasonably independent from the operator used for the calibration) we need quantities to scale according to the above expression. In practice this only happens in a limited region of bare couplings, since for too small g_0 the physical volume itself (the total number of lattice points is constrained by computer power) becomes too small and finite volume errors dominate. On the other hand increasing g_0 increases a and the lattice becomes too coarse to accurately represent the short-range physics. The region where the relation (3.71) is satisfied is known as the scaling window, and practical calculations are performed within it.

3.6.2 Spectroscopy

If we believe QCD to be the correct theory of the strong interactions, then we expect to be able to predict from it the mass spectrum of the hadrons, amongst other things. These quantities are well measured experimentally and should always be a first check for any lattice calculation. In fact, if lattice QCD had failed to predict these masses satisfactorily, either the lattice approach or the very theory of QCD itself would have come into question.

Although this thesis does not deal directly with spectroscopy issues, they are such a basic component of the lattice approach that a few paragraphs regarding on how they are handled are warranted. Many more details can be found in the literature.

The basic idea behind all spectroscopy calculations is to compute the expec-

tation value of an operator with the quantum numbers of the state one is interested
in, and then to extract its mass eigenvalue by taking advantage of the exponential
suppression of higher-energy states in the long time limit.

Let us specifically illustrate this with the problem of computing the mass
of the pion [34]. We choose as our operator of interest the fourth component of the
axial current $\mathcal{O} = A_4 = \bar{\psi}\gamma_4\gamma_5\psi$ which has a large coupling to the pion, and compute
the 2-point function $\langle 0| T[\sum_x \mathcal{O}(\mathbf{x}, t)\mathcal{O}(\mathbf{o}, 0)] |0\rangle$. In standard quantum mechanical
fashion, this correlator is the probability amplitude for the creation of a state (in
fact, all states in the spectral decomposition of $\mathcal{O}$) with the quantum numbers of
the pion at point $(\mathbf{o}, 0)$, evolving via the QCD Hamiltonian in space time until its
annihilation at $(\mathbf{x}, t)$.

Because we are working in Euclidean space-time, a given eigenstate of $\mathcal{O}$
with energy E has a weight e^{-Et}. We can then write the eigenstate decomposition

$$\langle 0| T[\sum_x \mathcal{O}(\mathbf{x}, t)\mathcal{O}(\mathbf{o}, 0)] |0\rangle = \sum_n \frac{\langle 0| \mathcal{O} |n\rangle \langle n| \mathcal{O} |0\rangle}{2E_n} e^{-E_n t} \tag{3.72}$$

where we have used the Lorentz-invariant normalization

$$\langle n |n'\rangle = 2E_n \delta_{nn'}, \tag{3.73}$$

$$1 = \sum_n \frac{1}{2E_n} |n\rangle \langle n| . \tag{3.74}$$

Now we try to extract information about the pion at rest. The first step is to make
a zero-momentum projection so that $E_n \to M_n$. This is accomplished by the spatial
integral (discrete sum on the lattice) $\sum_x$. Next we try to be as specific with our
construction of $\mathcal{O}$ as possible so that its spectral decomposition resolves only the
pion (ideally $\mathcal{O}$ would be exactly the quantum mechanical wavefunction of the pion).
And finally we look at the asymptotic time behavior of the correlation function,
where the higher mass states (radial excitations of the pion, three pions with total

$J = 0$, etc.) have been exponentially suppressed relative to the ground state:

$$\langle 0| T[\sum_{x} \mathcal{O}(\mathbf{x}, t)\mathcal{O}(\mathbf{o}, 0)] |0\rangle \xrightarrow[t\to\infty]{} \frac{\langle 0| \mathcal{O} |\pi\rangle \langle\pi| \mathcal{O} |0\rangle}{2M_\pi} e^{-M_\pi t}. \tag{3.75}$$

From an exponential fit to the large t data for our 2-point function we can then extract the mass eigenvalue we are interested in.

Let us finally mention how the above expectation value is expressed in terms of the quantities actually computed on the lattice. We are interested in computing

$$\langle 0| T[\sum_{x} \mathcal{O}(\mathbf{x}, t)\mathcal{O}(\mathbf{o}, 0)] |0\rangle = \langle 0| \sum_{x} \bar{\psi}(\mathbf{x}, t)\gamma_4\gamma_5\psi(\mathbf{x}, t)\bar{\psi}(\mathbf{o}, 0)\gamma_4\gamma_5\psi(\mathbf{o}, 0) |0\rangle$$

$$\tag{3.76}$$

which by using Wick contractions can then be written as

$$= \langle 0| \sum_{x} G_{F\,\mathrm{Latt}}^{-1}(0; \mathbf{x}, t)\gamma_4\gamma_5 G_{F\,\mathrm{Latt}}^{-1}(\mathbf{x}, t; 0)\gamma_4\gamma_5 |0\rangle \tag{3.77}$$

where $G_{F\,\mathrm{Latt}}^{-1}$ is the lattice version of the Feynman quark propagator (3.20). Since on the lattice the Dirac operator becomes a finite (if large) matrix, this propagator is simply the inverse of the Dirac matrix, and it depends on the particular background gauge field configuration. In practical calculations, it is this matrix inversion step which consumes most CPU cycles, and large amounts of research effort has been spent in finding fast, numerically stable algorithms for this inversion. Most lattice codes today employ variants of a stabilized biconjugate gradient inverter for this purpose.

Chapter 4

Instantons in QCD

In 1975, Belavin and collaborators [8] (reprinted in [73]) found a class of exact, analytical solutions to the classical $SU(2)$ Yang-Mills equations which they called 'pseudoparticles'. These solutions are known today as BPST instantons (or simply instantons), and have been found to play a critical role in several aspects of QCD.

Instantons are a peculiar feature of non-Abelian theories, and they are fundamentally non-perturbative objects, as they involve long range structure in the gauge fields. For this reason they are essential components of several low-energy phenomena in QCD, such as the θ parameter, the problem of the η' mass, chiral symmetry breaking and confinement. The extent of their contribution to confinement is still not fully clear and appears to be less than initially hoped [1].

In this work we will only concern ourselves with instantons in the context of QCD. Since they are a feature of the gauge fields, instanton solutions do exist in the $SU(2)$ sector of the electroweak theory. However, their interplay with the Higgs sector gives rise to complications we will not discuss here.

In this chapter we will present an overview of the physics of instantons. For further reference, the collection [73] edited by M. Shifman is an excellent source which contains reprints of many key original papers on the topic, including two com-

---

[1]Interestingly, it was precisely the confinement problem what initially motivated Polyakov [63] to look at the kinds of gauge field configurations which eventually led to instantons and opened up this field.

prehensive reviews by Coleman [15] and by Vainshtein et. al. [81]. Bitar and Chang [11] present a detailed study of the vacuum tunneling interpretation of instanton solutions, and Shuryak gives in [75] a friendly discussion of hadron and instanton physics in the spirit of G. Gamow's famous books. For an extremely detailed discussion of most problems related to instantons, the review article [69] by Schafer and Shuryak is probably the most comprehensive reference available today. Other references for specific topics will be given in the text.

4.1 Topology and the QCD Vacuum

We will begin by informally presenting a few basic definitions from topology which are necessary for understanding the way instantons appear in QCD. Let f and g be continuous functions from a space X to a space Y. The function f is said to be *homotopic* to g, denoted $f \simeq g$, if there exists a continuous function $F : X \times [0, 1] \to Y$ such that $F(x, 0) = f(x)$ and $F(x, 1) = g(x)$ for all $x \in X$. Basically two functions are homotopic if they can be continuously deformed into one another.

If we now consider the set of all possible functions between X and Y, modulo homotopy equivalence, we have the set of homotopy classes $[X, Y]$. This is commonly known in the physical literature as the set of 'topologically inequivalent transformations between X and Y.' The set $[S^n, X]$, where S^n is the n-dimensional sphere, is called the nth *homotopy group of* X and is denoted by $\pi_n(X)$. The first homotopy group, $\pi_1(X)$, is known as the *fundamental group* of X; it is the set of all possible inequivalent mappings of the unit circle onto the space X.

Let us now present without proof a few basic results concerning homotopy groups. It can be shown that

$$\pi_1(S^1) = \mathbb{Z}, \tag{4.1}$$

which is illustrated by the family of functions

$$f_d(z) = z^d; \; z \in \mathbb{C}, \, d \in \mathbb{Z}. \tag{4.2}$$

These functions map the unit circle d times around itself. Any continuous function mapping the unit circle onto itself can be continuously deformed into one of the f_d functions, for some value of d.

Furthermore, it can be shown that a relation similar to (4.1) holds for higher dimensional spheres. In general it is true that

$$\pi_k(S^k) = \mathbb{Z} \quad \forall k \in \mathbb{N}. \tag{4.3}$$

This result will be particularly useful to us in the following discussion. While we do not prove it here, we can illustrate it for the $k = 2$ case with a family of functions of the form

$$g_d(\theta, \phi) = (\theta, d\phi), \, d \in \mathbb{Z} \tag{4.4}$$

where (θ, ϕ) are the usual spherical coordinate angles. Any map from S^2 to itself is homotopic to a member of this family for some value of d.

With these basic definitions behind us, let us now see why all of this is relevant to the problem of the QCD vacuum. Even though QCD is an $SU(3)$ gauge theory, our discussion here will focus on $SU(2)$ solutions; this is not a limitation because all known instanton solutions for $SU(3)$ are in fact $SU(2)$ instantons embedded in $SU(3)$. The question of the existence of 'pure' $SU(3)$ instantons with more complex features than those we will discuss, remains open at this time. We will have more to say about this issue below, once we clarify the topological structure of $SU(2)$ instantons.

Because of the non-Abelian character of the gauge group, the QCD vacuum

is a very complex and interesting environment, in spite of the absence of matter fields. The vacuum is the minimum energy state of the theory, and for pure gauge QCD obviously the trivial $A_\mu(x) = 0$ is such a solution. However, we can also look for non-trivial field configurations which have finite total action and are still local minima of the action:

$$\frac{\delta S[A]}{\delta A} = 0, \ S[A] < \infty. \tag{4.5}$$

We can identically rewrite the gauge action as

$$S = \frac{1}{8g^2} \int d^4x \{ [F_{\mu\nu}^a \mp \tilde{F}_{\mu\nu}^a]^2 \} \pm \frac{8\pi^2}{g^2} Q, \tag{4.6}$$

with

$$Q = \frac{1}{32\pi^2} \int d^4x \, F_{\mu\nu}^a(x) \tilde{F}_{\mu\nu}^a(x) \tag{4.7}$$

and the dual field tensor given by

$$\tilde{F}_{\mu\nu}^a = \frac{1}{2} \epsilon_{\mu\nu\alpha\beta} F_{\alpha\beta}^a. \tag{4.8}$$

With the above form, we see that in order to have a finite action, the field strength tensor must vanish on the surface of a large sphere of radius R, faster than R^{-3} :

$$F_{\mu\nu}^a(|x| = R) \xrightarrow[R\to\infty]{} 0, \tag{4.9}$$

which is equivalent to requiring the fields to be 'pure gauge' on the surface of the large sphere:

$$A_\mu(x) \xrightarrow[|x|=R\to\infty]{} iU(x)\partial_\mu U(x)^\dagger, \tag{4.10}$$

where $U(x) \in SU(2)$.

Now we look for ways of minimizing the action as written in (4.6). In this form, it is clear that we can obtain minima with an action $S \propto |Q|$ if there exist field configurations which satisfy

$$F^a_{\mu\nu} = \pm \tilde{F}^a_{\mu\nu}. \tag{4.11}$$

We will assume for the time being that such solutions can indeed be constructed. Now we need to consider the behavior of the quantity Q we defined above. By using Gauss's theorem we can rewrite the volume integral (4.7) as a surface integral:

$$Q = \frac{1}{32\pi^2} \int_{|x|=R} K_\mu dS_\mu, \tag{4.12}$$

where the field K_μ, known as the Chern-Simons current, is given by

$$K_\mu = 2\epsilon_{\mu\nu\alpha\beta}(A^a_\nu \partial_\alpha A^a_\beta + \frac{1}{3} f^{abc} A^a_\nu A^b_\alpha A^c_\beta). \tag{4.13}$$

This shows us that for field configurations satisfying the duality condition (4.11), the value of the action is uniquely determined by the asymptotic properties of the A_μ fields, and does not actually depend on their local structure. This can be proved in detail by computing the variation of Q under changes in the A_μ; this variation vanishes thanks to the asymptotic condition (4.9) [73].

Since we are working with pure gauge configurations, this means that ultimately we are interested in understanding the asymptotic behavior of the possible classes of gauge transformations $U(x)$. If

$$U(x) \xrightarrow[|x|=R\to\infty]{} 1, \tag{4.14}$$

then obviously

$$A_\mu(x) \xrightarrow[|x|=R\to\infty]{} 0, \tag{4.15}$$

and we have a trivial configuration with $Q = 0$. Now the question is whether other solutions can be found. Let us consider what happens on the surface of our sphere of radius R in 4-d space, S_R^3: we want to know what kinds of $U(x)$ functions can be constructed there besides the trivial identity. Using the terminology introduced earlier, this means precisely considering the 3rd homotopy group of our group space, $\pi_3(SU(2))$. But any $U \in SU(2)$ can be written as

$$U = A + i\sigma B, \ A^2 + B^2 = 1. \tag{4.16}$$

This means that the group space of $SU(2)$ is equivalent to the three dimensional unit sphere S^3, and the question we are asking is then the class of mappings:

$$S^3 \longrightarrow S^3 \tag{4.17}$$

$$\text{Spacetime sphere} \rightarrow SU(2) \text{ group space.} \tag{4.18}$$

In other words, we need to know what $\pi_3(S^3)$ is. Using (4.3), we have

$$\pi_3(S^3) = \mathbb{Z}. \tag{4.19}$$

This result is of critical physical significance: it tells us that in the gauge vacuum of $SU(2)$, there exists an infinity of topologically inequivalent configurations labeled by the integers, which are local minima of the action.

At this point we can obtain some physical insight into the definition of Q given in (4.7). Q is called the *topological charge,* and it has been normalized to correspond directly with the integer index which labels the configuration class. This

is in fact no accident, as the construction of such integer invariants for topological spaces is a standard problem of algebraic topology. Q is thus an integer which describes the global, gauge invariant properties of the gluon field background.

The key result of Belavin et.al. in 1975 was to find an explicit solution to (4.11) which corresponds to $Q = 1$, known today as the BPST instanton after the initials of the four authors of [8]. The instanton gauge fields are given by

$$A_\mu^a(x) = \frac{2\eta_{a\mu\nu} x_\nu}{x^2 + \rho^2},$$ (4.20)

where ρ is an arbitrary parameter which characterizes the spatial extent of the fields (we can think of it as a 'radius' for the instanton). In the above we introduced the 't Hooft symbol $\eta_{a\mu\nu}$

$$\eta_{a\mu\nu} = \epsilon_{a\mu\nu} + \delta_{a\nu}\delta_{\nu 4} - \delta_{a\mu}\delta_{\mu 4}.$$ (4.21)

The anti-instanton solution with $Q = -1$ can be obtained by replacing $\eta_{a\mu\nu}$ with the dual 't Hooft symbol $\bar{\eta}_{a\mu\nu}$, given by

$$\bar{\eta}_{a\mu\nu} = \epsilon_{a\mu\nu} - \delta_{a\nu}\delta_{\nu 4} + \delta_{a\mu}\delta_{\mu 4}.$$ (4.22)

For these solutions the field strength is

$$(F_{\mu\nu}^a)^2 = \frac{192\rho^4}{(x^2 + \rho^4)^2}$$ (4.23)

and they both have an action $S = 8\pi^2/g^2$, as can be checked by direct integration.

It is clear that the above argument hinges completely on the particular connection between a manifold in physical 4-dimensional space and the group space of $SU(2)$. One may therefore ask whether these results can be in any way extended to the full $SU(3)$ of QCD. First, we note that since $SU(2)$ is a subgroup of $SU(3)$,

we can always embed these $SU(2)$ solutions in the context of full QCD. Furthermore, one can show [13] that ultimately all mappings from S^3 onto $SU(N)$ for $N > 2$ can be continuously deformed into mappings onto $SU(2)$. This means that our analysis based on $SU(2)$ is indeed relevant for 'real world' QCD, and in fact all the results presented in this work stem from the above $SU(2)$ instantons. A more detailed discussion of the connection between the dimensionality of space-time and that of the group space can be found in [81].

The question of whether other non-trivial structures may exist in the $SU(3)$ vacuum remains an open one. Such structures would have to be protected by a mechanism different to the one for the BPST instantons, but one can not exclude them outright. In fact, current numerical evidence suggests that instantons are not enough to account for quark confinement, and other mechanisms will have to fulfill that role. Whether they are long-range configurations of the gauge fields or something else altogether is at this point unknown, and the subject of current research.

4.2   Quantum Mechanical Tunneling Revisited

In the previous section we presented the mathematical background which justifies the existence of instantons. Now we will introduce a familiar problem from one-dimensional quantum mechanics which provides the basis for their physical interpretation.

Let us first expand a bit on the Wick rotation idea we mentioned in Sec. 3.1. In Minkowski space, position 4-vectors are denoted $x^\mu = (x^0, \mathbf{x})$ where $x^0 \equiv t \in \mathbb{R}$ is the time coordinate. A Wick rotation is an analytical continuation of the time coordinate made by defining

$$x^4 \equiv \tau = -ix^0 = -it. \tag{4.24}$$

With this change, the scalar product becomes

$$x^2 = x_\mu x^\mu = t^2 - \mathbf{x}^2 \xrightarrow[t \to i\tau]{} -(\tau^2 + \mathbf{x}^2) = -|x_E|^2.$$

If we now consider the Lagrangian for a classical particle in a time-independent potential

$$L = T - V = \frac{1}{2}\left(\frac{d^2x}{dt^2}\right) - V(\mathbf{x}),$$ (4.25)

and perform a Wick rotation, we obtain

$$L \xrightarrow[t \to i\tau]{} -L_E,$$ (4.26)

with

$$L_E = \frac{1}{2}\left(\frac{d^2x}{dt^2}\right) - \tilde{V}(\mathbf{x}),$$ (4.27)

$$\tilde{V}(\mathbf{x}) = -V(\mathbf{x}).$$ (4.28)

So under a Wick rotation, the mechanics of the particle is now governed in Euclidean space by an *inverted* potential.

A second important consequence of the Wick rotation is that the phase factor e^{iS} which appears in a path integral formulation of quantum mechanical problems becomes a real, damped exponential e^{-S_E}. In virtue of (4.26), we have

$$iS = i\int L\,dt \xrightarrow[t \to i\tau]{} i\int L_E(i\,d\tau) = -\underbrace{\int L_E\,d\tau}_{S_E}.$$ (4.29)

In Euclidean space, the classical solution to the equations of motion is still the leading contribution to quantum mechanical expectation values. Variations around it (quantum fluctuations) are in this formulation exponentially suppressed, while
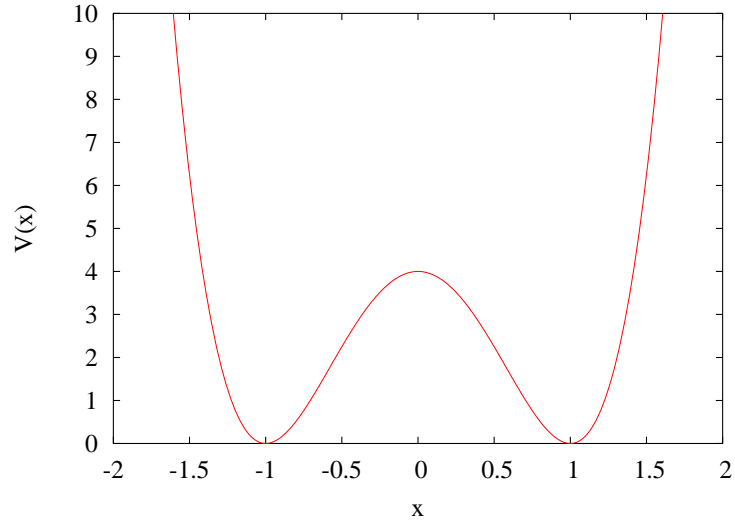
Figure 4.1: Double well potential.

in Minkowski space they tend to cancel each other out thanks to their oscillatory character.

The above remarks are equally valid for fields, as we can see by considering the Lagrangian density for a scalar field ϕ,

$$\mathcal{L} = \frac{1}{2}\partial_\mu\phi\partial^\mu\phi - V[\phi], \tag{4.30}$$

because $\partial_\mu\phi\partial^\mu\phi$ transforms like $x_\mu x^\mu$ under a Wick rotation:

$$\partial_\mu\phi\partial^\mu\phi \xrightarrow[t\to i\tau]{} -\partial_{\mu E}\phi\partial_E^\mu\phi, \tag{4.31}$$

with

$$\partial_E^\mu = \left(\nabla, \frac{\partial}{\partial\tau}\right). \tag{4.32}$$

With the above in mind, let us consider the problem, familiar from one-
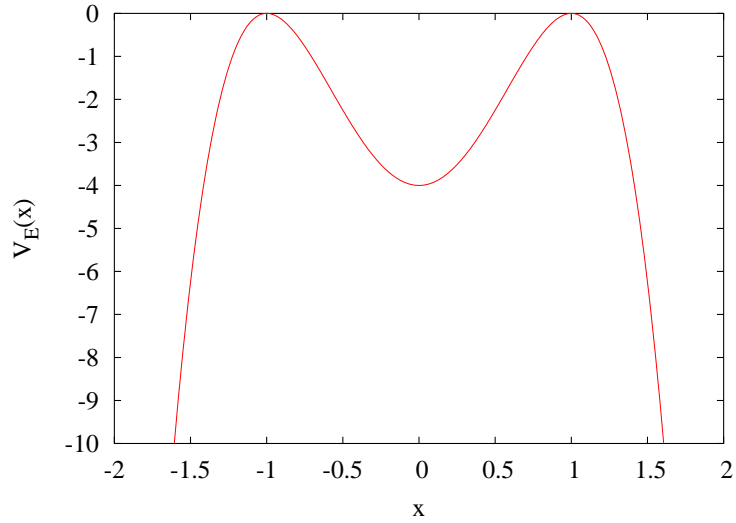
Figure 4.2: Double well potential in Euclidean space.

dimensional quantum mechanics, of a particle in a double well potential of the form

$$V(x) = \lambda(x^2 - \eta^2)^2, \tag{4.33}$$

shown in Fig. 4.1. The classical ground state for this system is located at $x = \pm\eta$, but the quantum system can tunnel from one minimum to the other. In the absence of tunneling, the states located at each minimum would be degenerate, but the presence of tunneling means that the true ground state of the system has contributions from both minima [67]. It is important to note here that tunneling is a non-perturbative phenomenon. The energy difference between the (symmetric) ground state and the (anti-symmetric) first excited states is [81]

$$E_1 - E_0 \propto e^{-\lambda^{1/2}\eta^3}; \tag{4.34}$$

this quantity can not be expanded as a power series in λ.

Now, let us perform a Wick rotation and examine the behavior of this same system in Euclidean space-time, where the potential becomes that of Fig. 4.2. We are
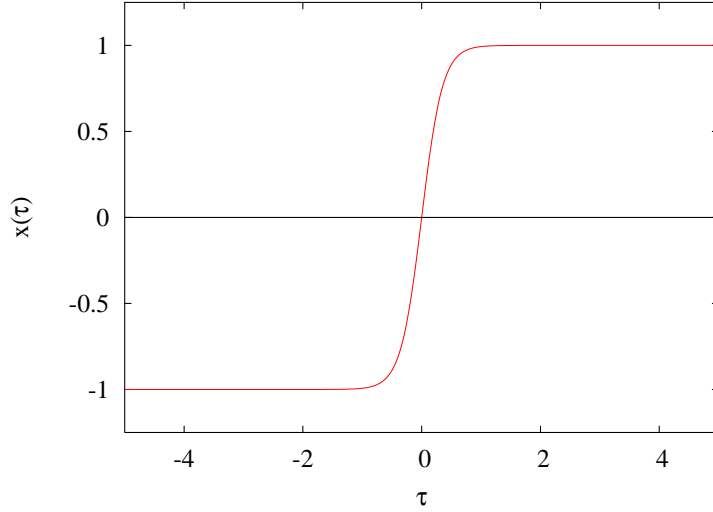
Figure 4.3: One-dimensional instanton for the potential (4.33), centered at the origin.

looking for solutions with finite action, and obviously the trivial $x(\tau) = \pm\eta$ satisfy this. However, there is a class of non-trivial solutions which connect the two humps and still have finite action: those which start at one hump as $\tau \to -\infty$ and end up in the other as $\tau \to \infty$. Since for the classical equations of motion this corresponds to zero-energy motion, the equations can be directly integrated:

$$x(\tau) = \eta \tanh\left[\sqrt{2\lambda}\eta(\tau - \tau_c)\right], \tag{4.35}$$

where τ_c is a free parameter. This solution, an instanton in one dimension for the double well potential, is shown in Fig. 4.3, for $\tau_c = 0$. This free parameter is called the 'center' of the instanton, and the total action

$$S_0 = S[x(\tau)]_{\mathrm{inst}} = \int_{-\infty}^{\infty} d\tau \dot{x}^2 = \frac{2}{3}\eta^2 \tag{4.36}$$

is independent of it.

We have then found, in Euclidean space-time, finite-action solutions to the classical equations of motion which connect various local minima for the po-

tential. These solutions are thus associated with tunneling behavior in the original Minkowski-space problem. This is exactly the scenario we discussed previously for the $SU(2)$ vacuum. Here we have presented the tunneling analogy in the context of one-dimensional quantum mechanics with an explicit potential, a situation slightly different to that of a gauge theory. However, the fundamental physical ideas are the same, and much easier to illustrate in our simplified model. A detailed presentation of the tunneling-instanton connection for the full $SU(2)$ case can be found in Ref. [11].

4.3   Instantons and Chiral Symmetry

Instantons have been very useful in understanding the problem of spontaneous chiral symmetry breaking in QCD. Let us write the fermionic part of the QCD Lagrangian (2.6) for the case of two light quarks u and d :

$$\mathcal{L} = \bar{u} i \not{D} u + \bar{d} i \not{D} d - m_u \bar{u} u - m_d \bar{d} d. \tag{4.37}$$

If m_u and m_d are very small, we can treat them approximately as vanishing. In this case ($m_u = m_d = 0$), besides an $SU(2)$ symmetry mixing the u and d fields, the Lagrangian of Eq. (4.37) is symmetric under a separate pair of $U(1)$ transformations. This can be seen by writing the quark doublet as

$$\psi = \begin{pmatrix} u \\ d \end{pmatrix}. \tag{4.38}$$

The Lagrangian (4.37) is then invariant under the global $U(1)$ transformations U_L and U_R :

$$\psi_L \to U_L \psi_L, \quad \psi_R \to U_R \psi_R, \tag{4.39}$$

where the left and right-handed fields are given by

$$\psi_L = \frac{1}{2}(1 - \gamma_5)\psi, \tag{4.40}$$

$$\psi_R = \frac{1}{2}(1 + \gamma_5)\psi. \tag{4.41}$$

We can write the currents associated with these symmetries as

$$
\begin{aligned}
j_L^\mu &= \bar{\psi}_L \gamma^\mu \psi_L, & j_R^\mu &= \bar{\psi}_R \gamma^\mu \psi_R, \\
j_L^{\mu a} &= \bar{\psi}_L \gamma^\mu \tau^a \psi_L, & j_R^{\mu a} &= \bar{\psi}_R \gamma^\mu \tau^a \psi_R,
\end{aligned}
\tag{4.42}
$$

where $\tau^a = \sigma^a/2$ ($a = 1, 2, 3$) are the $SU(2)$ generators. Adding the left and right-handed currents we obtain the baryon number and isospin currents

$$j^\mu = \bar{\psi}\gamma^\mu\psi \qquad j^{\mu a} = \bar{\psi}\gamma^\mu\tau^a\psi_R, \tag{4.43}$$

while subtracting them gives us the axial vector currents:

$$j^\mu = \bar{\psi}\gamma^\mu\gamma^5\psi \qquad j^{\mu a} = \bar{\psi}\gamma^\mu\gamma^5\tau^a\psi_R. \tag{4.44}$$

Now, in QCD if the quarks are massless, we expect the vacuum to contain a significant number of quark-antiquark pairs, since the energy cost of creating them is small. But these quarks must have zero total momentum and angular momentum, which means that they must necessarily be of opposite chirality. This means that the vacuum can be a state with a non-zero expectation value for the $\bar{\psi}\psi$ operator:

$$\langle 0| \bar{\psi}\psi |0\rangle = \langle 0| \bar{\psi}_L\psi_L + \bar{\psi}_R\psi_R |0\rangle \neq 0. \tag{4.45}$$

But if the QCD vacuum satisfies (4.45), then its symmetry is restricted to $U_L = U_R$, less than that of the original Lagrangian. This means that we have four spontaneously broken symmetries associated with the four axial vector currents. From

Goldstone's theorem, we then expect to find four massless bosons with the quantum numbers of these currents.

In nature the quarks are not in fact truly massless, but the u and d quarks are light enough that we can treat their mass perturbatively, and look for light bosons with the proper quantum numbers. In fact, the members of the pion triplet have a mass $m_\pi \approx 140$ MeV, and can thus be considered to be the Goldstone bosons of spontaneous chiral symmetry breaking.

Note however that there are *three* pions in nature, not four. The remaining 'light' Goldstone boson is missing. The particle with the right quantum numbers, the $\eta^{'}$, is much heavier than the pions ($m_{\eta'} \approx 958$ MeV). This is due to the fact that the ABJ anomaly breaks the conservation of the axial current $j^{\mu 5}$, a situation known as the $U_A(1)$ problem. It turns out that this problem can be understood in terms of instantons, as was shown by 't Hooft in [79], but we will not pursue this point any further.

Going back to the pions, we now ask, what mechanism drives the spontaneous breaking of chiral symmetry? The connection with instantons is given by the Banks-Casher relation [5]:

$$\langle 0 | \bar{\psi}\psi | 0 \rangle \propto \rho(\lambda \to 0), \tag{4.46}$$

where $\rho(\lambda)$ is the density of eigenmodes of the Dirac operator with eigenvalue λ:

$$D\psi = \lambda\psi. \tag{4.47}$$

It was found by 't Hooft ([78], [79]) that the Dirac operator has exact zero modes ($\lambda = 0$) in the presence of isolated instantons. When we have a complex vacuum with interacting instantons and anti-instantons, these exact zero modes are broken into conjugate near-zero pairs. This means that (4.46) is in fact a relation connecting the instanton content of the vacuum with chiral symmetry breaking.

This relation is extremely useful for establishing a phenomenological connection for instantons, since for finite quark mass one can show that [53]

$$\langle 0| \bar{\psi}\psi |0\rangle \frac{m_q}{N_f} = \frac{f_\pi^2 m_\pi^2}{2N_f^2} + O(m_\pi^4). \tag{4.48}$$

We will not cover this problem in more depth here; interested readers should refer Diakonov's review [28] and Nieter [56] for further background. We must note that this issue is not currently settled, and there is ongoing research trying to establish whether the instantons are in fact fully responsible for breaking chiral symmetry, or just part of the answer. Details on the current state of this problem can be found in [17], [16] and references therein.

4.4   Instantons in the $SU(3)$ Vacuum

Up to this point we have discussed the properties of isolated instantons. The BPST instanton is a solution of the classical equations of motion, but it describes only one object with topological charge $Q = 1$. On the other hand, we know from the arguments presented above that there exist vacua with arbitrary values of Q. While we do not have exact analytic solutions for such configurations, approximations can be made based on the single instanton solution. If we assume that there are widely separated instantons, we expect a simple superposition solution to be a reasonable approximation to more complex vacua.

A model of very separated instantons is called the instanton 'gas' model, and it has been found to be insufficient for accurately describing some known phenomenological properties of the vacuum, such as the chiral symmetry relation (4.48). On the other hand, a model with slightly higher density of particles, known as the Instanton Liquid Model (ILM) has been shown to be reasonably successful in describing a number of phenomenological properties of the vacuum[69].

In 1998, Hasenfratz and Nieter ([41], [56]) performed actual measurements
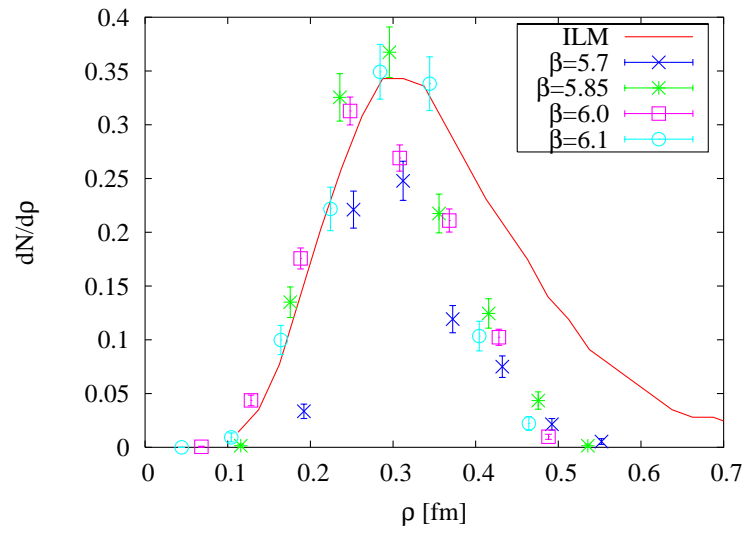
Figure 4.4: Instanton distribution in $SU(3)$, taken from [41]. The solid line represents the prediction from the phenomenological Instanton Liquid Model.

of the instanton contents for the $SU(3)$ vacuum, and found them to be in reasonable agreement with the ILM, as shown in Fig. 4.4.

Chapter 5

Topology on the Lattice

The measurement of quantities related to topology on a discrete lattice presents a number of challenges, but it has been the subject of extensive study in recent years. The main problems which need to be addressed are:

(1) How to remove random vacuum fluctuations without destroying topological features.

(2) How to find suitable lattice representations of the continuum operators we want to measure.

We will briefly present here the strategies developed to tackle these two issues and extract information about topological properties from numerical simulations. We follow and summarize here the presentations from [56], [38] and [25], where more details can be found.

5.1 Smoothing

On the lattice, we must deal with the dominance of random vacuum fluctuations which have no long-range structure. The instantons, while dynamically of crucial importance, have a relatively low action content: the action of a typical vacuum configuration is overwhelmingly due to uncorrelated fluctuations, with the instantons contributing only a small percentage of the total action. Their importance comes, of

course, from their long-range coherent structure[1]. But their smallness makes them very difficult to detect, as they are buried under a pile of random but larger fluctuations [55, see Fig. 7]. A number of methods have been developed to address this problem. They all attempt to remove the short-range, random fluctuations while protecting as much as possible any underlying semi-classical structure.

Based on Renormalization Group (RG) ideas, the perfect actions developed by Hasenfratz *et al.* [24, 23, 42, 43] provide an exact preservation of all the classical properties of the gauge background. Perfect actions restore rotational symmetry, have an exact spectrum and provide scale invariant instantons, even on coarse lattices. They appear as an ideal solution to extract topological information from the gauge fields. The problem is that, in practice, perfect actions are prohibitively expensive to implement for QCD.

However, the theoretical ideas behind perfect actions gave us insight into the kind of structure that better actions need. While it may be impossible to do practical calculations with perfect actions, we may still be able to construct approximate algorithms capable of seeing topological structures through the noisy QCD vacuum. The basic idea is to replace the links by averages of neighboring links. These 'fat links' are able to 'smear' the highly local uncorrelated fluctuations without distorting longer-ranged structures excessively.

The simplest method which can be connected to these ideas is known as APE smearing [30, 1]. APE smearing is in fact older than the perfect action construction, but today we can see it as a member of the same family of ideas. It is based on the construction

$$
\begin{aligned}
X_\mu(x) = (1-\alpha)U_\mu(x) \quad &+ \quad \frac{\alpha}{6}\sum_{\nu \neq \mu}[U_\nu(x)U_\mu(x+\hat{\nu})U_\nu(x+\hat{\mu})^\dagger \\
&+ \quad U_\nu(x-\hat{\nu})^\dagger U_\mu(x-\hat{\nu})U_\nu(x-\hat{\nu}+\hat{\mu})], \qquad (5.1)
\end{aligned}
$$

---

[1]Even if we think of an instanton as a localized object, the symmetries protecting it are ultimately global, as they are connected to the asymptotic behavior of the gauge fields.
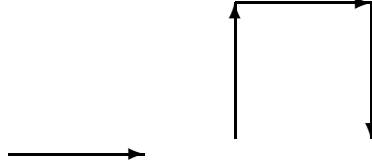
Figure 5.1: Paths used in building the APE links.

where $X_\mu(x)$ is called a smeared link, and the free parameter α is known as the smearing fraction. The paths which enter (5.1) are shown in Fig. 5.1. At each step of the process, a link $U_\mu(x)$ is replaced by the projection of the smeared link onto the gauge group.

In [26], the Boulder group worked on a smoothing algorithm which tried to implement all the properties of perfect actions. Unfortunately, this approached proved to be computationally very expensive. But they found that a practical compromise could be obtained via a set of several carefully tuned APE steps. This method, known as RG mapping, maintains most of the desirable scaling properties of the original idea.

In [38], Hasenfratz and Knechtli developed a new smoothing algorithm based on APE smearing, called HYP blocking. This method was used to explore the finite temperature features of QCD [39, 35] and for dynamical fermion simulations [51, 36, 40]. The HYP links are given by:

$$
\begin{aligned}
V_{i,\mu} &= Proj_{SU(3)}[(1-\alpha_1)U_{i,\mu} + \frac{\alpha_1}{6}\sum_{\pm\nu\neq\mu}\tilde{V}_{i,\nu;\mu}\tilde{V}_{i+\hat{\nu},\mu;\nu}\tilde{V}^\dagger_{i+\hat{\mu},\nu;\mu}], \\
\tilde{V}_{i,\mu;\nu} &= Proj_{SU(3)}[(1-\alpha_2)U_{i,\mu} + \frac{\alpha_2}{4}\sum_{\pm\rho\neq\nu,\mu}\bar{V}_{i,\rho;\nu\,\mu}\bar{V}_{i+\hat{\rho},\mu;\rho\,\nu}\bar{V}^\dagger_{i+\hat{\mu},\rho;\nu\,\mu}], \quad (5.2) \\
\bar{V}_{i,\mu;\nu\,\rho} &= Proj_{SU(3)}[(1-\alpha_3)U_{i,\mu} + \frac{\alpha_3}{2}\sum_{\pm\eta\neq\rho,\nu,\mu}U_{i,\eta}U_{i+\hat{\eta},\mu}U^\dagger_{i+\hat{\mu},\eta}].
\end{aligned}
$$

These complicated-looking forms are simply a three-level process of APE-
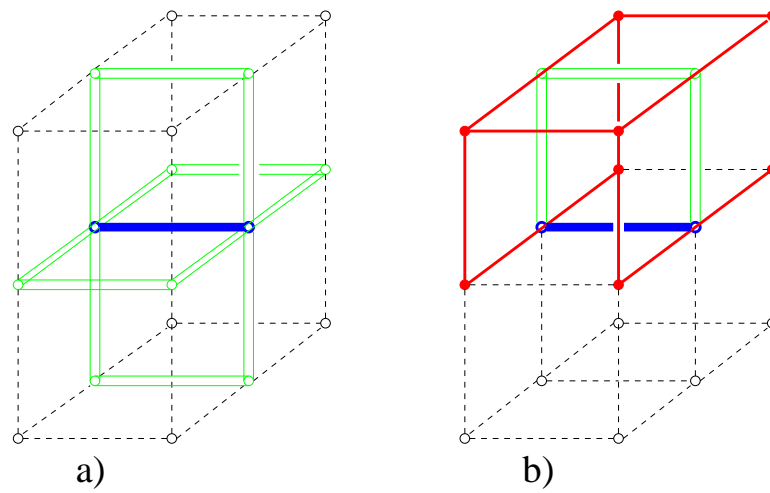
Figure 5.2: Schematic structure of HYP links in three dimensions, from Ref. [38]. In a), the fat link is built from the four double-lined staples; in b) each double-lined link is built from two staples which extend only into the hypercubes attached to the original link.

like smearing steps, each similar to (5.1). At each step the resulting links are projected back onto the $SU(3)$ gauge group. This construction is illustrated for a three dimensional space in Fig. 5.2, taken from Ref. [38]. The HYP algorithm has a triple $(\alpha_1, \alpha_2, \alpha_3)$ of parameters similar to APE's α. One of the main strengths of this method is its improvement of flavor symmetry breaking when used with Kogut-Susskind fermions [38]. The α_i parameters are tuned to maximize the value of the smallest plaquette. Since flavor symmetry breaking is driven precisely by local fluctuations in the gauge fields, this procedure improves the flavor symmetry properties of the resulting action.

In our analysis of topological features, we will mainly use APE smearing, but we will present some comparisons with HYP blocking.

There is another family of smoothing algorithms known as 'cooling' [9, 80, 44], which perform a local minimization of the action. The minimization tends to remove fluctuations in the local neighborhood which have large action, but the locality of the process protects long-range structures such as the instantons. The process is carried over the entire lattice in what is called a *sweep.* The simplest cooling algorithms do in fact have a significant impact on instantons after a limited number of sweeps, but more sophisticated ones have been developed which protect the instantons over hundreds of sweeps [19]. A comparison between cooling and smearing algorithms can be found in [12].

5.2   Operators

For measuring topological properties, we have the same freedom we had with respect to the action. Any operator which in the $a \rightarrow 0$ limit describes a continuum quantity is in principle an acceptable lattice description, and with this freedom we can try to control different problems. As we know, the action of a BPST instanton is independent of its radius ρ, but on the lattice this scale independence is broken by the introduction of the lattice spacing a. Furthermore, this minimum scale
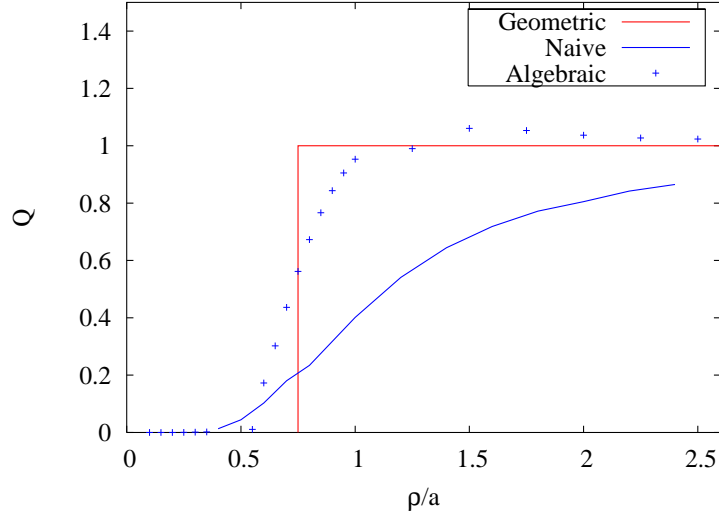
Figure 5.3: Comparison of topological charge operators for a background with a single $SU(2)$ instanton, from Ref. [25].

means that the lattice can not resolve any structure smaller than a, so any instanton with $\rho \lesssim a$ will "fall through the lattice".

A purely geometric definition [54, 61] exists which guarantees exact integers for the total topological charge. This geometric operator is shown in as a solid line Fig. 5.3 (from Ref. [25]) . This figure shows the topological charge of smooth, continuum-like instantons as a function of their radius. The measurements were done on gauge backgrounds containing a single instanton, at various values of the instanton radius. The geometric operator can only identify instantons whose radius is of the order of the lattice spacing, as expected, but it provides a sharp, clear signal for the presence of those instantons it can detect. Unfortunately this operator is computationally very expensive, and it is therefore not used in full-scale calculations.

While there is little we can do about losing very small instantons on the lattice, the scaling issues can be dealt with in ways which are still computationally practical. In (4.7) we defined the continuum topological charge for a gauge back-

Table 5.1: Couplings for the algebraic topological charge operator.

Operator	c_1	c_2
1	0.09030	0.48846
2	-0.17863	0.41270

ground. The integrand in that expression,

$$q(x) = F_{\mu\nu}^a(x)\tilde{F}_{\mu\nu}^a(x), \tag{5.3}$$

is known as the topological charge density. The simplest discretization which has the correct $q(x)$ limit as $a \to 0$ is the twisted plaquette consisting of the path $(\hat{x}, \hat{y}, -\hat{x}, -\hat{y}, \hat{z}, \hat{t}, -\hat{z}, -\hat{t})$. As we discussed in Chapter 4, the total topological charge Q is an integer quantity, but this naïve discretization does not in general produce an integer value. In Fig. 5.3 the results from this operator are shown as a dashed line. We can see that it has a very smooth profile, incapable of providing a clear identification even of instantons with $\rho \sim 1.5a$.

In [25], DeGrand *et al.* developed an improved operator for the measurement of topological charge in $SU(2)$ based on renormalization group ideas, which we will use for our work. Their 'algebraic' charge definition is made of two operators in two representations:

$$q(x) = \sum_j c_j^1 \operatorname{Tr}(1 - U_j) + c_j^2 \left[\operatorname{Tr}(1 - U_j)\right]^2, \tag{5.4}$$

where operator 1 is the path $(\hat{x}, \hat{y}, \hat{z}, -\hat{y}, -\hat{x}, \hat{t}, \hat{x}, -\hat{t}, -\hat{x}, -\hat{z})$ and operator 2 is the path $(\hat{x}, \hat{y}, \hat{z}, -\hat{x}, \hat{t}, -\hat{z}, \hat{x}, -\hat{t}, -\hat{x}, -\hat{y})$, summed over all permutations and reflections. The coefficients are tuned to optimize the identification of instantons, using the geometric operator as a reference. The actual values are given in Table 5.1.

As shown in Fig. 5.3, the algebraic operator reproduces the sharp profile of the geometric definition fairly well. It remains simple enough to be of practical use.

Chapter 6

Finite Temperature

So far we have discussed features of QCD –such as asymptotic freedom and confinement– at zero temperature, and laid out the framework for studying them numerically on the lattice. At this point we turn our attention to the high temperature regime of the theory, and in particular to some interesting effects which are expected to be present on the lattice.

We will first motivate the subject with a brief description of the expected features of QCD at high temperatures and then proceed to look at instantons on the lattice under these conditions.

6.1   High Temperature QCD in the Continuum

As we have already discussed, under typical conditions we never observe free quarks, as all color charge is confined inside the hadrons. We now ask whether this situation persists under conditions of high temperature and/or density.

A naïve thermodynamic analysis of the quark and gluon density of states in fact predicts a transition from a mixture of free ultra-relativistic Fermi and Bose gases to a plasma with no distinct hadrons [33]. By equating the pressure in the gas with the B parameter from the MIT Bag model, for two quark flavors we obtain the
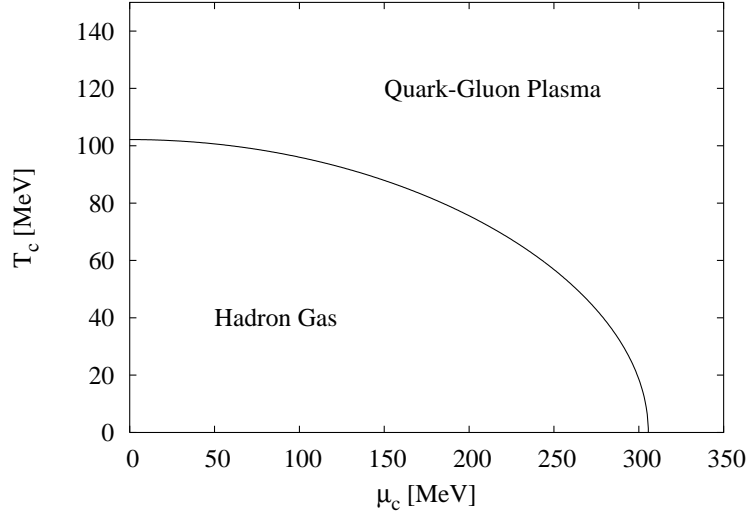
Figure 6.1: QCD phase diagram at first approximation.

phase boundary

$$B = T_c^4 \left[\frac{37\pi^2}{90} + \left(\frac{\mu_c}{T_c} \right)^2 + \frac{1}{2\pi^2} \left(\frac{\mu_c}{T_c} \right)^4 \right], \tag{6.1}$$

illustrated in Fig. 6.1. We must note that this picture should only be considered as having qualitative value, since the actual numbers it predicts are based on overly simplistic assumptions.

However, the overall physical picture presented here is supported both by analytical arguments [62] and by numerical results [27]. Table 6.1 summarizes the key features of the two regimes of QCD, at zero chemical potential. In this work we will not look at the $\mu_c > 0$ regime, which has its own set of complications and on which only recently some progress has begun to be made. In [52], Kogut presents a review of the state of the art with respect to QCD at high temperature and density. He discusses the lattice results in connection with the experimental data which is now available from the Relativistic Heavy Ion Collider (RHIC) facility at Brookhaven National Laboratory. At this point we do not have conclusive evidence of the existence of the quark gluon plasma, but various experimental signatures

Table 6.1: Comparison of QCD features at low and high temperatures.

Low T	High T
Hadronic matter	Quark-gluon plasma
Confined quarks and gluons	Debye screening of color
Broken chiral symmetry	Restored chiral symmetry

are indeed well described under such an assumption. Further work both on the experimental data and on the lattice will be needed to understand this issue.

Under the assumption that some sort of transition does indeed exist, its exact nature remains to be specified. At zero chemical potential, Pisarski and Wilczek [62] argued that for 3 or more massless quark flavors, QCD should have a first order transition. For $N_f = 2$, the exact nature of the instanton background may determine whether the transition is of first or second order. For non-vanishing quark masses, the transition appears to be of different types depending on the type of fermionic action used for the simulation. Looking at staggered fermions, Aoki *et al.* [2] find no evidence of a first order transition and rather a crossover behavior. This was confirmed by Hasenfratz and Knechtli [39] using also staggered fermions but the more sophisticated HYP gauge links. In contrast to this, Iwasaki *et al.* find [47] that Wilson fermions exhibit either a first or second order transition, depending on the number of flavors. The origin of this discrepancy is still the subject of debate and research, since ultimately we expect the physical predictions to be independent of the modeling tools employed.

6.2   Finite T on the Lattice

We will now discuss how finite temperature calculations are implemented on the lattice. First of all, let us recall that in the continuum, finite temperature field theory (in thermal equilibrium) is described by an analytical continuation of the time coordinate of the form $t \to -i\tau$. Since this is exactly the process we followed

to implement the lattice description of quantum field theories, the lattice already has the basic layout to describe finite temperature. The connection is continued by interpreting the 'time' direction on the lattice, τ, as the inverse temperature $\beta = 1/T$.

Finally, we note that the partition function of a thermodynamic system is given by

$$Z = \operatorname{Tr} e^{-H/T}. \tag{6.2}$$

This trace can be obtained on the lattice by requiring periodic boundary conditions on the gauge fields and antiperiodic boundary conditions on the fermion fields.

The connection between time and inverse temperature is made in practice by using lattices which are *shorter* in the fourth direction, which represents time in the zero-temperature case. This can be understood by considering that the spatial directions represent an infinite volume (in principle), while at finite temperature, $\beta \sim \tau$ is an explicitly finite quantity.

We must stress that we are now considering an equilibrium system at finite temperature, so there is no real time variable any more. It is important to remember this fact as the literature often uses the 'time direction' term to refer casually to the fourth dimension, under the understanding that there is no time evolution being studied here, only equilibrium thermodynamics.

The topic of lattice theories at finite T is discussed in detail in presentations by DeTar [27] and Karsch [49]. For recent reviews of the current state of lattice thermodynamics, in addition to the Karsch reference, we refer the reader to Refs. [50, 31].

6.3 Finite T Effects on Instantons

Now we turn our attention to the effects we expect to see in the structure of instantons at finite temperature. The key idea we will exploit is based on the

realization [69, Sec. IV.A.2] that we can interpret the propagation of quarks in the QCD vacuum as a process of hopping from instantons (I) to anti-instantons (A). This process in turn induces an effective attractive interaction between the instantons and the anti-instantons, which we expect to play a significant role in dynamical simulations. We will now outline Shuryak's argument.

First of all, let us recall that the Dirac operator has exact fermionic zero modes in the presence of an (anti)-instanton, and that these zero modes are of (negative) positive chirality. The basic idea when considering the fermionic instanton interaction is to split the Dirac spectrum into quasi-zero modes (associated with I-A pairs), linear combinations of the zero modes of the individual isolated instantons, and non-zero modes. In the basis spanned by the zero modes, we can write the Dirac operator as

$$
i\slashed{D} = \begin{pmatrix} 0 & T_{IA} \\ T_{IA} & 0 \end{pmatrix}, \tag{6.3}
$$

where the overlap matrix elements T_{IA} are defined as

$$
T_{IA} = \int d^4x \psi_{0,I}^\dagger(x - z_I) i\slashed{D}\, \psi_{0,A}(x - z_A). \tag{6.4}
$$

Here, $\psi_{0,I}(x - z_I)$ is a fermionic zero mode associated with an instanton with center at z_I. This matrix element has the structure of a hopping amplitude from one pseudo-particle to another. It can be written as two quark-instanton vertices connected by a propagator, $\psi_{0,I}^\dagger i\slashed{D}(i\slashed{D})^{-1}i\slashed{D}\psi_{0,A}$. The matrix elements T_{II} and T_{AA} due to pseudo-particles of identical topological charge vanish due to the chirality of their associated zero modes. The effective interaction resulting from these modes is attractive.
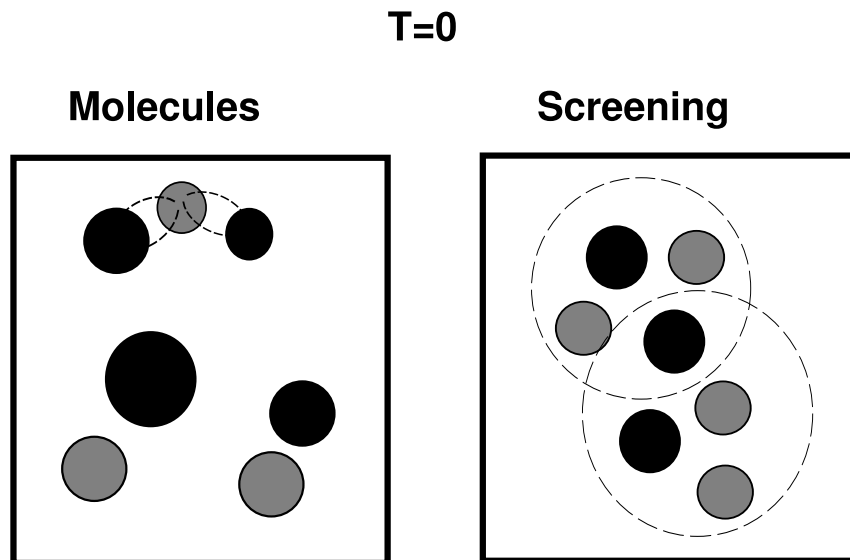
Figure 6.2: At $T = 0$ the net topological charge vanishes as $m_q \to 0$. Likely mechanisms for this are the formation of tight I-A pairs or screening in clouds of net vanishing charge.

The topological susceptibility χ is defined as

$$\chi = \frac{1}{V}\left\langle Q^2 \right\rangle, \tag{6.5}$$

where V is the lattice volume. One can show [37] that in the presence of dynamical quarks χ is given by

$$\chi = \left\langle \bar{\psi}\psi \right\rangle \frac{m_q}{N_f^2} + O(m_\pi^4) = \frac{f_\pi^2 m_\pi^2}{4N_f} + O(m_\pi^4). \tag{6.6}$$

For dynamical configurations at zero temperature, as $m_q \to 0$ we then find that $\langle Q \rangle \to 0$. The two most likely mechanisms for this to occur are the formation of tight instanton–anti-instanton (IA) pairs or the screening of net charge, as illustrated in Fig. 6.2. In [37], Hasenfratz considered these two scenarios and found evidence for the formation of pairs. The present work can be considered a continuation of this investigation which tries to probe the finite temperature regime.

At finite temperature, the fermionic interaction we have just described remains a key factor in shaping the vacuum. But the anisotropy of the space-time lattice introduces new elements into the problem. First of all, let us look at the structure of fermionic propagators at finite temperature. At finite T the free massless fermion propagator in the spatial direction is given by [69]

$$S_T(r,0) = \frac{i\overrightarrow{\gamma} \cdot \overrightarrow{r}}{2\pi^2 r^4} z e^{-z} \left[\frac{(z+1) + (z-1)e^{-2z}}{(1+e^{-2z})^2} \right] \tag{6.7}$$

where $z = \pi r T$, and in the τ direction by

$$S_T(0,\tau) = \frac{i\gamma_4}{2\pi^2 \tau^3} \frac{y^3}{2} \frac{1 + \cos^2(y)}{\sin^3(y)} \tag{6.8}$$

where $y = \pi \tau T$. These propagators are both shown in Fig. 6.3.

We see that propagators for fermions are exponentially suppressed in the
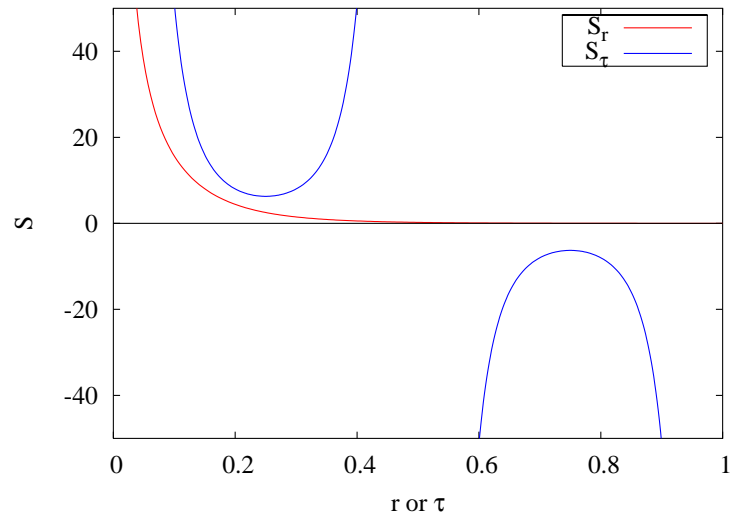
Figure 6.3: Fermion propagators at finite temperature.

spatial directions, relative to the time direction. This difference in the fermion prop-agators, in accordance to our picture of fermion-induced interactions we described earlier, should manifest itself also in the behavior of the instantons. And indeed, if we look at the T_{IA} overlap matrix elements at finite T, we find that it can be written as [77]

$$T_{IA}(x) = a f_1(x) + b f_2(x), \tag{6.9}$$

where a and b are constants whose specific form need not concern us here. The asymptotic forms for the f_i functions can be computed in the high temperature limit as:

$$f_1^{\text{as}} = i\frac{\pi^2}{\beta} \sin\left(\frac{\pi\tau}{\beta}\right) \exp\left(-\frac{\pi r}{\beta}\right), \tag{6.10}$$

$$f_2^{\text{as}} = i\frac{\pi^2}{\beta} \cos\left(\frac{\pi\tau}{\beta}\right) \exp\left(-\frac{\pi r}{\beta}\right). \tag{6.11}$$

From these forms we see that at high temperatures, the T_{IA} elements are strongly anisotropic. They display exponential suppression in the spatial directions while maintaining periodicity in the temporal direction. Because of this, and keeping in mind that the background gauge fields are periodic themselves in the time direction, we expect to see a strong anisotropy in the vacuum structure at finite temperature. We can interpret this effect by considering the interaction between any (anti)instanton and its 'image' charge which occurs through the time direction in virtue of the periodicity of the boundary conditions. This is illustrated in Fig. 6.4.

Now, we must note that these effects are not expected to appear in quenched simulations. The instanton structure depends critically on the existence of virtual quark-antiquark pairs which appear from the gauge vacuum. These virtual pairs es-tablish the attractive interactions between instantons and anti-instantons and they are absent in quenched simulations. In the pure gauge case, we expect to see some-
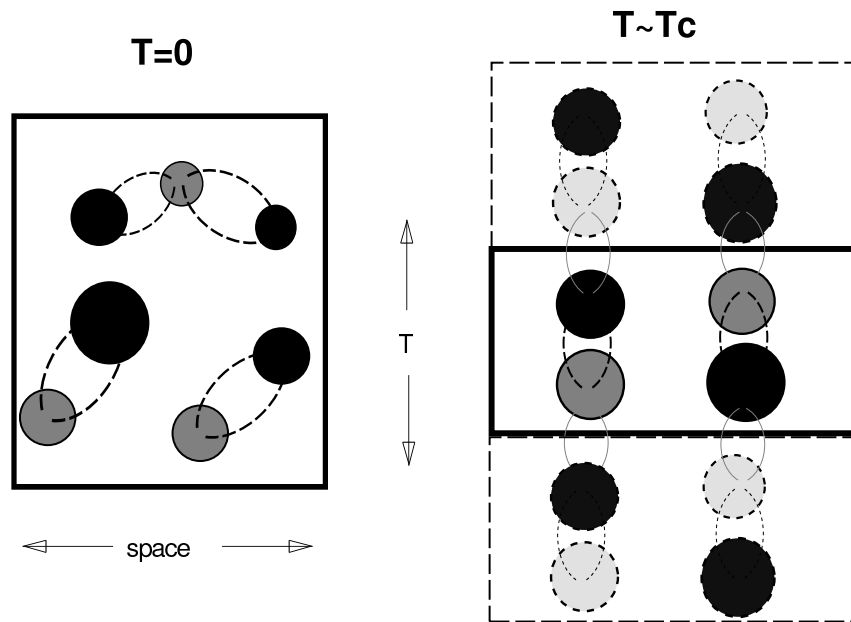
Figure 6.4: The quark-induced interaction picture for the instanton polarization effect at the phase transition.

thing similar to what is shown in Fig. 6.5, with no polarization structure in the temporal direction.

6.4 Previous Work on Pair Formation

The issue of instanton pair formation and polarization has been studied in the past, and we will summarize the existing work on this problem. The oldest proposals come from Ilgenfritz and Shuryak [46, 45], who first introduced the idea that a quark-induced interaction between instantons could be a driving factor for the chiral phase transition. Their work relied on approximate expressions for the instanton partition function and not on direct lattice simulations.

In [76], Shuryak and Velkovsky used Partially Conserved Axial Current (PCAC) methods to obtain a strict result concerning instanton densities as a function of temperature. This result gave strength to the idea of instanton pairing at finite temperatures as opposed to a disappearance of the instantons altogether (which could be another mechanism explaining chiral restoration at high T).

In [70], Schäfer found strong evidence of the polarization effect by simulating the statistical mechanics of a single IA pair as a function of temperature. However, for this idea to be validated it needs to be studied in the context of full lattice simulations, and this is the path we follow in our work. Schäfer and Shuryak visited the problem in [68], also performing numerical simulations of the statistical mechanics of an instanton model. They identified clear evidence of polarized pair formation at finite temperature, as seen in Fig. 10 of their work. We must emphasize that this was not done in the context of a full dynamical lattice simulation, which is a much noisier environment than that of a controlled instanton-only model.

In [83, 84], Velkovsky and Shuryak performed a very detailed analytical study of the instanton interactions and the resulting structure at temperatures close to T_c. Their results again are in strong support of pair formation as a key mechanism of the chiral transition, and their analysis of the fermionic-induced interactions, while
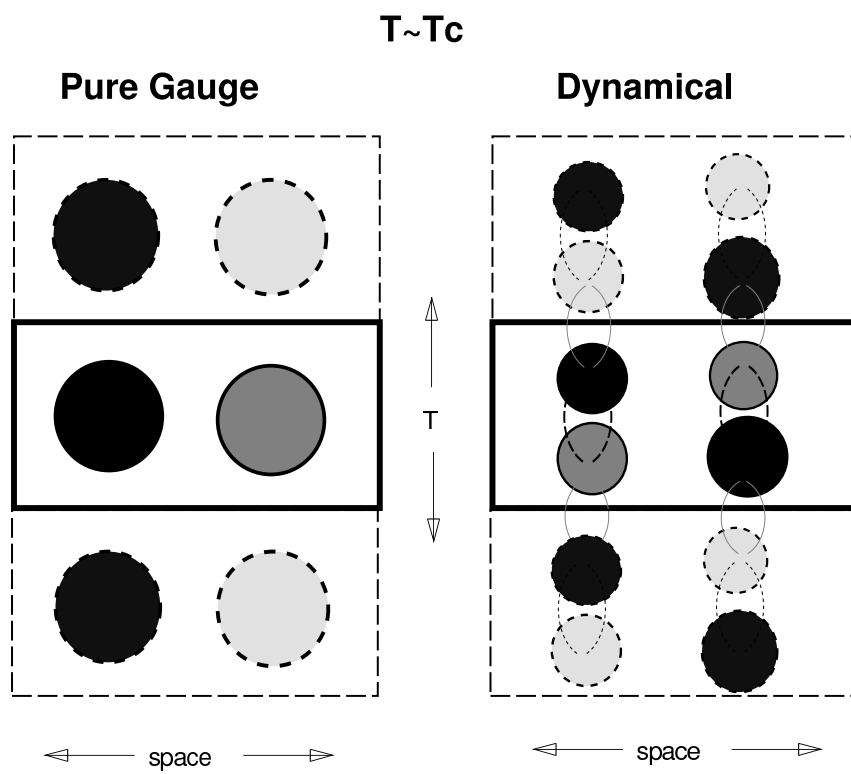
Figure 6.5: Around the phase transition, we expect a difference between quenched and dynamical simulations, induced by the virtual quarks.

far more detailed than what we have presented here, supports the overall physical picture we gave.

After all this evidence accumulated in support of the pair formation mechanism discussed here, Hasenfratz [37] performed the first direct measurements on dynamical lattice simulations. She analyzed the spatial structure of the topological charge density two-point correlator

$$c(x) = \frac{1}{V} \int d^4x' \, q(x')q(x' + x), \qquad (6.12)$$

comparing pure gauge $SU(3)$ configurations against full QCD ones, at zero temperature. According to the picture we've discussed, she expected to find a significant difference between the two cases, even at $T = 0$. She found that the dynamical simulations exhibited a much stronger degree of instanton pairing than the quenched ones. The present work continues this investigation by looking at the finite temperature structure, where we expect to find signatures of these same effects.

Chapter 7

Topological Charge Correlation Analysis

In this chapter will study the topological structure of the QCD vacuum by measuring on the lattice the correlation function

$$c(x) = \frac{1}{V} \int d^4 x' \, q(x') q(x' + x) \tag{7.1}$$

where $q(x)$ is the topological charge density. We are specifically looking for the effects of working at finite temperature, which should manifest themselves as a dependence of $c(x)$ on the fourth coordinate. This fourth coordinate will be henceforth labelled t, but which as we've discussed, it does not represent physical time. For the sake of brevity we may call it in our discussion the 'time' coordinate or direction, but it should be clear by this point that this terminology does not in any way imply a dynamical process: we are only looking at equilibrium thermodynamics.

In order to study this effect, we will perform averages of $c(x)$ over the spatial coordinates. If we write the four-vector x as $x = (\mathbf{r}, t)$ and $r = |\mathbf{r}|$ where $\mathbf{r} \in \mathbb{R}^3$, after averaging the $c(x)$ data over all orientations of $\mathbf{r}$ we will be left with correlation information of the form $c(r, t)$ where we will try to find a signal for temperature-induced effects on the topological structure.

We will begin by taking a brief look at $c(r, t)$ in a set of finite-temperature quenched configurations as a first reference, and will then proceed to study in detail a large set of dynamical configurations.

Table 7.1: Dataset for pure gauge configurations. All lattices of dimension $16^3 \times 8$.

β	APE	Total
5.90	24, 36, 48	100
6.00	24, 36, 48	100
6.10	24, 36, 48	100

7.1 Lattices Processed

For this project, we looked at a large set of configurations, available from the publicly available archive known as the Gauge Connection (`http://qcd.nersc.gov`). We studied a set of $16^3 \times 8$ quenched lattices as a reference, and used the large $24^3 \times 12$, $N_f = 2$ dataset produced by the MILC collaboration for a detailed thermodynamic study performed in 1996 [10].

Table 7.1 lists the quenched dataset used, and the levels of APE blocking performed on it. Similarly, Table 7.2 shows the size of our dynamical dataset, along with the levels of both APE and HYP blocking performed. It is necessary to smear the configurations in order to extract topological information from them, but we have monitored the effects of smearing to make sure that the physically relevant information is not lost in the process. This is discussed in more detail in sections 7.4 and 7.5.

These lattices make up the complete set available at the Gauge Connection

Table 7.2: Dataset for dynamical configurations. All lattices of dimension $24^3 \times 12$. Numbers in parentheses indicate the number of processed lattices at a given blocking level, when different from the total available data set for that mass and β value.

m_q	β	APE	HYP	Total
0.008	5.65	24, 36, 48	2,3,4	149
	5.725	24, 36, 48	2, 3, 4, 6, 8	129
	5.85	6, 9, 12, 18, 24, 36, 48	2, 3, 4, 6, 8	148
0.016	5.70	24, 30 (23)	2,3,4	241
	5.75	24	2,3,4	253
	5.80	24, 30 (48)	2,3,4	249
	5.85	24	N/A	165

archive, and the processing of the set (both quenched and dynamical) took several months of processing on multiple workstations belonging to the Colorado High Energy Group.

Quark mass values, here and in the rest of this chapter, are given in dimensionless form. A dimensionful value is obtained by rescaling with the lattice spacing: $m_q^{\text{phys}} = m_q^{\text{unitless}}/a$. In the following we will simply write m_q for the unitless values.

The dynamical lattices (which we will focus on) have a physical lattice spacing $a \approx 0.1 \, \text{fm}$. In [10], Bernard *et al.* found signals of a transition as a weak crossover. They combined an analysis of several observables (Polyakov loop, $\langle \bar{\psi}\psi \rangle$, a fuzzy loop, baryon susceptibility, induced quark number and chiral susceptibility) to pinpoint its location. Their conclusion is that for $m_q = 0.008$ the crossover is located in the $\beta = 5.65 - 5.70$ range and for $m_q = 0.016$ in the $\beta = 5.75 - 5.85$ range.

7.2   Finite Temperature Quenched Configurations

Our first step will be to study the behavior of $c(r, t)$ for quenched configurations. This will be useful as a reference point to contrast our findings with the dynamical lattices.

Figure 7.1 shows the results of our measurements for the entire quenched dataset. We see that, within the statistical uncertainty, there is no measurable difference between the various t values. Even though the lattices are strongly anisotropic, the topological structure itself does not manifest this anisotropy.

This first observation is in agreement with the scenario we have described in Chapter 6. The absence of virtual quark-antiquark pairs removes the mechanism for inducing anisotropy in the topology. This does not mean that no finite temperature physics is present in quenched simulations, but it does indicate that there will be significant limitations when studying phenomena strongly connected to topological effects.
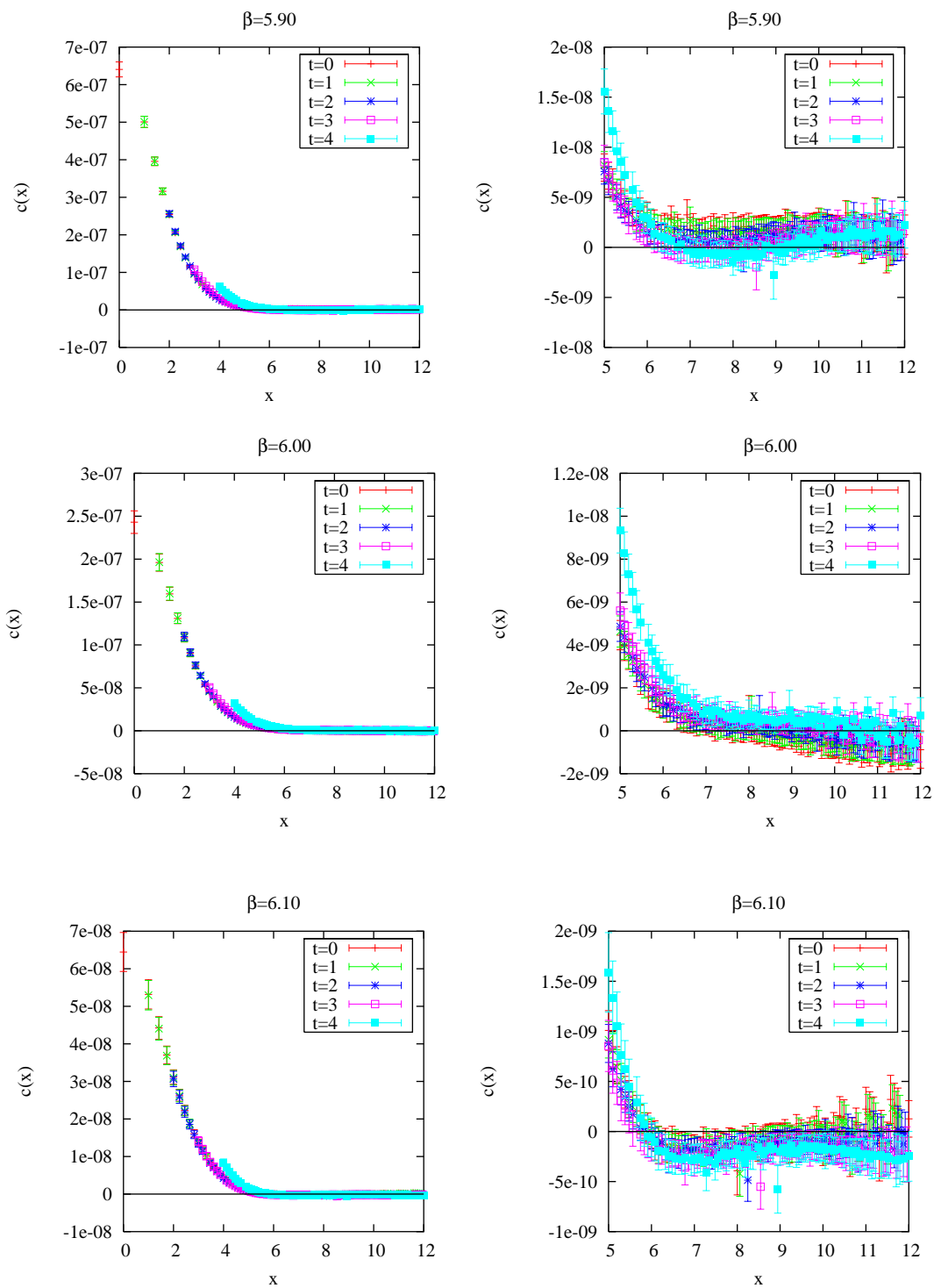
Figure 7.1: Plots of $c(r, t)$ for the pure gauge configurations. All lattices were blocked 24 APE steps. The column on the right is a detail of the $x = [5, 12]$ region.

7.3 Directly Looking at Dynamical Configurations

Before showing our correlation measurements for the dynamical configurations, let us first take a look at the lattices themselves. This will be an instructive exercise to perform, as we will be able to see that the intuitive picture we have previously discussed is a rather strong idealization.

Schäfer and Shuryak [68] present figures with a very clearly organized structure of instanton-anti-instanton pairs polarized in the time direction. However, we must keep in mind that this work was based on a hand-constructed model of interacting instantons, and it is *not* a direct measurement of quantities in a full QCD calculation. Looking at such an environment shows a far more complex structure for the gauge background.

We will study the topological charge density directly, by looking at a few configurations. We must emphasize that a direct visual study of a handful of configurations can not be used to extract any quantitative information, given the nature of a Monte Carlo calculation. On the other hand, it can be very useful for gaining insights into what the fields we are interested in actually look like. Here we will only present images for a few lattices chosen as typical representatives of the dataset after having looked at many of them.

On a typical lattice after 24 APE steps, the topological charge density has a distribution such as is shown in Figure 7.2, nearly symmetrical about the origin. In order to be able to process many lattices efficiently we clipped the data to a symmetric range. We then computed isosurfaces of constant topological charge at 32% and 68% of the full range of values.

Figure 7.3 shows[1] the resulting isosurfaces for lattice 704[2]. The various

---

[1]In the next chapter we will present some details about the tools used for these visualizations.

[2]This lattice is a typical representative of the features present in all of the configurations studied. We will also use a few other lattices for visualization purposes. They were all chosen because they offer clearly visible topological structures, but are in no way fundamentally different from any other lattice in our entire sample.
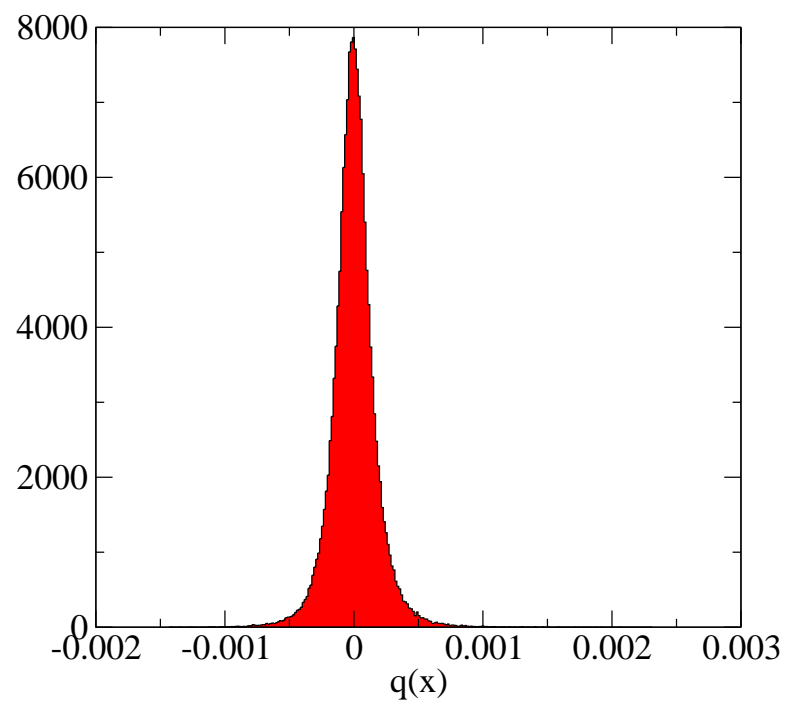
Figure 7.2: Distribution of topological charge density for lattice 704, after 24 steps of APE blocking.
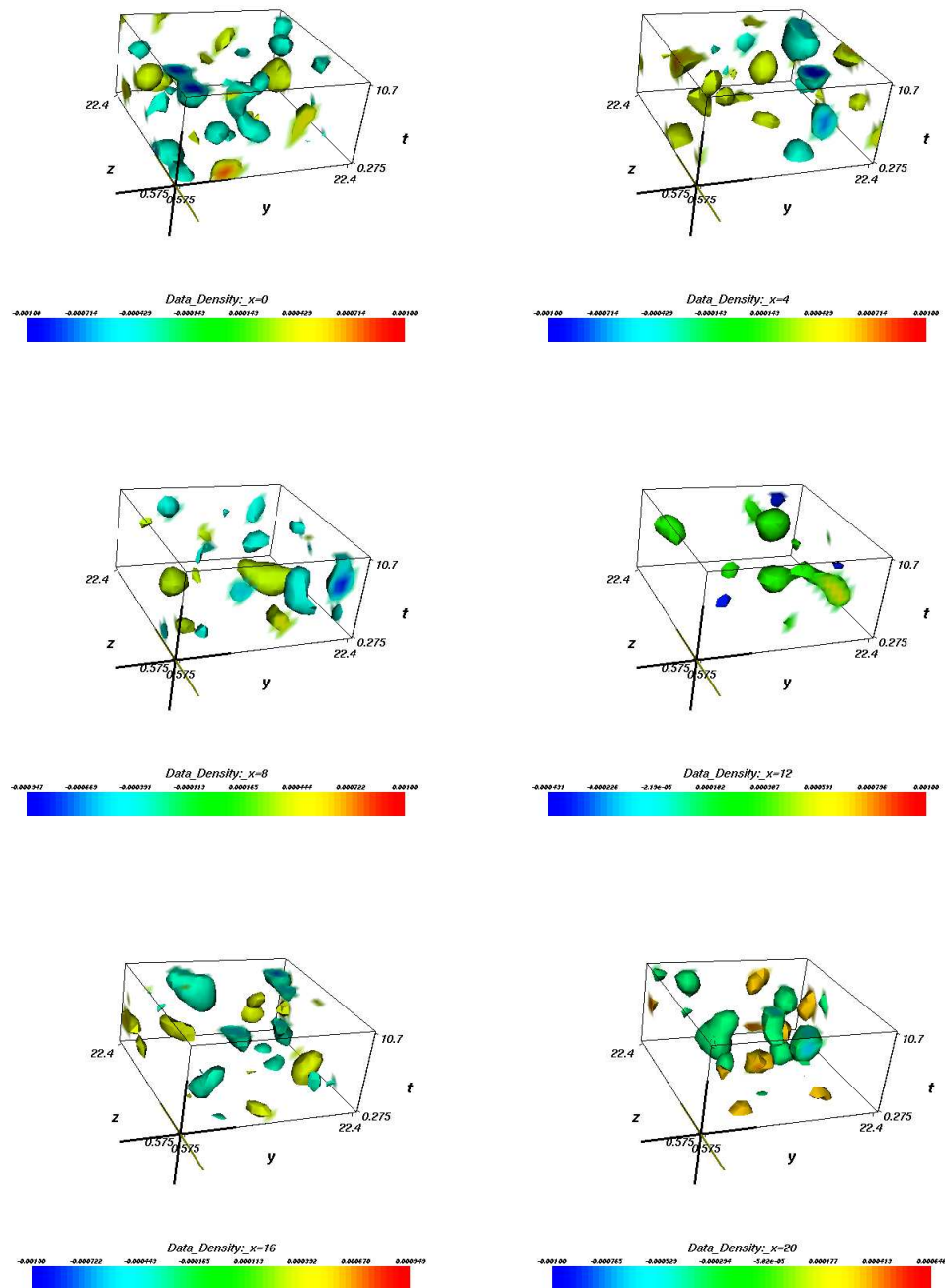
Figure 7.3: Topological charge density isosurfaces (lattice 704). $m_q = 0.008$, $\beta = 5.85$, 24 APE steps. Three-dimensional slices taken at $x = 0$, 4, 8, 12, 16, 20.
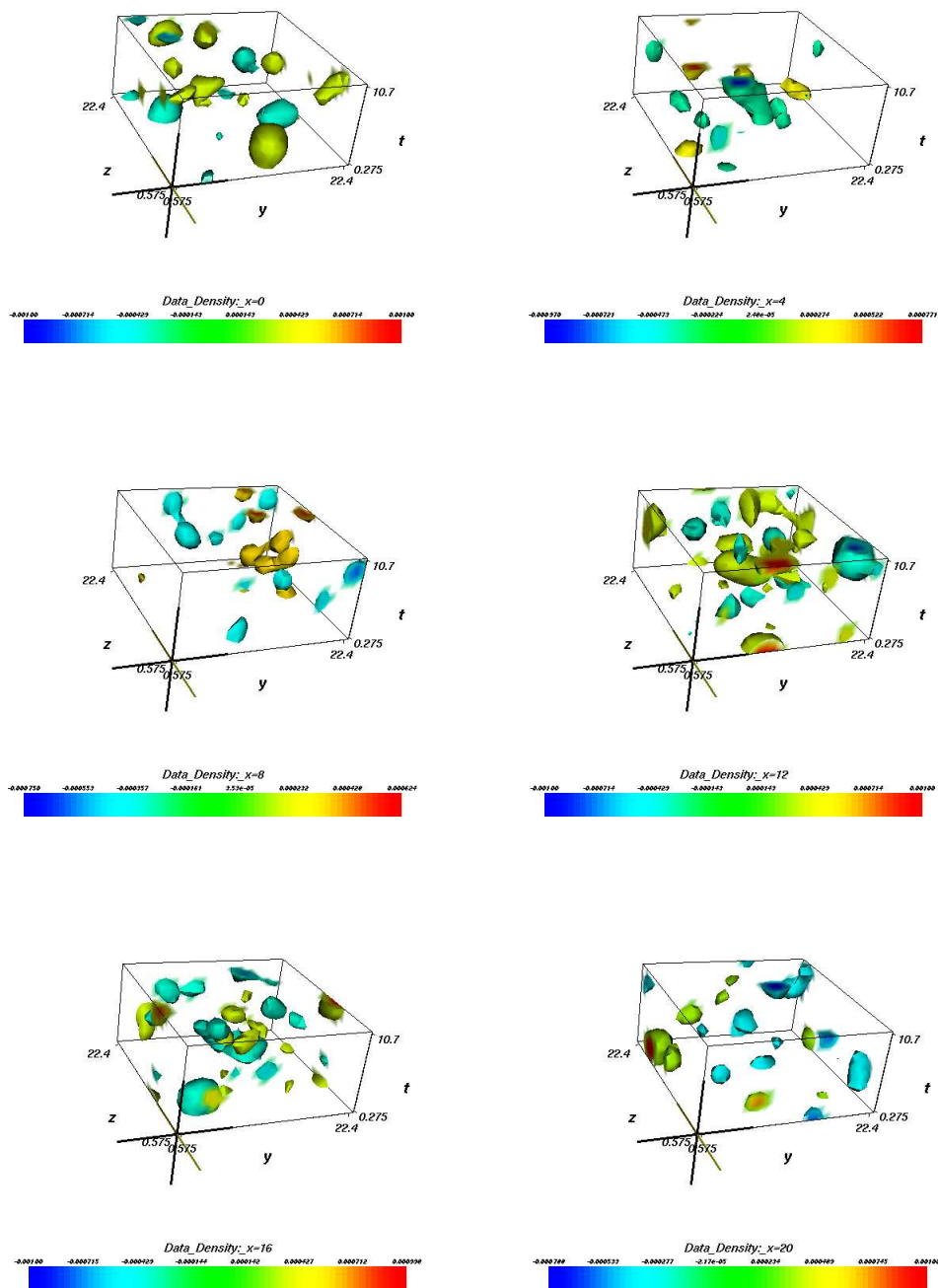
Figure 7.4: Topological charge density isosurfaces (lattice 1304). $m_q = 0.008$, $\beta = 5.85$, 24 APE steps. Three-dimensional slices taken at $x = 0, 4, 8, 12, 16, 20$.
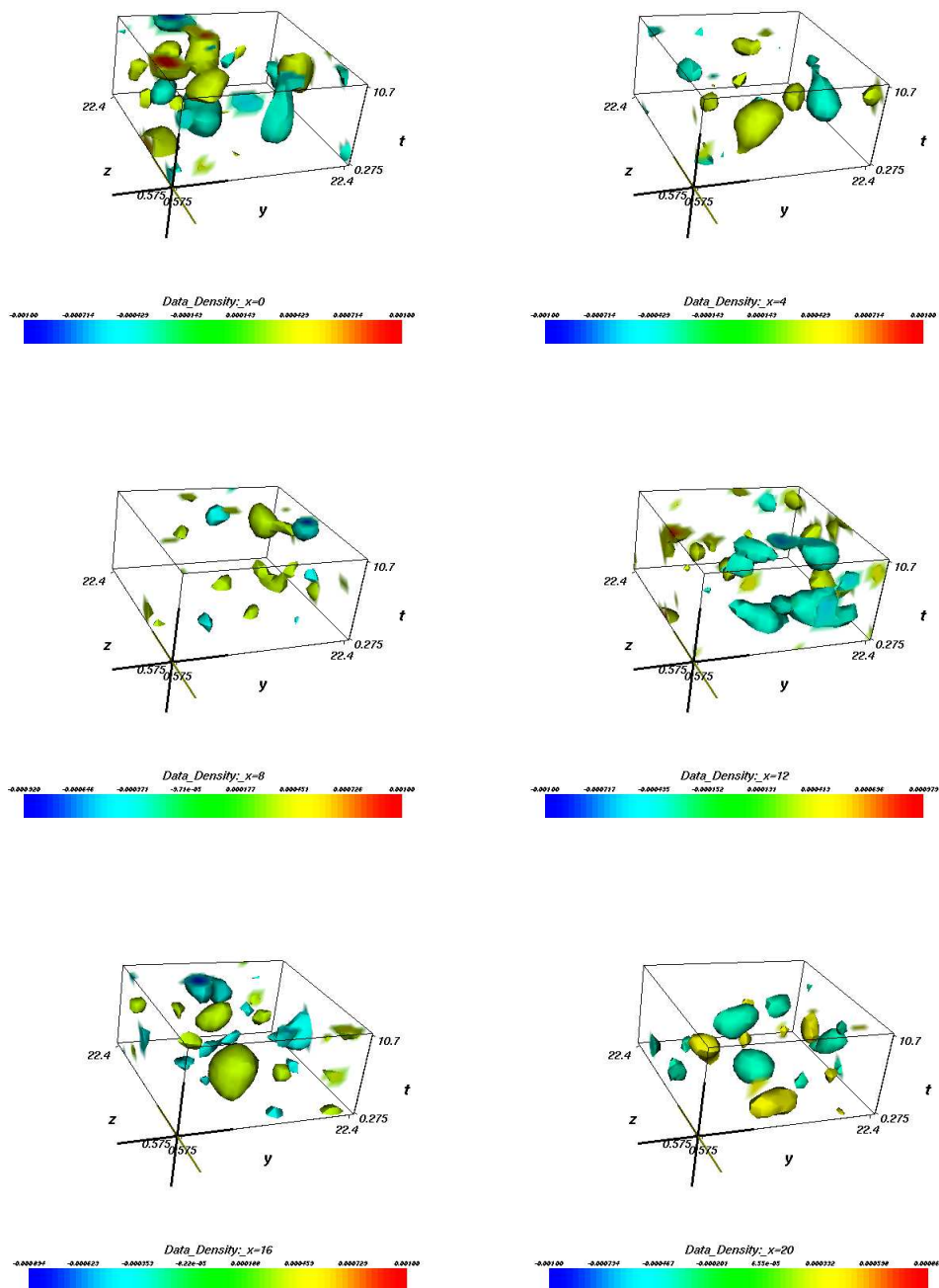
Figure 7.5: Topological charge density isosurfaces (lattice 1600). $m_q = 0.008$, $\beta = 5.85$, 24 APE steps. Three-dimensional slices taken at $x = 0$, 4, 8, 12, 16, 20.

sub-figures present three-dimensional slices of the full four-dimensional lattice taken at different values of the x coordinate, so the three axes displayed are y, z and t. Figures 7.4 and 7.5 show the same information for lattices 1304 and 1600 respectively.

As we can see in these figures, the real environment of a full QCD calculation is a far noisier and complex one than the schematic scenario we described in Chapter 6. First of all, we must remember that the BPST instanton is a solution for an isolated object in empty space, so the configurations we can actually find in a volume full of fluctuations only approximate the instanton. Furthermore, while the instantons are indeed minimum action solutions, there is no analytical result telling us that they are necessarily the only type of gauge structure possible. In fact we expect them to coexist with many other gauge structures driven by quantum fluctuations.

While we can not extract any quantitative information from these figures, they should serve as a caution against trusting too blindly the comfortable scenarios we described previously, and which have been used in the literature. In particular, after looking directly at many configurations we can state that we do *not* see, in any individual lattice, a structure of neatly aligned pairs polarized in the vertical direction. Of course, this does not mean that a statistically significant effect is not present, and we will now proceed to analyze the correlation results. But we do expect it to be a somewhat weak effect at best, since no sharp pair formation appears visible to the 'naked eye' in our dataset.

7.4   Comparison of APE and HYP blocking

We now turn our attention to the measurement of $c(r, t)$ on our dynamical lattices. As we have discussed before, we have a choice of algorithms for eliminating the random fluctuations which would otherwise swamp out most of the topology signal. We will concentrate on comparing APE and HYP blocking.

Since HYP blocking is essentially built from three APE levels with tunable
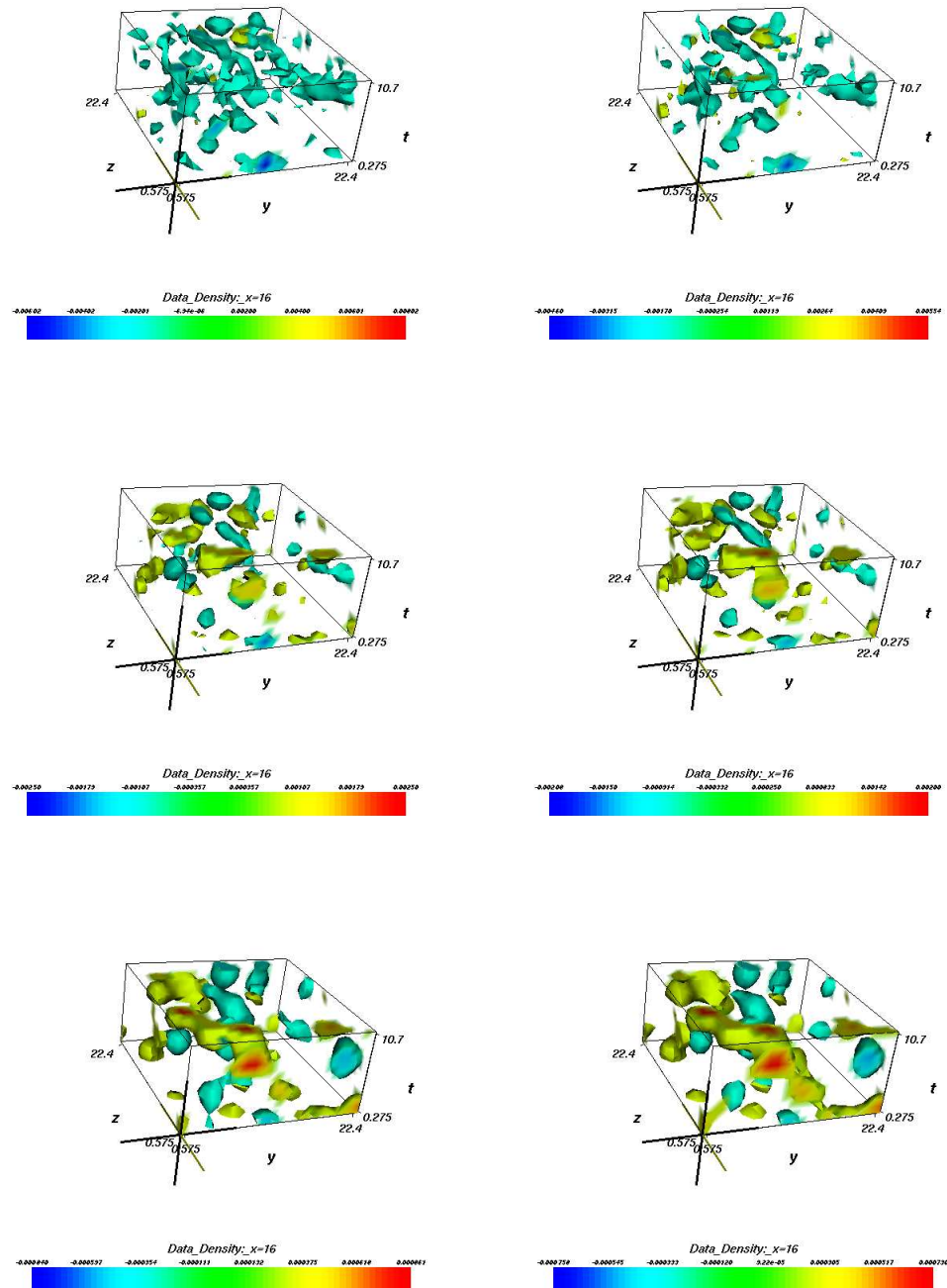
Figure 7.6: Comparison of APE and HYP blocking. The left column shows the effect of 6, 12 and 24 APE steps (top to bottom). The right column shows 2, 3 and 4 HYP steps.

parameters, we roughly expect to find a three-to-one correspondence between APE and HYP blocked lattices. Figure 7.6 shows in parallel the results of blocking a lattice repeatedly (6, 12 and 34 APE steps vs. 2, 3 and 4 HYP steps). We can see that while the two processes do not yield exactly identical results, the overall structure of both is very similar.

In order to guarantee that this is not a particular feature of an individual lattice we must look at the entire dataset. Figures 7.7 and 7.8 show the results of both types of blocking on the topological correlator, as measured for all 148 lattices with $m_q = 0.008$, $\beta = 5.85$.

From this we can safely conclude that, for our purposes of studying topological charge correlation, both algorithms provide equal results. This doesn't mean that they are identical in all respects, as the HYP blocking is particularly useful for studying flavor symmetry breaking issues. But for the problem we are interested in we can work with either of them.

Since we had completed the APE runs first, we made the decision to use APE blocking for the rest of the project.

7.5   The process of APE blocking

Having settled on the use of APE blocking, we must now choose how many steps to perform on our configurations before attempting to extract any conclusions. Again, let us first get a feel for how the blocking process affects a given configuration.

Figure 7.9 shows the results of performing 6, 9, 12, 18, 24 and 36 APE steps on a particular configuration. We can see how initially what we have is a large amount of small-scale noise with no discernible long-range structures. As the process removes these short-range fluctuations, larger features begin to appear. While numerically not identical, after reaching 18 APE steps the larger structures appear reasonably stable with most of the short-range noise removed.

Before making a decision we must however confirm the above picture with
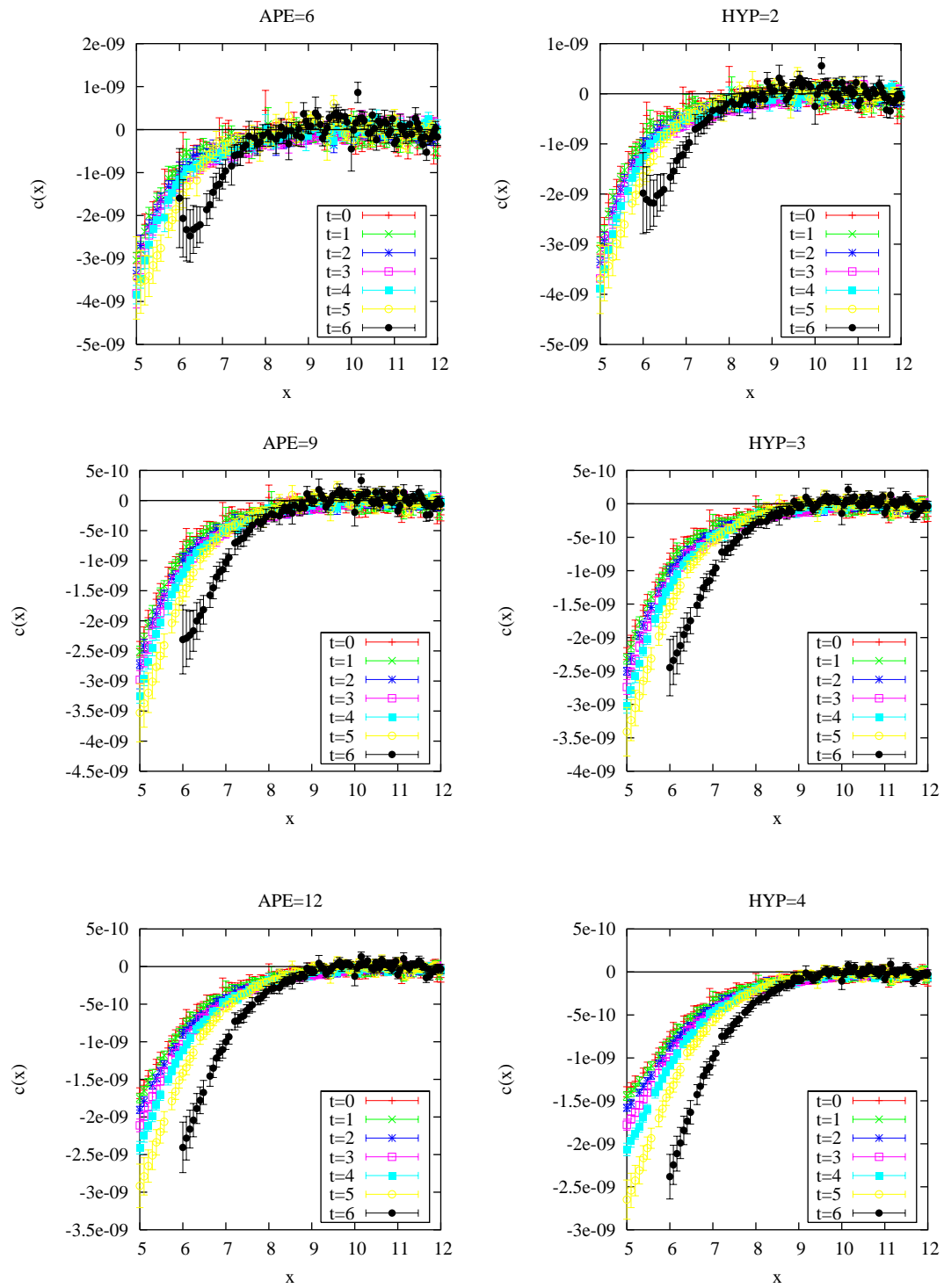
Figure 7.7: Comparison of APE and HYP blocking for $m_q = 0.008$, $\beta = 5.85$ lattices. Only the $x = [5, 12]$ region is shown.
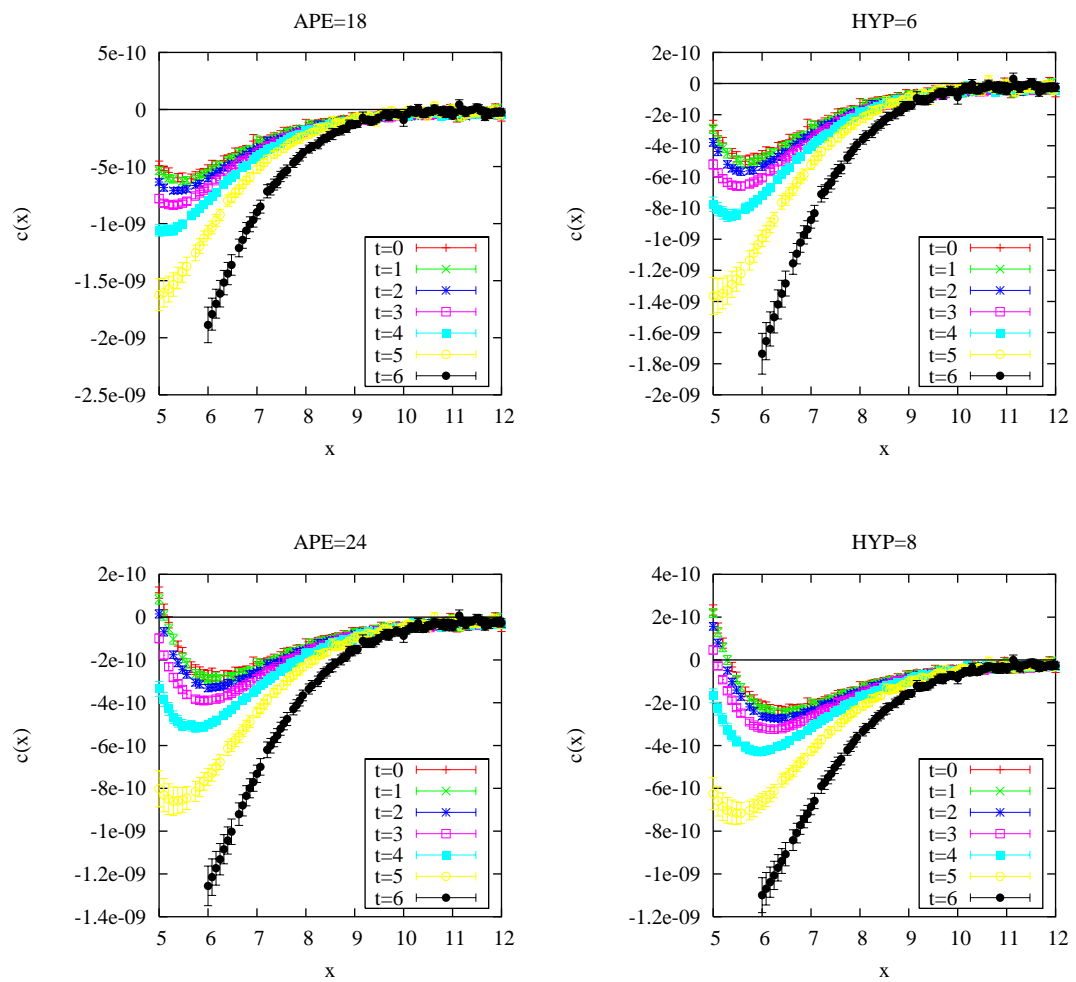
Figure 7.8: Comparison of APE and HYP blocking, continued.
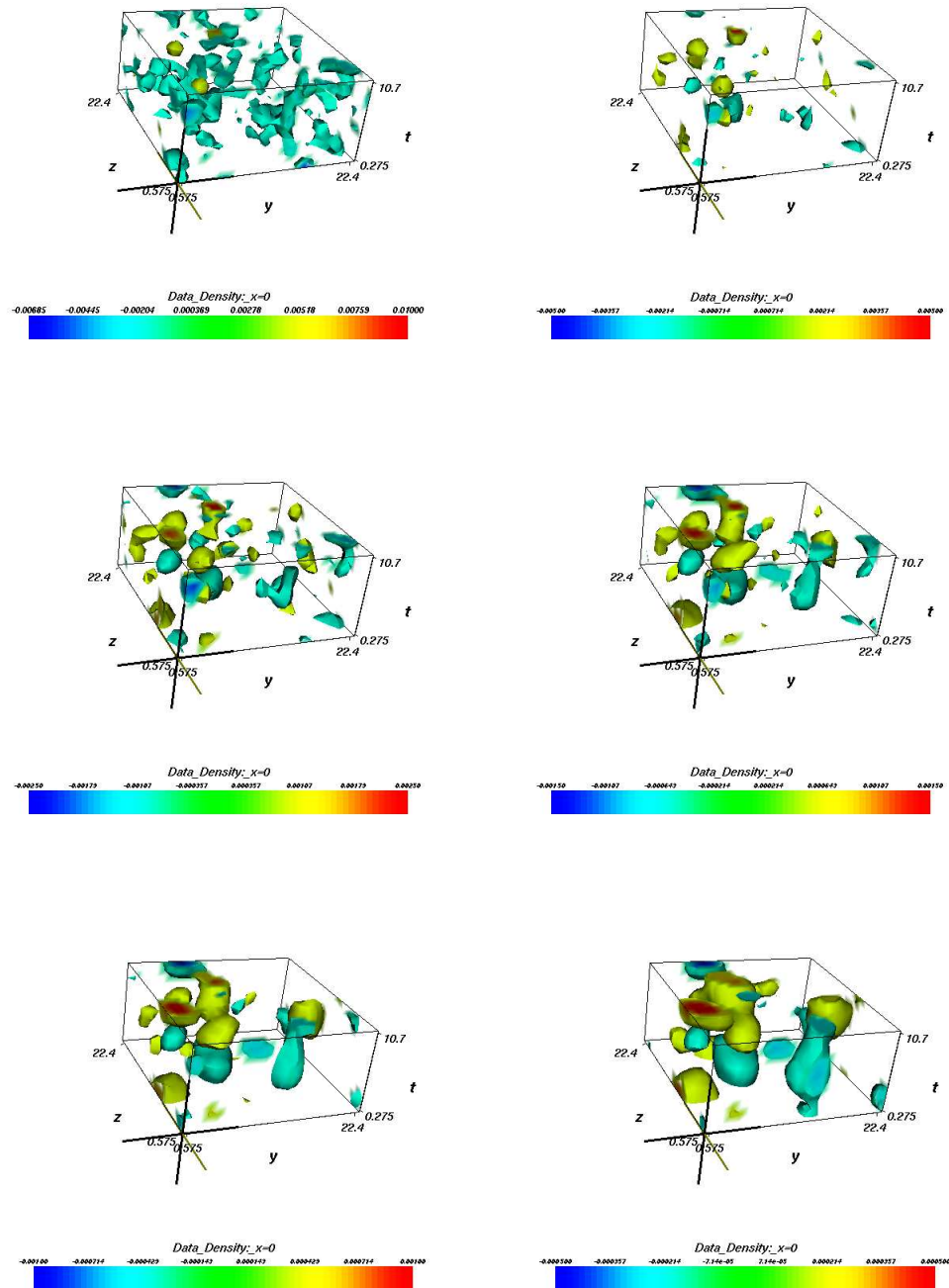
Figure 7.9: APE process shown for the $x = 0$ slice of lattice 1600 ($m_q = 0.008$, $\beta = 5.85$). From left to right and top to bottom, 6, 9, 12, 18, 24 and 36 APE steps shown.
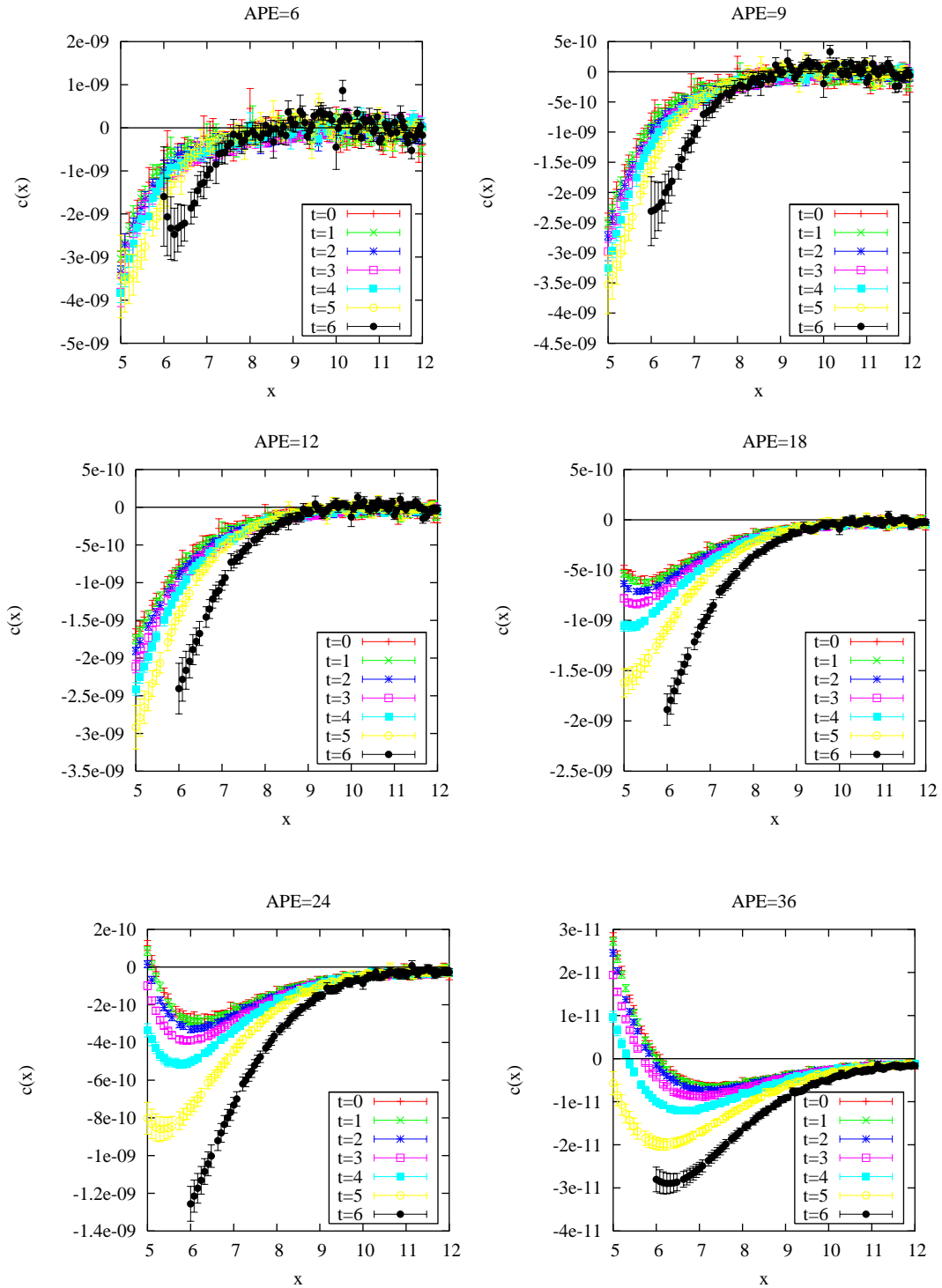
Figure 7.10: Effects of APE blocking on $c(r,t)$, shown for the full $m_q = 0.008$, $\beta = 5.85$ set of configurations. The plots corresponding to 6, 9 and 12 APE steps are taken from Fig. 7.7. Those for 18 and 24 steps are from Fig. 7.8. They are reproduced here in one figure to show the whole APE process.

the complete set of lattices. Figure 7.9 shows the effects of APE blocking on $c(r, t)$ for all the $m_q = 0.008$, $\beta = 5.85$ lattices. Similar results are obtained for all other m_q and β values.

We see from this that as we progressively remove all of the short-range noise, a time-dependent signal begins to appear. While the broad qualitative features of the three graphs at APE 18, 24 and 36 steps are similar, we chose to use 24 steps for the rest of the study. It appears as a reasonable balance between having removed most of the short-range fluctuations and not distorting too much the topology.

7.6   Correlation Measurements at 24 APE Steps

Having settled on using 24 APE blocking steps for our analysis, we proceed to measure the topological correlator $c(r, t)$ on the entire dataset.

Figure 7.11 shows the $c(r, t)$ results (where $x = \sqrt{r^2 + t^2}$) for all β values with $m_q = 0.008$ and 24 APE steps. This should be compared to Fig. 7.1 with the same measurements performed on the set of quenched configurations. We immediately see that there is indeed a qualitatively significant difference between the two scenarios. The negative dip in $c(x)$ at larger distances can be attributed to a correlation between objects of opposite topological charge.

Figures 7.12 and 7.13 show the results of performing the same measurements for the $m_q = 0.016$ dataset, with results qualitatively similar to those at the lighter quark mass.

The quenched configurations show essentially no negative correlation at all, which indicates a statistically vanishing pairing of oppositely charged objects, as one would expect in the absence of dynamical fermions to mediate their interactions.

Furthermore, in these plots we see that the negative correlation is not only present, but also anisotropic. The higher time slices show larger negative values, which fits nicely into our intuitive model of pairing in the temporal direction.

Before making any direct conclusions, however, we must take into account
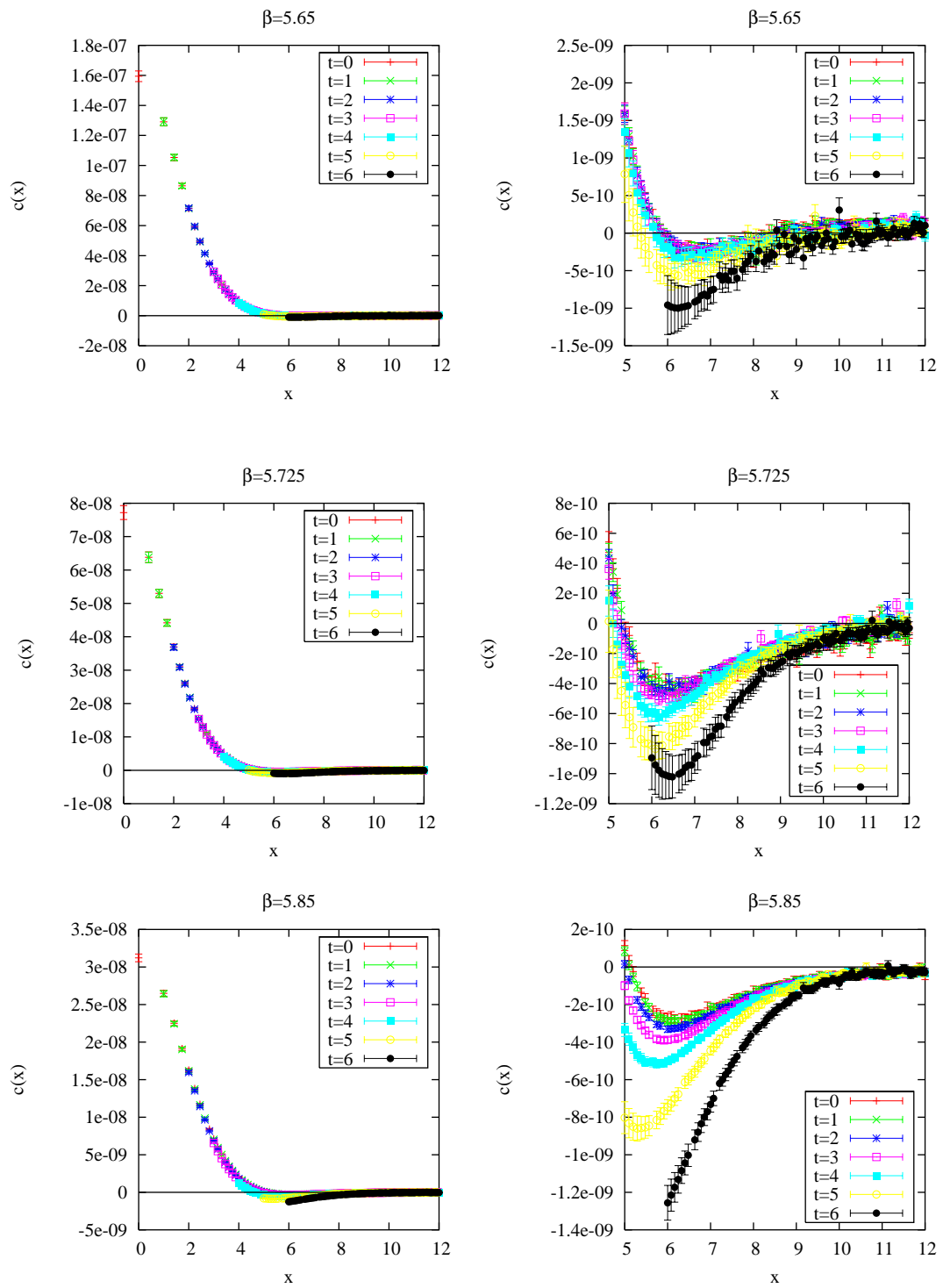
Figure 7.11: Topological correlator for all β values with $m_q = 0.008$ and 24 APE steps. The second column shows a detail of the $x = [5, 12]$ region.
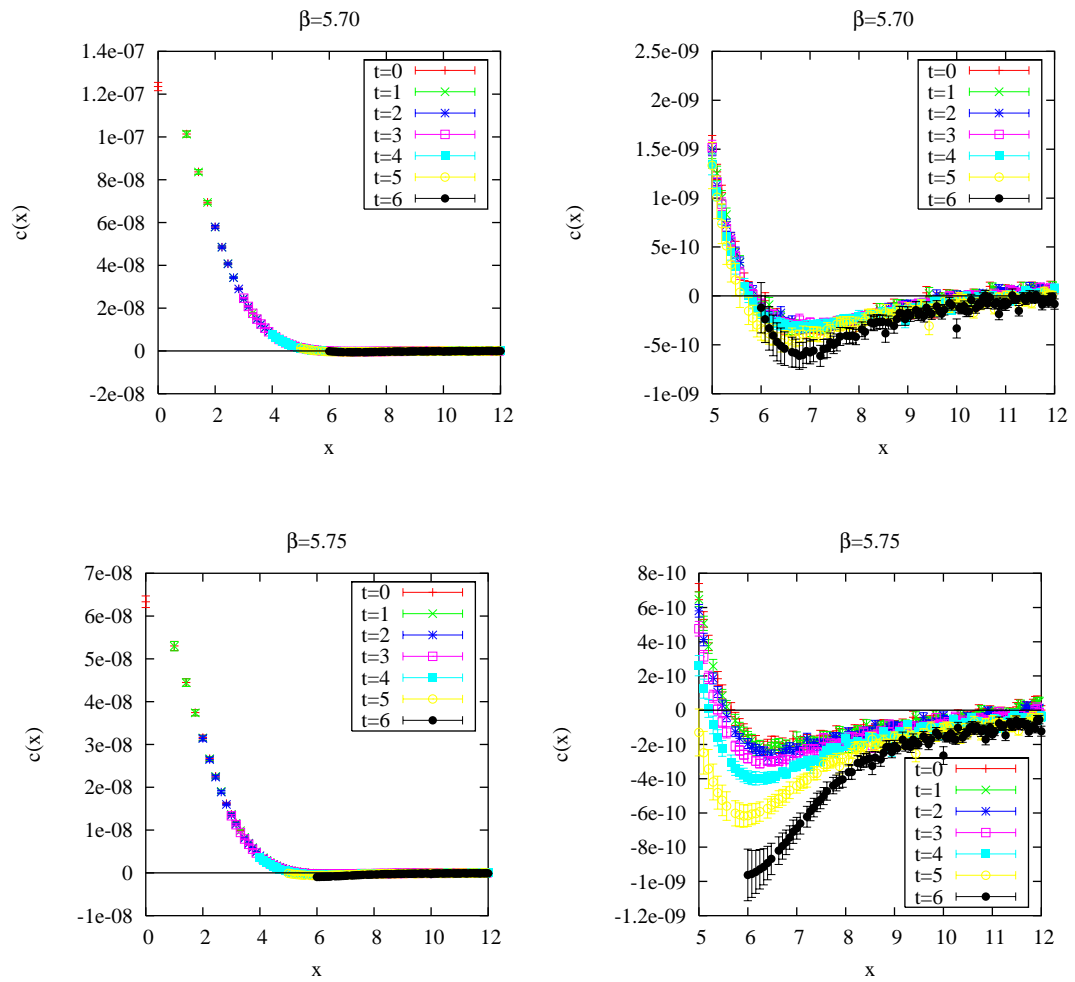
Figure 7.12: Topological correlator for all β values with $m_q = 0.016$ and 24 APE steps.
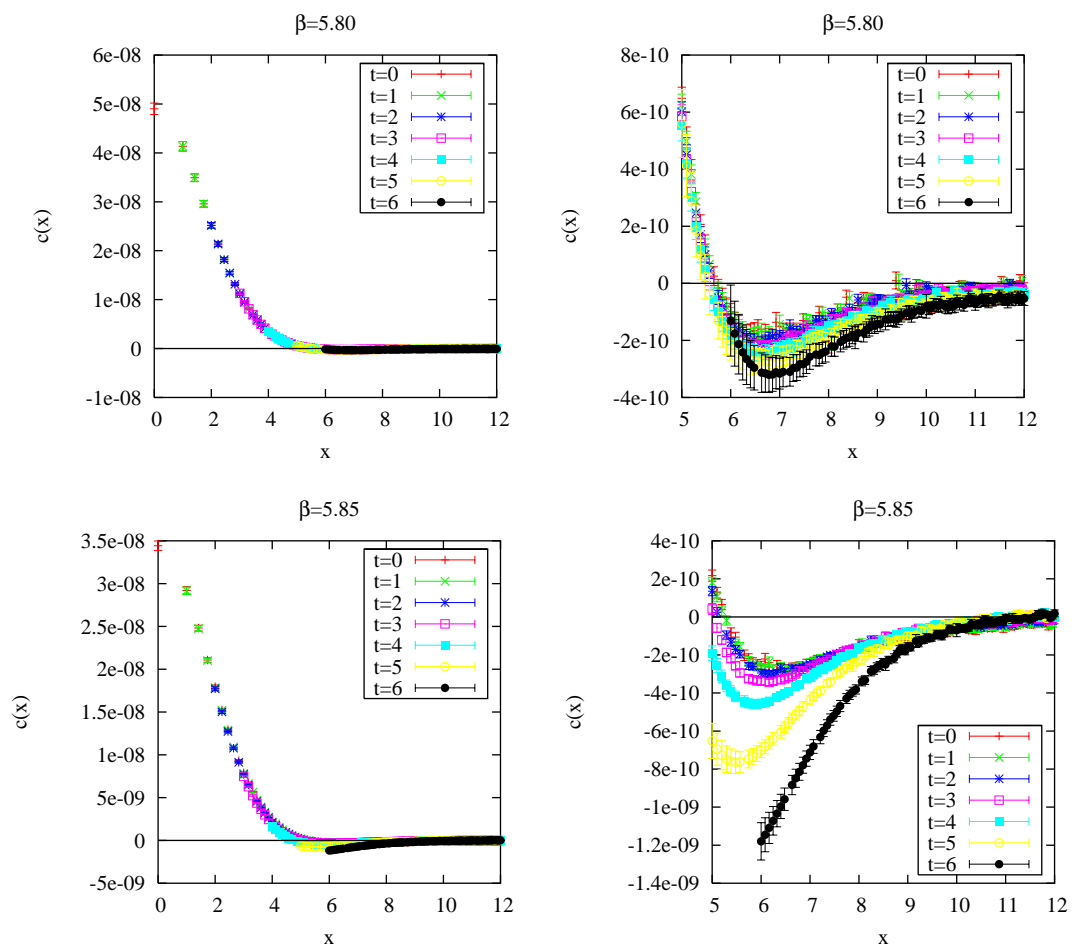
Figure 7.13: Topological correlator for $m_q = 0.016$, continued.

the periodicity of the lattice. Since the boundary conditions on the gauge fields are periodic, we in fact have an overcounting which becomes fairly significant for the higher time-slices. We now turn our attention to this issue before trying to make any conclusions about the presence of an anisotropy in these measurements.

Note however that the significant pairing correlation, in contrast to the behavior observed in for the quenched configurations, is not affected by the overcounting.

7.7   Addressing the Effects of Periodicity

In order to correctly establish whether there is a statistically significant anisotropy in the topological correlation measurements, we must control the effects of overcounting through the lattice periodicity.

Since at $t = N_t/2$ the overcounting is exactly a factor of 2, we should compare the $t = 0$ data against the $t = N_t$ data, divided by 2. Only if this comparison shows a statistically significant difference can we make a valid conclusion about the presence of anisotropy in the dynamical configurations.

Figure 7.14 shows the results of this process for the $m_q = 0.008$ at all β values. We can see that in fact, for values of β above the estimated crossover, we have indeed a statistically significant effect. For smaller β the pair correlation remains present, but we can not claim a significant anisotropy, as most of the apparent effect previously seen can be accounted for as an overcounting artifact.

Figure 7.15 shows the corresponding results for $m_q = 0.016$. It is not completely clear to us why the apparent increase and later decrease of the effect for the $m_q = 0.016$ data, but we will comment a bit on this in the next section after we try to quantify this effect better.

From these results we can conclude that there is a definite anisotropic pairing of instantons and anti-instantons, in agreement with the Shuryak picture. We will now try to quantify this effect by using a simple model for the pair distribution.
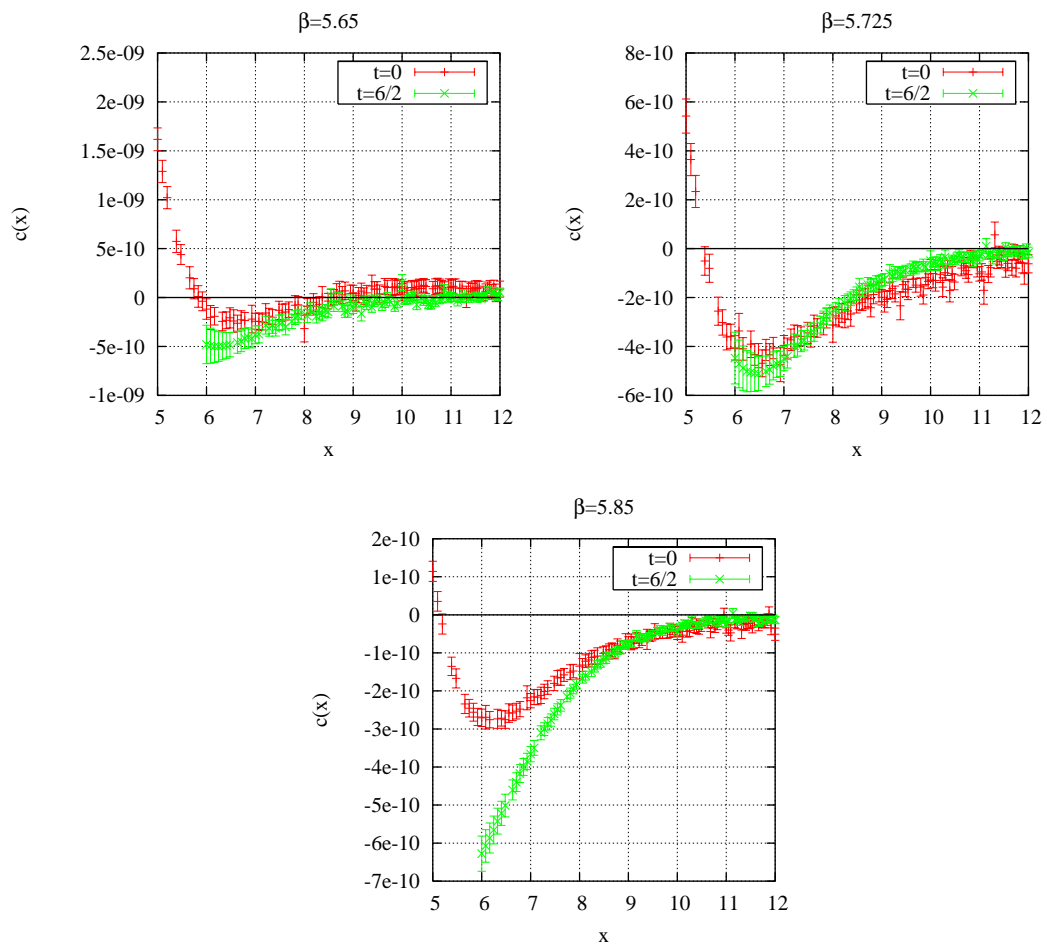
Figure 7.14: Comparison of the $t = 0$ data with the $t = 6$ data divided by 2, for $m_q = 0.008$ at all β values.
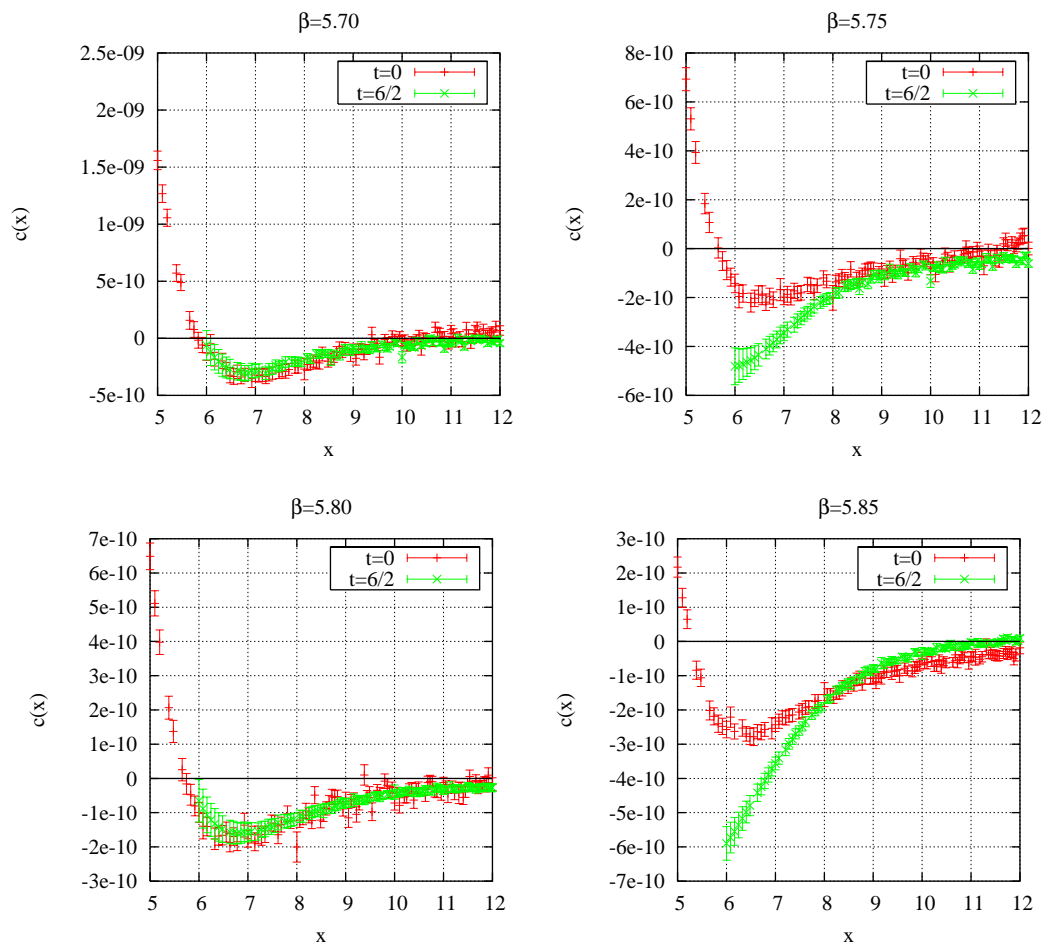
Figure 7.15: Comparison of the $t = 0$ data with the $t = 6$ data divided by 2, for $m_q = 0.016$ at all β values.

7.8 Simple Pairing Model

At this point we have seen statistically convincing evidence of an anisotropic negative correlation in the topological charge density of dynamical configurations, which is not present for quenched ones. Intuitively this can be interpreted as the effect of pairing of regions with opposite topological charge. In order to try to quantify this effect better, we will use a simple model of randomly distributed instantons and I-A pairs to describe $c(x)$, following the lines of [37].

We will model the charge distribution as a collection of separate instantons and anti-instantons, whose field strength (squared) is given by

$$F_{\mu\nu}^2(x;\rho) = F_{\mu\nu}(x;\rho)F^{\mu\nu}(x;\rho) = \frac{192\rho^4}{(x^2 + \rho^2)^4} \tag{7.2}$$

where ρ is the "radius" of the pseudo-particle, a parameter which characterizes the spatial extent of the fields. For a single particle this leads to the charge density

$$q_0(x;\rho) = \frac{1}{32\pi^2}F_{\mu\nu}^2(x;\rho) = \frac{6}{\pi^2}\frac{\rho^4}{(x^2 + \rho^2)^4}. \tag{7.3}$$

from which we can compute explicitly the single-particle correlation which will be our basic building block as

$$c_0(x;\rho) = \frac{1}{V}\int d^4x'\, q_0(x')q_0(x' + x) \tag{7.4}$$

With a little algebra this becomes

$$c_0(z;\rho) = \frac{1}{V}\frac{36}{\pi^4\rho^4}\omega(q) \tag{7.5}$$

where the parameter q is defined as

$$q = \frac{z}{2\rho} \tag{7.6}$$

and the function $\omega(q)$ is defined through the integral

$$\omega(q) = \int d^4y \ \{[(y-q)^2 + 1][(y+q)+1]\}^{-4}.$$

(7.7)

The spherical coordinates $(r, \theta_1, \theta_2, \phi)$ in four dimensions are defined through the transformation equations

$$\begin{cases} x &=& r\sin\theta_2 \sin\theta_1 \cos\phi \\ y &=& r\sin\theta_2 \sin\theta_1 \sin\phi \\ z &=& r\sin\theta_2 \cos\theta_1 \\ t &=& r\cos\theta_2 \end{cases}$$

(7.8)

With these, the 3-d angular integral can be performed explicitly and the remaining expression, which will have to be evaluated numerically, is

$$\omega(q) = \frac{\pi^2}{2^{10}q^8} \int_0^\infty dy \ \frac{1}{y^5} \frac{5 - 12g(y,q) + 8g^2(y,q)}{g^{7/2}(y,q) \left[g(y,q) - 1\right]^{5/2}}$$

(7.9)

with the function $g(y,q)$ being

$$g(y,q) = \left(\frac{y^2 + q^2 + 1}{2yq}\right)^2.$$

(7.10)

Now, if we are to model the topological charge density on the lattice as a collection of N_0 reasonably well separated instantons and N_p instanton–anti-instanton (IA) pairs, we can write the charge correlator as

$$c(x) = N_0 c_0(x) - N_p c_p(x),$$

(7.11)

where $c_p(x)$ is a function representing the correlation for an IA pair. If we had a

charge distribution consisting of a single pair separated by a four-vector d,

$$q(x) = q_0(x) - q_0(x + d), \tag{7.12}$$

then

$$c_p^1(x) = 2c_0(x) - c_0(x + d) - c_0(x - d). \tag{7.13}$$

Since in any given lattice we expect to find many randomly oriented pairs, we must then average this pair correlator over all possible orientations of d. Noting that

$$\langle c_0(x + d) \rangle_d = \langle c_0(x - d) \rangle_d, \tag{7.14}$$

we can write the direction-averaged pair correlator as

$$c_p(x) = 2 \left[c_0(x) - \langle c_0(x + d) \rangle_d \right]. \tag{7.15}$$

With this form we can then use the following form to model our correlation measurements:

$$c(x) = N_0 c_0(x) - N_p c_p(x) = n_a c_0(x) + n_b c_0^{\mathrm{av}}(x), \tag{7.16}$$

where

$$c_0^{\mathrm{av}}(x) = \langle c_0(x + d) \rangle_d, \tag{7.17}$$

$$N_0 = n_a + n_b, \tag{7.18}$$

$$N_p = \frac{n_b}{2}. \tag{7.19}$$

The average $c_0^{\mathrm{av}}(x)$ can be computed from the above form of $c_0(x)$ by integrating

over all orientations of d, and is given by

$$c_0^{\text{av}}(x;\rho,d) = \frac{288}{\pi^5 V \rho^2 xd} \int_{\frac{|d-x|}{2\rho}}^{\frac{|d+x|}{2\rho}} dy \, y \, \omega(y) \sqrt{1 - \frac{4\rho^2 y^2 - d^2 - x^2}{2xd}}. \tag{7.20}$$

7.9 Fitting the Correlation Data

When attempting to use Eq. (7.16), we must note the fact that the $t = 6$ data lacks information about the close distances, and it is therefore impossible to reliably obtain N_0 and ρ from it. The process we used was then to fit the $t = 0$ data to (7.16), and using the values of (N_0, ρ) obtained from this, fit the $t = 6$ (suitably rescaled by a factor of 2) data.

The results of this process are shown in Table 7.3. The pairing fraction f_p, defined as

$$f_p = \frac{2N_p}{N_0}, \tag{7.21}$$

represents the fraction of objects on the lattice which are forming IA pairs.

The results of these fits are shown in Figure 7.16 for the $m_q = 0.008$ configurations, and in Figures 7.17 and 7.18 for the $m_q = 0.016$ set. We can indeed obtain a fairly good description of our data using this model, as can be seen from these figures.

In Table 7.4 we have computed the ratio of pairing fractions between the $t = 6$ and the $t = 0$ data for all configurations. This ratio is an indicator of how strongly the pairing effect changes with respect to the time slice considered. These results are shown in Figure 7.19, along with the estimated crossover boundaries.

We observe an increase in the anisotropy of the pairing for the configurations which are well above the crossover. The effect is marginally significant for the $m_q = 0.008$ case, as we had expected already from both the correlation data and our inspection of the configurations themselves.

Table 7.3: Fit results using Eq. (7.16). The $t = 6$ data has been rescaled by a factor of 2 before fitting it.

m_q	β	t	ρ	d	N_0	N_p	f_p
0.008	5.65	0	2.53 ± 0.05	4.4 ± 0.4	15 ± 2	1.0 ± 0.2	0.13 ± 0.03
		6		4.5 ± 1		1.2 ± 0.2	0.16 ± 0.03
	5.725	0	2.56 ± 0.01	5.3 ± 0.2	7.9 ± 0.2	0.70 ± 0.06	0.18 ± 0.02
		6		5.56 ± 0.05		0.66 ± 0.06	0.17 ± 0.02
	5.85	0	2.90 ± 0.05	4.26 ± 0.02	5.9 ± 0.4	0.76 ± 0.08	0.26 ± 0.03
		6		4.08 ± 0.04		0.98 ± 0.04	0.33 ± 0.03
0.016	5.70	0	2.58 ± 0.01	4.94 ± 0.15	12.22 ± 0.04	0.87 ± 0.03	0.142 ± 0.005
		6		5.4 ± 0.2		0.76 ± 0.06	0.125 ± 0.010
	5.75	0	2.76 ± 0.04	4.3 ± 0.2	9.0 ± 0.3	0.88 ± 0.02	0.196 ± 0.008
		6		5.0 ± 0.2		0.89 ± 0.05	0.198 ± 0.013
	5.80	0	2.79 ± 0.08	4.5 ± 0.4	7.2 ± 0.9	0.70 ± 0.13	0.194 ± 0.04
		6		5.3 ± 0.7		0.56 ± 0.12	0.156 ± 0.04
	5.85	0	2.87 ± 0.06	4.4 ± 0.2	6.1 ± 0.3	0.74 ± 0.08	0.24 ± 0.03
		6		4.14 ± 0.14		0.95 ± 0.14	0.31 ± 0.05
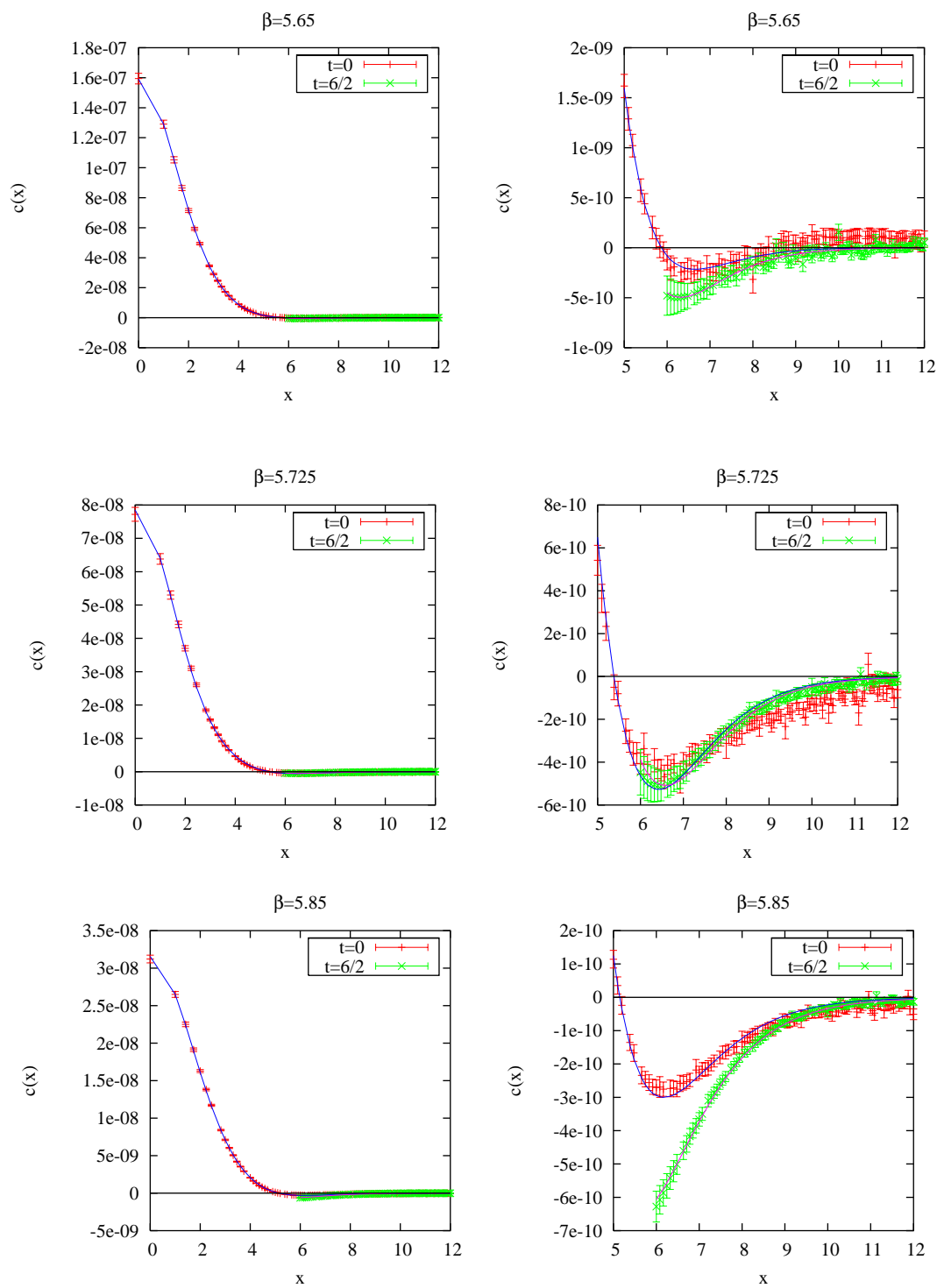
Figure 7.16: Data fit to Eq. (7.16) for the $m_q = 0.008$ configurations, with the $t = 6$ data rescaled by a factor of 2.
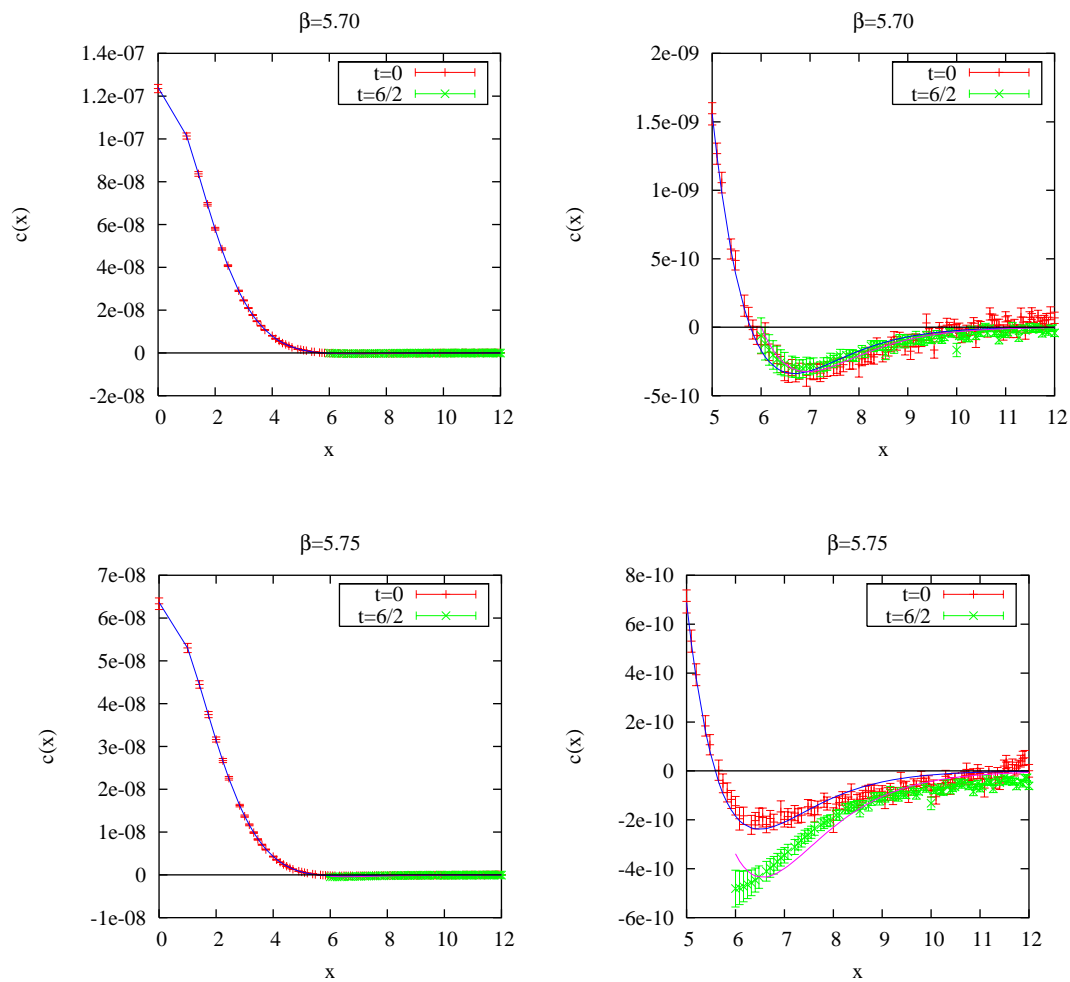
Figure 7.17: Data fit to Eq. (7.16) for the $m_q = 0.016$ configurations, with the $t = 6$ data rescaled by a factor of 2.
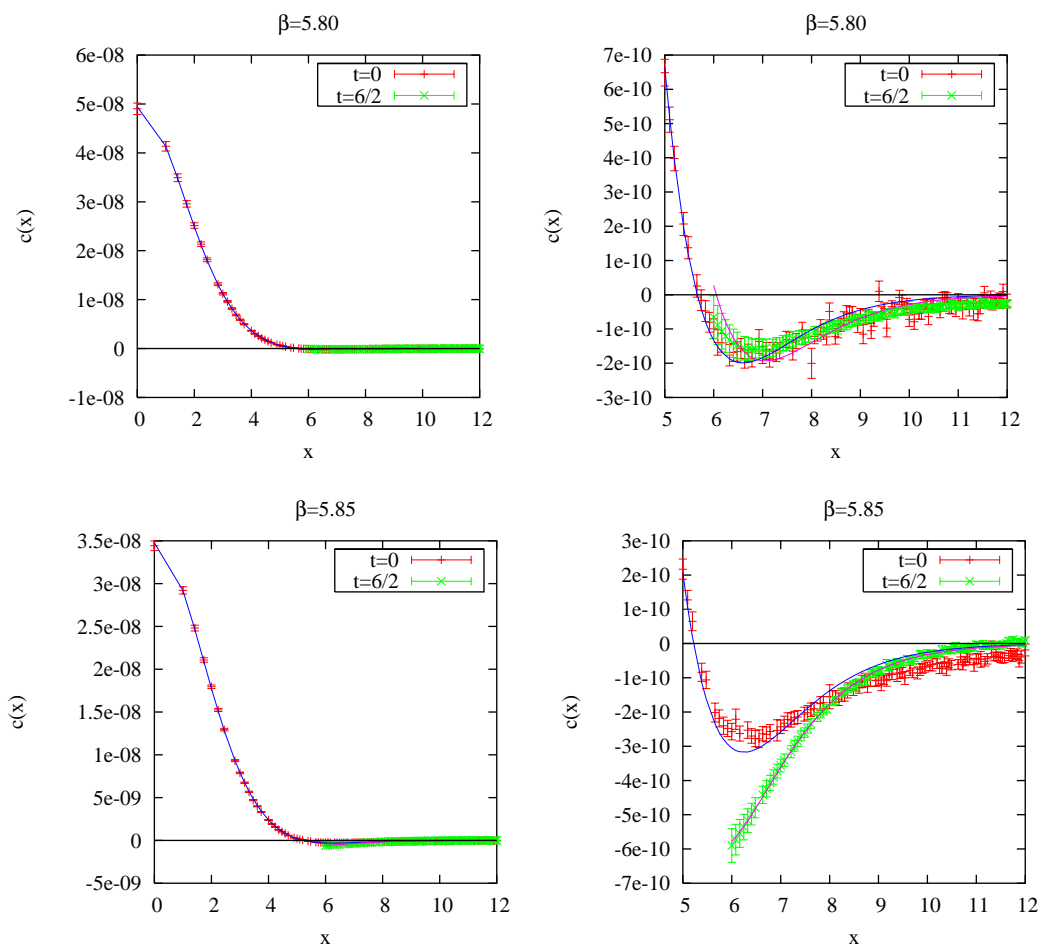
Figure 7.18: Data fit to Eq. (7.16) for the $m_q = 0.016$ configurations, continued.

Table 7.4: Ratio of pairing fractions between the $t = 6$ and the $t = 0$ data for all configurations.

m_q	β	f_{p6}/f_{p0}
	5.65	1.2 ± 0.4
0.008	5.725	0.94 ± 0.12
	5.85	1.3 ± 0.2
	5.70	0.88 ± 0.07
0.016	5.75	1.01 ± 0.08
	5.80	0.8 ± 0.3
	5.85	1.3 ± 0.3

The puzzling behavior shown by the $\beta = 5.80$ data at $m_q = 0.016$, which we discussed before, may be caused by correlation artifacts of the original dataset. In Table 7.5 we present the results for the total charge $\langle Q \rangle$, $\langle Q^2 \rangle$ and the susceptibility $\langle \chi \rangle^{1/4}$. The fact that we find repeated occurrences of $\langle Q \rangle \neq 0$ suggests that these lattices may have been poorly decorrelated with respect to the topological background. Because the topological properties of the background depend on long-range structures, in general their autocorrelation times are much longer than those of other observables. This issue is currently under investigation.
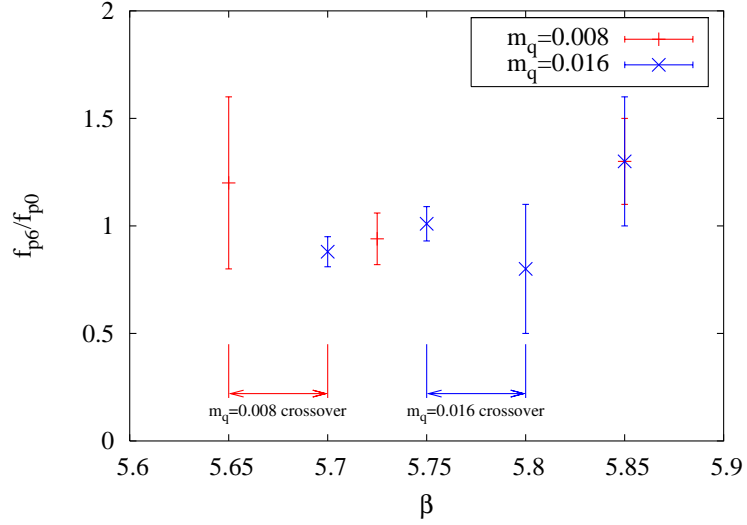
Figure 7.19: Ratio of the pairing fractions for the $t = 6$ and the $t = 0$ data for all configurations. The estimated boundaries for the crossover are indicated by the vertical lines for each quark mass value.

Table 7.5: Topological charge and susceptibility for all the lattices analyzed. The lattice spacing is shown and used to convert the susceptibility to physical units.

m_q	β	a (fm)	$\langle Q \rangle$	$\langle Q^2 \rangle /V \times 10^8$	$\langle \chi \rangle^{1/4} \times 10^2 \, \mathrm{GeV}$
0.008	5.65	0.112	-1.61 ± 0.18	15.9 ± 0.4	3.52 ± 0.02
	5.725	0.099	0.23 ± 0.11	7.72 ± 0.20	3.32 ± 0.02
	5.85	0.093	0.00 ± 0.01	3.12 ± 0.05	2.82 ± 0.01
0.016	5.70	0.118	0.20 ± 0.15	12.4 ± 0.2	3.14 ± 0.01
	5.75	0.116	-0.19 ± 0.09	6.28 ± 0.14	2.69 ± 0.02
	5.80	0.114	0.65 ± 0.07	4.82 ± 0.12	2.57 ± 0.02
	5.85	0.111	0.39 ± 0.04	3.44 ± 0.05	2.42 ± 0.01

Chapter 8

Visualization of Lattice Quantities

Because lattice calculations are done via Monte Carlo methods, in practice one must collect aggregate data from many configurations and for many purposes regular two and three dimensional plotting programs are sufficient for looking at the results. But as we have seen in this project, it may be useful to be able to directly study the raw lattice data, as it may provide first hand evidence of the actual structure of the lattice itself. In the previous chapter we used this kind of information to guide our analysis of the topological structure and to contrast direct observations against the naïve expectations from simple models. In this chapter we will describe these tools and present some of the other interesting uses which can be made of them for probing lattice QCD structure.

8.1   A Mixed Language Approach

Before discussing the details of our visualization system, let us make a brief detour into the methodology used to develop it. The daily toolbox of any computational physicist tends to be a somewhat eclectic mix of large programs written in languages like C and FORTRAN, controlled by a collection of scripts written typically in languages like sh, sed, awk, and more recently Perl or Python.

While this approach of loosely bound scripts controlling monolithic applications has proven to be useful for a long time, it is not without its complications. Typically this means that making changes to the important cores of the applications

is a delicate and often difficult process, as large scientific codes have a tendency to be complex and under-documented. And it also means that the core codes must worry about issues such as user input/output, data storage or string parsing which are often rather clumsy and error-prone operations in languages such as C and FORTRAN. It is not uncommon to hear of scientific collaborations where these problems lead the various members of a group to each keep his or her own copy of the core code, making small changes to adapt to his research interests but breaking the modularity and integration of the overall code and making it difficult to propagate these changes back into the main project [7].

In recent years an alternative approach has been gaining ground in the scientific computing community. The idea is to strip the compiled language core to its bare essentials where numerical performance is paramount, and turn it into a set of libraries with well defined interfaces but no overall control. Such libraries can then be controlled via a high-level language where the global logic resides, but where performance is a secondary concern. It is typical of scientific programs to spend upwards of 90% of their CPU time in a key numerical core, and if this core is well optimized, in the long run all the rest of the program can be written in a slower but more convenient language without significant negative impact.

For this approach to work, it must be possible to access the compiled core libraries from within the high-level language in a direct and natural manner. This is not necessarily a trivial task, and it requires both careful design and implementation.

The advantages of this approach, when properly implemented, can be many. First of all, high level languages are often interpreted; while this presents a performance problem, it has the advantage of drastically simpler development cycles compared to compiled languages. They also tend to be very expressive and to offer natively complex data types such as lists and hash tables which simplify the organization of overall logic. Finally, these languages tend to have very comprehensive libraries for many tasks not often found in languages like C or Fortran. Doing regular

expression processing, html generation, image manipulation or communicating over the internet with a remote server is often a matter of a few lines of code in these languages. Similar tasks in C are often complex and delicate enough that they are simply not done inside the language by scientific programmers.

There are many such languages today to choose from, with Perl and Python being the most popular. In the scientific community, Python [82] is rapidly gaining popularity for a number of reasons. It is a language with a very simple but expressive syntax, an elegant mechanism for Object Oriented Programming whose syntax is far cleaner than that of C++ or Java, a large set of powerful libraries, and some features specifically useful to scientific computing users:

(1) A powerful set of extensions for numerical computing, known as NumPy, has been developed and is actively maintained [4]. NumPy gives Python capabilities roughly equivalent to that of systems like IDL or MatLab, with the added benefit of a far superior language and the support of libraries for other non-numeric tasks.

(2) Python was designed from the ground up to be easily extended in C (most of NumPy is in C). This means that wrapping existing libraries in C or even FORTRAN is a relatively easy task. There exist tools which automate most of this process, such as SWIG [6] for C/C++ and f2py [60] for FORTRAN.

(3) Recent developments such as the weave project [48] allow for the inclusion of C code inlined as part of a Python program. The code is automatically compiled on the fly, eliminating the need to manually write extension modules.

There exist many scientific projects which have adopted Python as their overall control/scripting language. For example, the blueprint for future development of analysis software at the LHC (CERN) has chosen Python as a key component for the integration of the complex set of systems and libraries which LHC will use [3].

For our project we decided to use Python both for the analysis of most of the data and for the three dimensional visualization problem. We developed an environment called IPython for interactive use [64] which provides facilities similar to those of the Mathematica or MatLab interpreters, with many enhancements. This is useful both for code development and for interactive data analysis, as it provides direct access to the Gnuplot plotting package.

Visualizing three-dimensional data is a computationally demanding task, and an all Python approach to this problem would produce unacceptably slow performance. But the VTK rendering toolkit [71], written in C++, is a very efficient and comprehensive system which we can use for our purposes. It is actively maintained and can take advantage of accelerated rendering hardware present in modern video cards. Furthermore, VTK comes with a set of Python bindings, which suits our purposes very well.

On top of VTK, the MayaVi data visualizer [65] has been developed as a graphical front end with interactive capabilities for real-time manipulation of the data. MayaVi itself is written in Python, which means that it can be also controlled via another program and not only from its graphical interface.

Our approach was then to build on top of MayaVi and VTK by writing a set of Python classes and utilities to load and process the information from lattice simulations, prepare them for processing and control a MayaVi instance for the final visualization. A screen capture of the resulting MayaVi process is shown in Figure 8.1. At this point the MayaVi process is active and the user can manipulate the plotting region, rotate it in real time, modify the parameters of the visualization and save the output to a number of formats.

The code is currently capable of understanding topological density and fermionic eigenmode files, and is easily extensible to other quantities. It has methods for computing histograms of the full four-dimensional sets and take three-dimensional slices along any direction for visualization. It can compute color maps of the internal
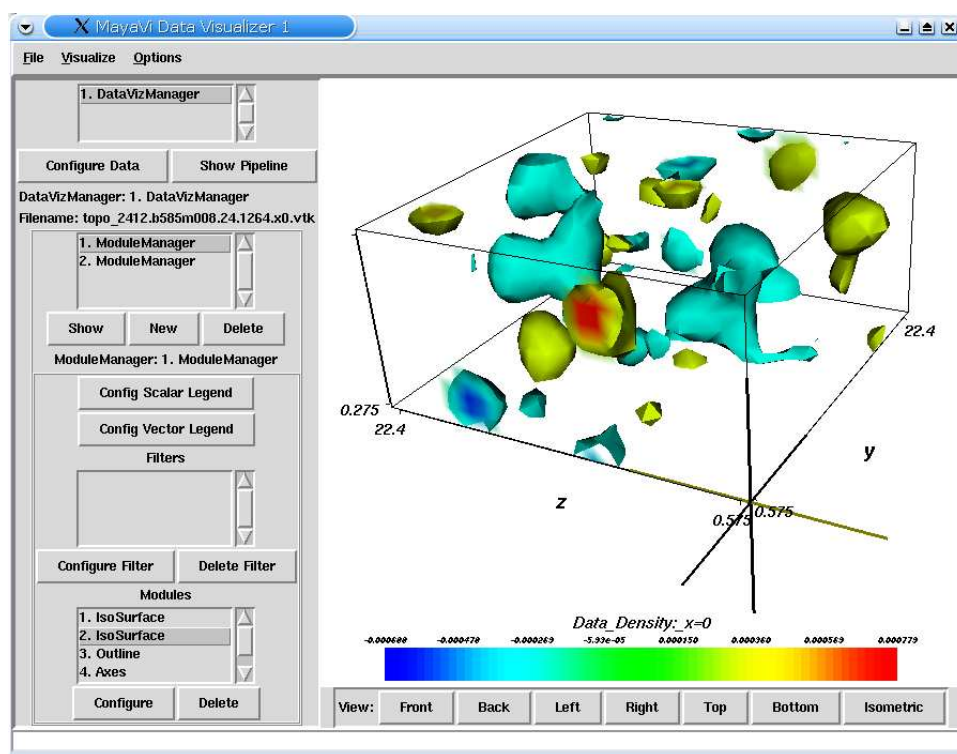
Figure 8.1: Screen capture of the MayaVi visualizer with isosurfaces of constant topological charge and color maps of internal structure displayed.

structure of the cutout objects at the lattice boundaries, as is shown in Figure 8.1.

Because lattice data is four dimensional, we developed a method to automatically generate a table with three-dimensional slices of an entire lattice in HTML format. It is done by controlling the MayaVi object directly through code and requires no user interaction besides the choice of global parameters. This allows for quick study of the structure of an entire lattice (instead of viewing only one slice at a time), and because the format is easy to view in any browser, it provides an easy way to share the information with collaborators. This kind of task is easy with a language such as Python with extensions for HTML generation, but would be fairly cumbersome in other languages like C or FORTRAN.

8.2 Artificial Instantons

In the previous chapter we have already used the results from our visualization tool, so we will not repeat that here. We will however illustrate an additional possibility it offers by looking at a simple example which is interesting for physical reasons, that of artificial instantons.

Figure 8.2 shows a configuration where two instantons and two anti-instantons have been manually constructed and aligned along a diagonal. The top image is one of our usual isosurface representations, while the bottom image shows the topological charge rendered as a translucent volume. Volume rendering is computationally very expensive, because the image must be computed by following light rays throughout the entire dataset taking into account the values of the data and mapping them to a table of transparency values. This requires manual definition of an opacity function. While for most of our work we have used isosurface calculations, it was very straightforward to add this capability to the code because the VTK toolkit already has builtin volume renderers. The entire volume rendering code is about 250 lines of Python.

These artificial configurations are physically interesting if we contrast them
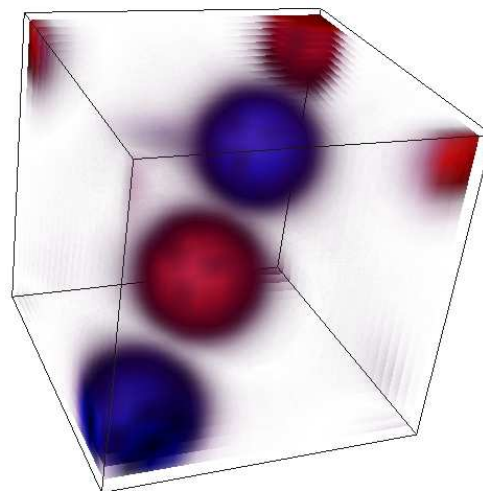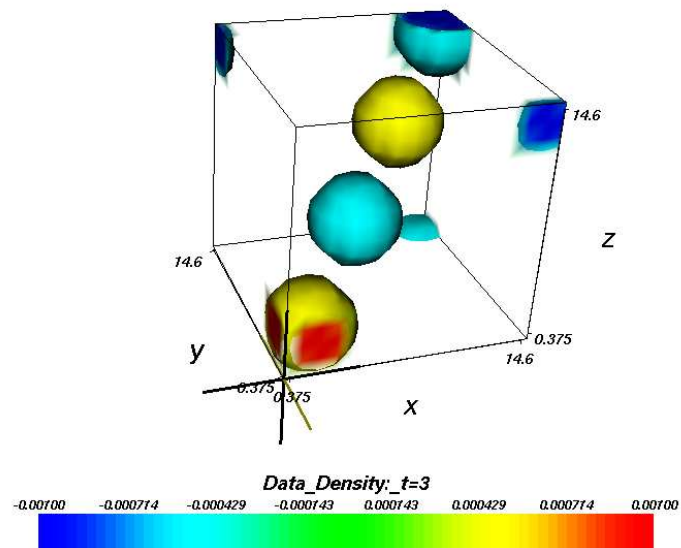
Figure 8.2: Artificial instanton configuration, displayed as isosurfaces of constant topological charge (top) and as a translucent volume with a suitably defined opacity function (bottom).

with the images we have been working with of real lattices. Most models (including our own simple correlation one) work on the assumption that the objects in the QCD vacuum look like the configuration from Figure 8.2. As we have seen, the reality of lattice structure is far noisier and less structured than this. It should then come as no surprise that identifying phenomenological quantities from instanton models is a difficult proposition, to say the least.

8.3   The Relation Between Topological and Fermionic Observables

We will conclude this chapter by considering the connection between the topological background and the fermionic eigenmodes of the Dirac operator. We have already discussed this connection before, and it can be quantitatively studied by considering the proper correlators, which we will not go into. But it is instructive to perform a visual analysis with our tools to gain some intuition into the behavior of these quantities.

In Figure 8.3 we present the topological density for a particular dynamical configuration with $\beta = 6.1$. Six slices taken at $x = 0$, 3, 6, 9, 12 and 15 are shown. As we have discussed, the Dirac operator has exact chiral zero modes on isolated (anti) instantons. In the presence of nearby instanton–anti-instanton structures these exact zero modes will split into conjugate pairs with non-zero eigenvalues. For this particular configuration, professor Tom DeGrand gave us a dataset with the lowest 5 fermionic eigenmodes of the Dirac operator, the first two of which are chiral.

Our visualization code has been adapted to also analyze the structure of fermionic eigenmodes. The raw data contains the scalars $\langle \bar{\psi}(\gamma_5 + 1)\psi \rangle$ and $\langle \bar{\psi}(\gamma_5 - 1)\psi \rangle$, from which we can compute the densities $\langle \bar{\psi}\psi \rangle$ and $\langle \bar{\psi}\gamma_5\psi \rangle$.

Modes 0 and 1, shown in Figures 8.4 and 8.5, are both chiral (they both have $\langle \bar{\psi}(\gamma_5 - 1)\psi \rangle = 0$). Modes 2, 3 and 4, shown in Figures 8.6, 8.7 and 8.8 are not chiral.

By comparing these figures to the gauge background, we can in fact confirm
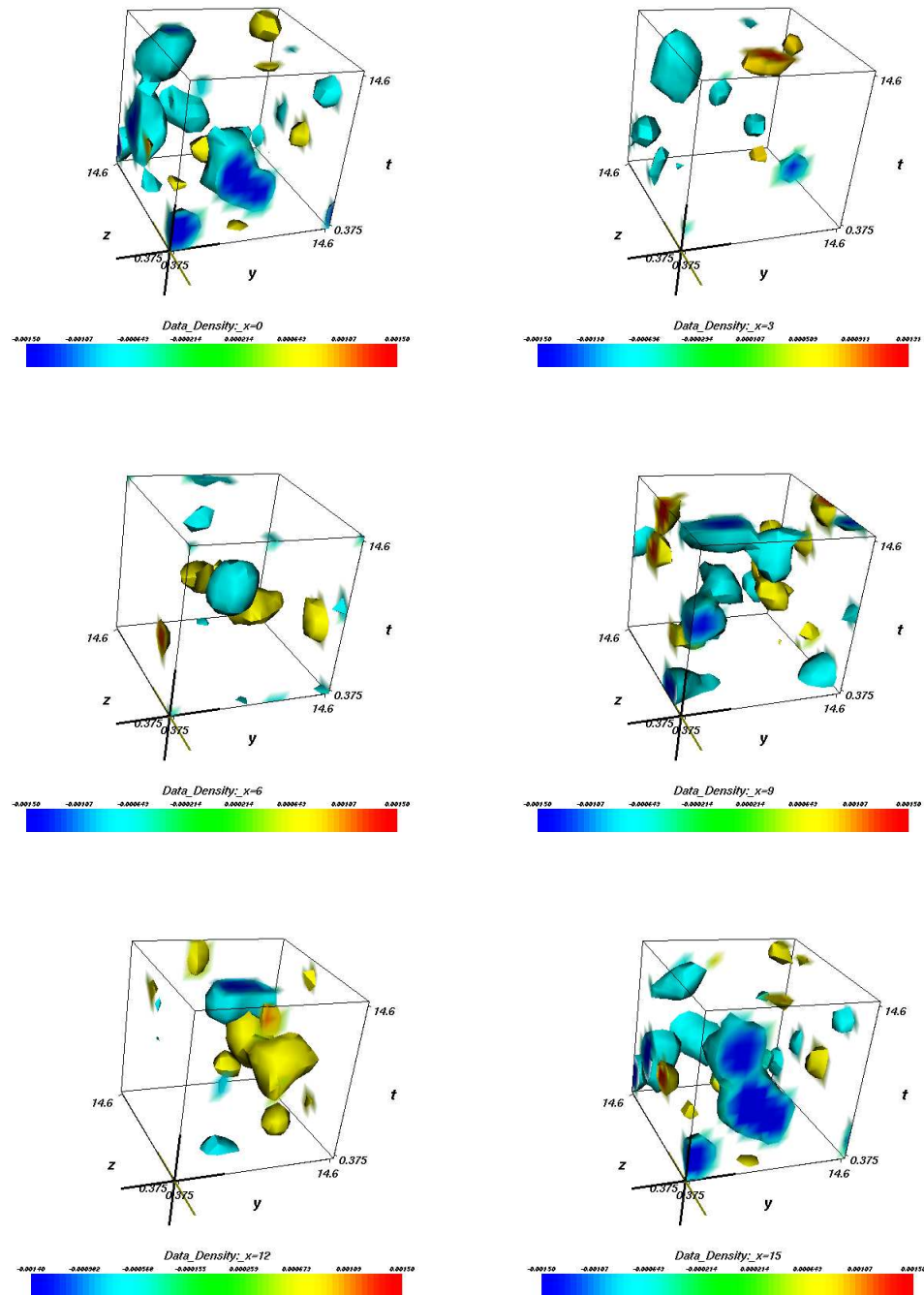
Figure 8.3: Topological charge density for a 16^4 lattice with $\beta = 6.1$, after 18 steps of APE blocking. Slices taken at $x = 0$, 3, 6, 9, 12 and 15.

that the various eigenmodes are strongly localized around the significant features of the gauge fields. While any individual fermionic mode is free to couple more or less strongly to any particular instanton, in general we find that the eigenmodes do not localize in areas with no significant gauge background. This kind of analysis can be a useful tool when trying to understand and optimize the chiral properties of various fermionic actions, an important topic of much current research.
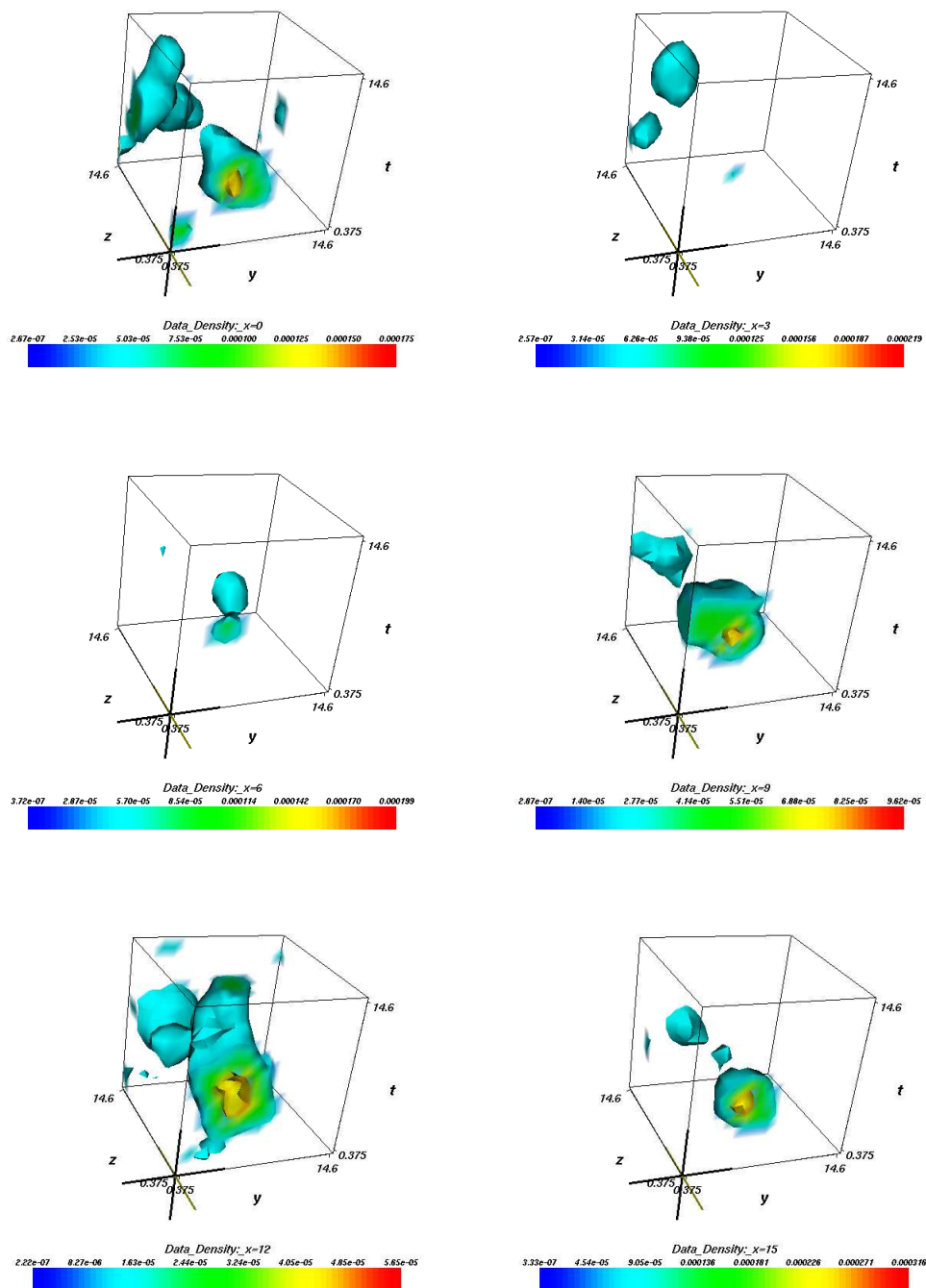
Figure 8.4: $\langle \bar{\psi}\psi \rangle$ for eigenmode 0.
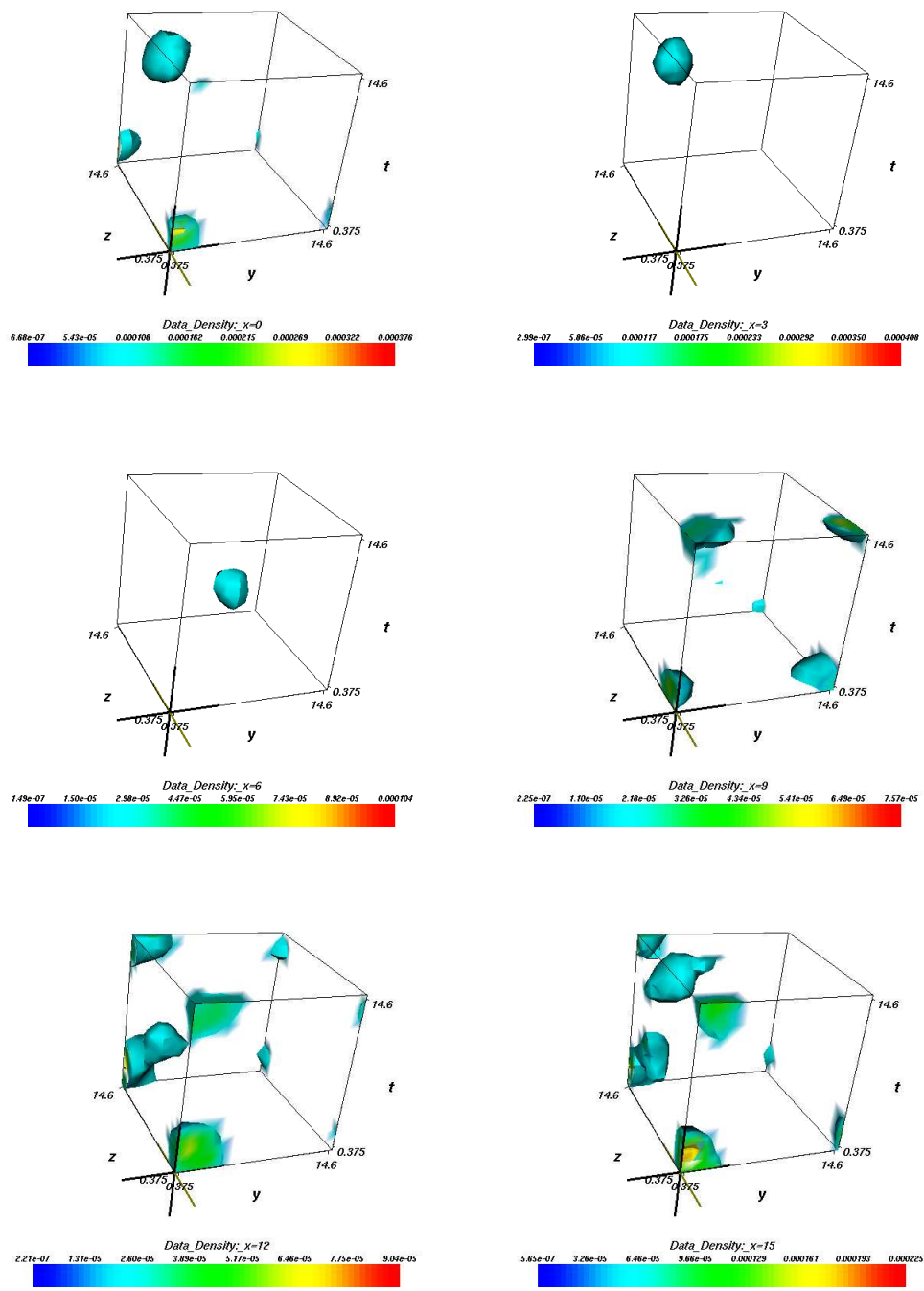
Figure 8.5: $\langle \bar{\psi}\psi \rangle$ for eigenmode 1.
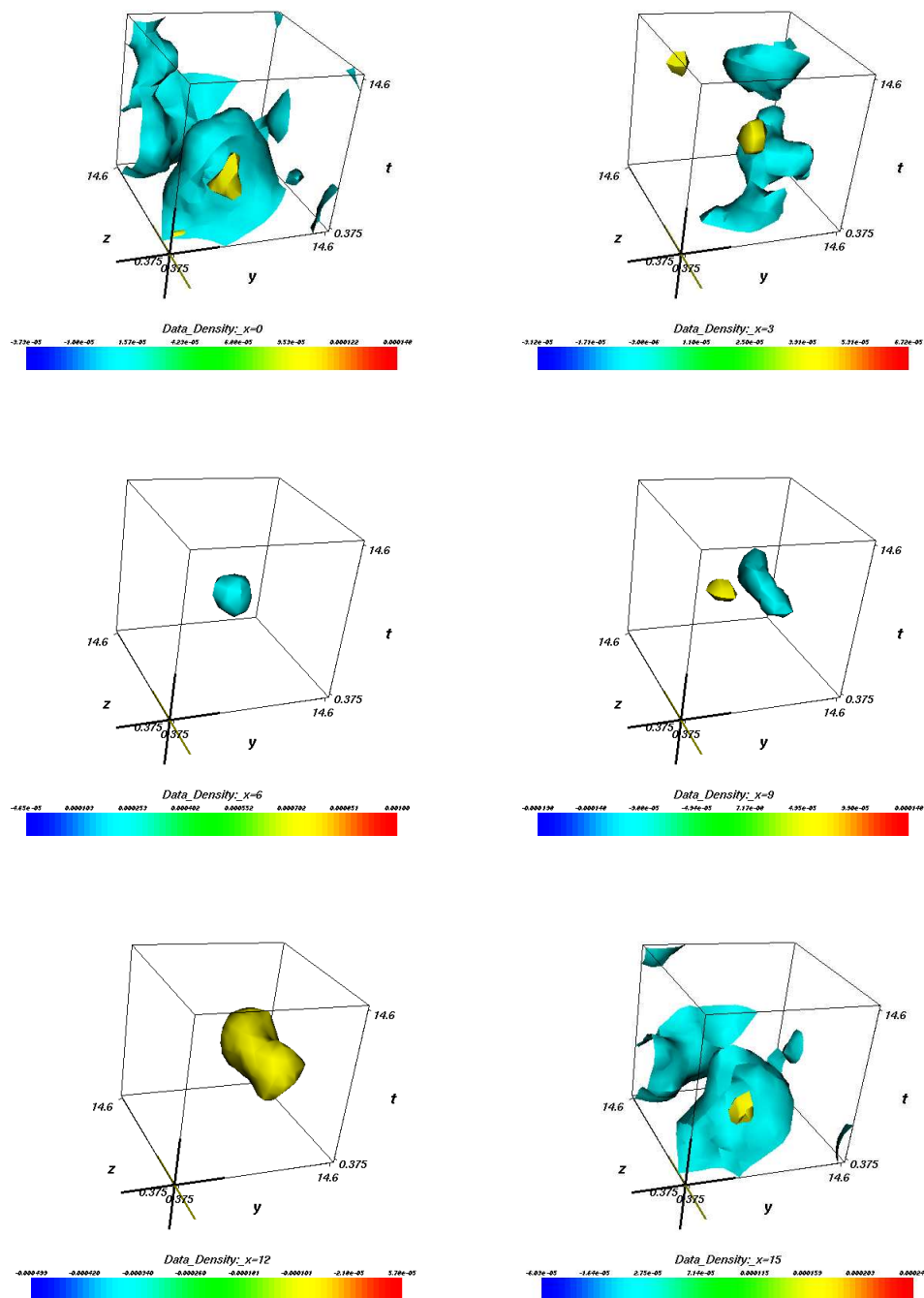
Figure 8.6: $\langle \bar{\psi}\psi \rangle$ for eigenmode 2.
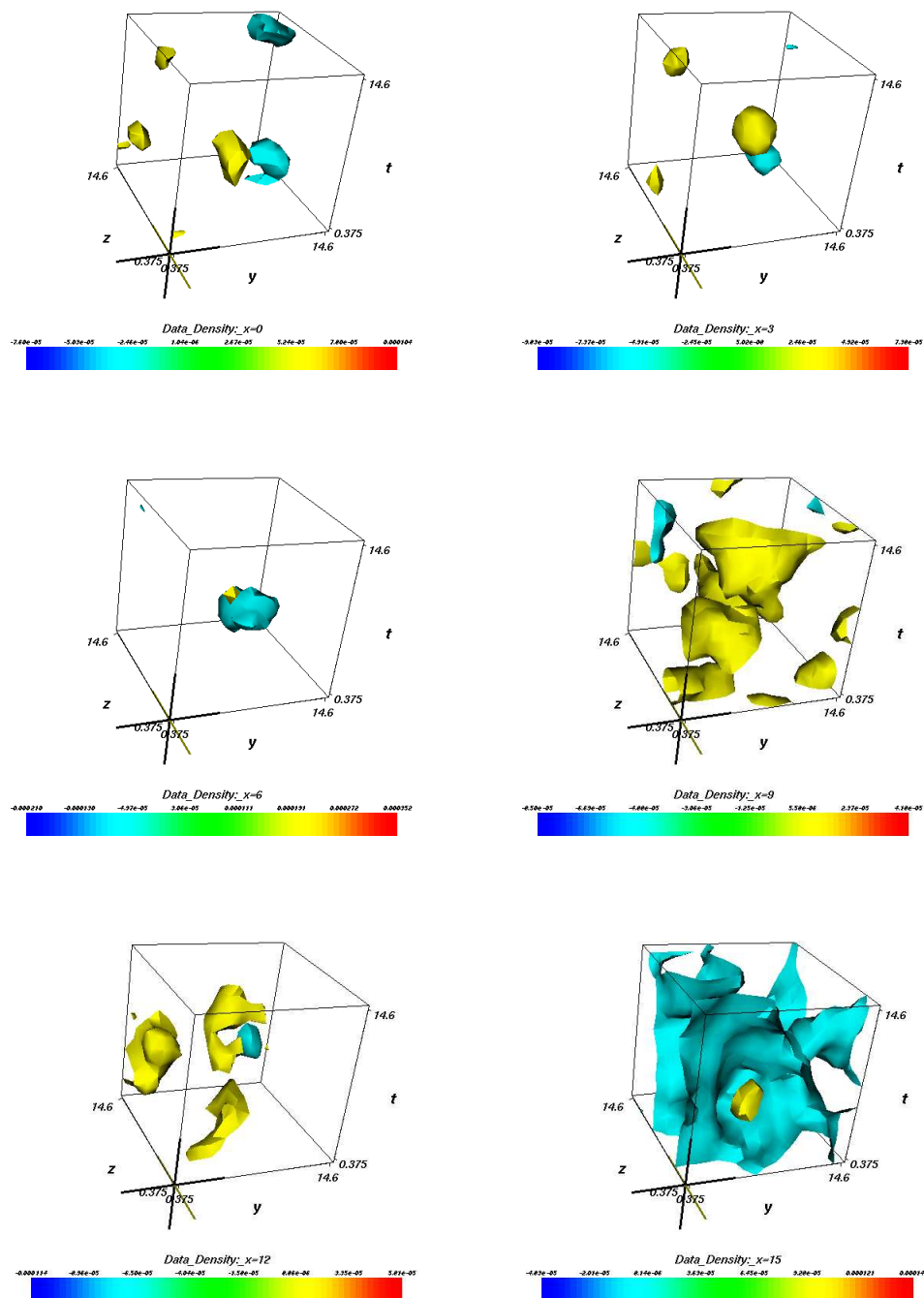
Figure 8.7: $\langle \bar{\psi}\psi \rangle$ for eigenmode 3.
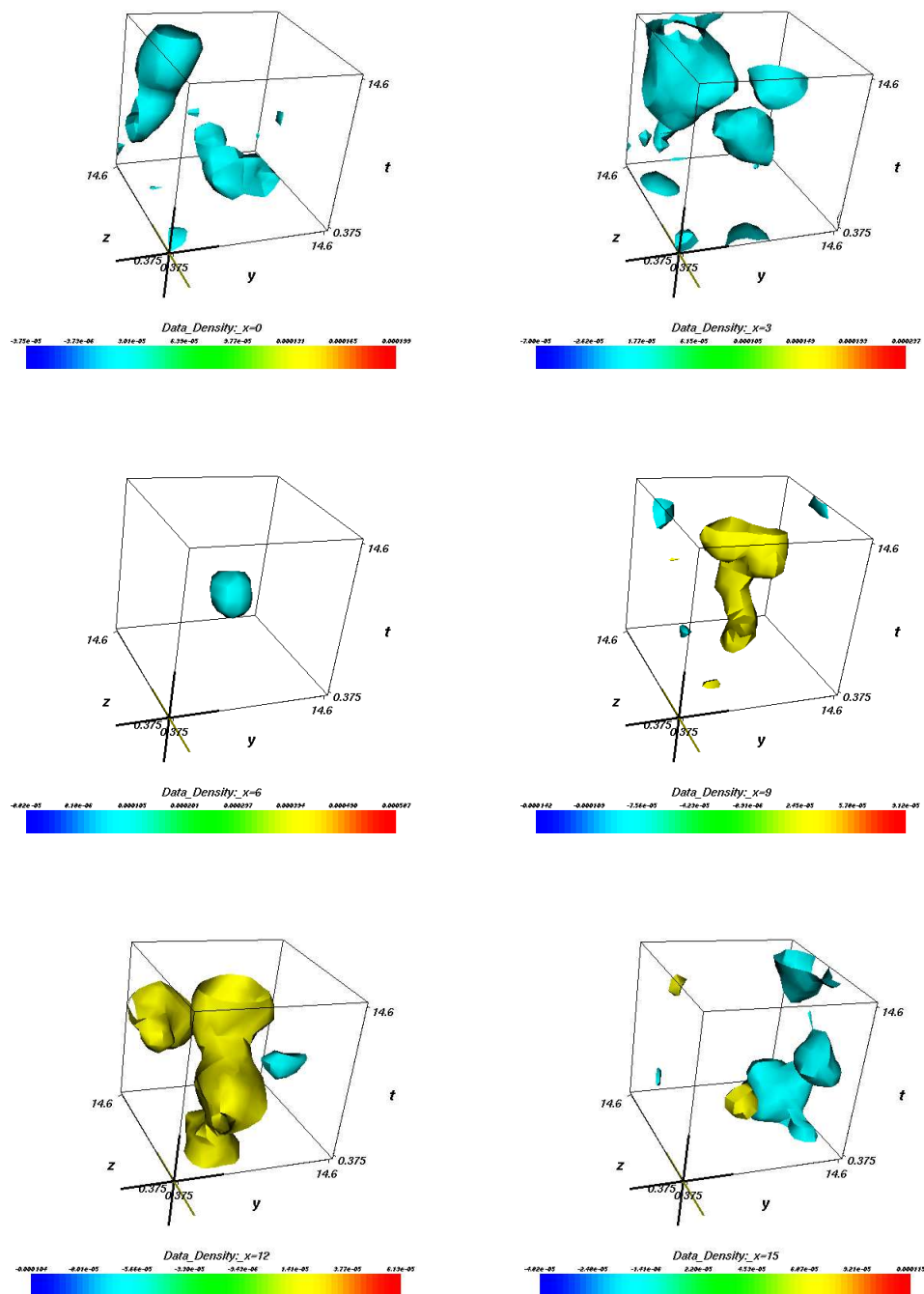
Figure 8.8: $\langle \bar{\psi}\psi \rangle$ for eigenmode 4.

Chapter 9

Summary and Outlook

We have completed a detailed study of the topological charge auto-correlation in the finite temperature QCD vacuum. What have we learned? Well, we can safely affirm that there is indeed a pair formation effect which is present in dynamical configurations and absent in quenched simulations. Furthermore, this effect is indeed anisotropic and dependent on the temperature. This is one more piece of evidence to add to the puzzle of the mechanisms of the QCD phase transition: instanton-fermion driven effects do appear to be an ingredient of the problem, and they do persist through the transition.

However, we have also seen that this effect is mild and difficult to quantify. The intuitive picture presented by Shuryak and others is appealing and has a direct connection with artificially constructed phenomenological models. On the other hand, we have seen that the actual QCD vacuum is a complex, extremely noisy environment. The BPST instanton is an isolated, free space solution, and we have seen that the lattice QCD vacuum has a lot of topological structures whose form goes beyond that of the instanton solution. Instanton physics is here to stay, but we have still much to learn about these objects.

We must also caution that the lattice set we analyzed appears to have worse auto-correlation problems than we initially expected with respect to its topological properties. Obtaining properly decorrelated configuration with respect to topological properties is very expensive computationally. We are currently studying in more

detail this issue, but it appears that for a proper study of topological effects, much more careful attention needs to be paid to autocorrelation issues than has been done in the past.

Our approach has been limited and we should try to construct a more detailed description which can quantify the pairing effect correctly across the entire lattice. We have in fact been working on such a model, but it has proven difficult to obtain stable fits to the data with it and we must refine it further before conclusions can be drawn from it.

It is also possible that these simulations are using a quark mass which is too heavy and therefore suppresses the effects. Until dynamical simulations can be performed with lighter quark masses and a similar analysis can be repeated, we will have to wait for the answer to this question.

The thermodynamics of QCD is a fascinating problem and we are starting to obtain experimental data in this regime from the RHIC experiments ([52], [74]). It is certainly far too optimistic to expect lattice calculations to be able to describe the details of an environment as complex as a violent heavy ion collision, but it is still instructive to learn as much as possible about the broad thermodynamic properties of this regime. We have mounting evidence that instantons (or more broadly speaking, instanton-like topological structures) play a role in this problem.

Furthermore, it seems clear that dynamical simulations are needed to understand the behavior of QCD in these regimes, as critical details are missed by the quenched approximation.

Finally, the development of flexible, easy to use visualization tools is a useful addition to a lattice physicist's toolbox. While these kinds of visual studies will never in and of themselves provide ultimate quantitative answers, they can be useful in building an understanding of this complex environment and guiding one's intuition.

Bibliography

[1] M. Albanese et al., *Glueball masses and string tension in lattice QCD*, Phys. Lett. **B192** (1987), 163.

[2] S. Aoki et al., *Phase structure of lattice QCD at finite temperature for 2+1 flavors of Kogut-Susskind quarks*, Nucl. Phys. Proc. Suppl. **73** (1999), 459–461, e-print: `hep-lat/9809102`.

[3] J. Apostolakis et al., *Report of the LHC Computing Grid Project-Architecture Blueprint RTAG*, Tech. report, CERN, 2002, URL `http://lcgapp.cern.ch/project/blueprint/BlueprintReport-final.doc`.

[4] D. Ascher et al., *Numerical Python*, URL `http://www.pfdubois.com/numpy`.

[5] T. Banks and A. Casher, *Chiral Symmetry Breaking in Confining Theories*, Nucl. Phys. **B169** (1980), 103.

[6] D. Beazley, *SWIG – Simplified Wrapper and Interface Generator*, URL `http://www.swig.org`.

[7] D. Beazley, *Feeding a Large-scale Physics Application to Python*, Python International Conference, 1997, URL `http://www.python.org/workshops/1997-10/proceedings/beazley.html`.

[8] A.A. Belavin, A.M. Polyakov, A.S. Shvarts, and Y.S. Tyupkin, *Pseudoparticle solutions of the Yang-Mills equations*, Phys. Lett. **B59** (1975), 85–87.

[9] B. Berg, *Dislocations and topological background in the lattice O(3) sigma model*, Phys. Lett. **B104** (1981), 475.

[10] C.W. Bernard et al., *Two-flavor staggered fermion thermodynamics at $N_t = 12$*, Phys. Rev. **D54** (1996), 4585–4594, e-print: `hep-lat/9605028`.

[11] K.M. Bitar and S.J. Chang, *Vacuum Tunneling of Gauge Theory in Minkowski Space*, Phys. Rev. **D17** (1978), 486.

[12] F.D.R. Bonnet, D.B. Leinweber, A.G. Williams, and J.M. Zanotti, *Improved smoothing algorithms for lattice gauge theory*, (2001), e-print: `hep-lat/0106023`.

[13] R. Bott, *An application of the Morse theory to the topology of Lie-groups*, Bull. Soc. Math. France **84** (1956), 251–281. MR 19,291a

[14] A. Chodos, R.L. Jaffe, K. Johnson, C.B. Thorn, and V.F. Weisskopf, *A new extended model of hadrons*, Phys. Rev. **D9** (1974), 3471–3495.

[15] S.R. Coleman, *The Uses of Instantons*, Instantons in Gauge Theories (M. Shifman, ed.), World Scientific, 1994, Lecture delivered at 1977 Int. School of Subnuclear Physics, Erice, Italy, Jul 23-Aug 10, 1977, p. 382.

[16] N. Cundy, M. Teper, and U. Wenger, *Instantons and chiral symmetry breaking in SU(N) gauge theories*, (2002), e-print: `hep-lat/0209104`.

[17] N. Cundy, M. Teper, and U. Wenger, *Topology and chiral symmetry breaking in SU(N(c)) gauge theories*, (2002), e-print: `hep-lat/0203030`.

[18] C. Davies, *Lattice QCD*, (2002), e-print: `hep-ph/0205181`.

[19] P. de Forcrand, M. Garcia Perez, J.E. Hetrick, and I.O. Stamatescu, *Topological properties of the QCD vacuum at $T = O$ and $T \approx T_c$*, (1997), e-print: `hep-lat/9802017`.

[20] T. DeGrand, A. Hasenfratz, P. Hasenfratz, P. Kunszt, and F. Niedermayer, *Fixed-point action for fermions in QCD*, Nucl. Phys. Proc. Suppl. **53** (1997), 942–944, e-print: `hep-lat/9608056`.

[21] T. DeGrand, R.L. Jaffe, K. Johnson, and J.E. Kiskis, *Masses and other parameters of the light hadrons*, Phys. Rev. **D12** (1975), 2060.

[22] T. DeGrand, *Nonperturbative quantum field theory on the lattice*, (1996), e-print: `hep-th/9610132`.

[23] T. DeGrand, A. Hasenfratz, P. Hasenfratz, and F. Niedermayer, *The Classically perfect fixed point action for SU(3) gauge theory*, Nucl. Phys. **B454** (1995), 587–614, e-print: `hep-lat/9506030`.

[24] T. DeGrand, A. Hasenfratz, P. Hasenfratz, and F. Niedermayer, *Fixed point actions for SU(3) gauge theory*, Phys. Lett. **B365** (1996), 233–238, e-print: `hep-lat/9508024`.

[25] T. DeGrand, A. Hasenfratz, and T.G. Kovacs, *Topological structure in the SU(2) vacuum*, Nucl. Phys. **B505** (1997), 417–441, e-print: `hep-lat/9705009`.

[26] T. DeGrand, A. Hasenfratz, and T.G. Kovacs, *Revealing topological structure in the SU(2) vacuum*, Nucl. Phys. **B520** (1998), 301–322, e-print: `hep-lat/9711032`.

[27] C. DeTar, *Quark-Gluon Plasma in Numerical Simulations of Lattice QCD*, Quark Gluon Plasma 2 (R.C. Hwa, ed.), World Scientific, Singapore, 1995, p. 784.

[28] D. Diakonov, *Chiral-symmetry breaking by instantons*, (1995), e-print: `hep-ph/9602375`.

[29] S. Duane, *Stochastic quantization versus the microcanonical ensemble: getting the best of both worlds*, Nucl. Phys. **B257** (1985), 652.

[30] M. Falcioni, M.L. Paciello, G. Parisi, and B. Taglienti, *Again on SU(3) glueball mass*, Nucl. Phys. **B251** (1985), 624–632.

[31] Z. Fodor, *Lattice QCD Results at Finite Temperature and Density*, (2002), e-print: `hep-lat/0209101`.

[32] P.H. Ginsparg and K.G. Wilson, *A remnant of chiral symmetry on the lattice*, Phys. Rev. **D25** (1982), 2649.

[33] W. Greiner and A. Schaefer, *Quantum chromodynamics*, Springer, 1994.

[34] R. Gupta, *Introduction to lattice QCD*, (1997), e-print: `hep-lat/9807028`.

[35] A. Hasenfratz and F. Knechtli, *The phase diagram of QCD with two and four flavors: Results with HYP fermions*, Nucl. Phys. Proc. Suppl. **106** (2002), 432–434, e-print: `hep-lat/0202019`.

[36] A. Hasenfratz and F. Knechtli, *Simulating dynamical fermions with smeared links*, Nucl. Phys. Proc. Suppl. **106** (2002), 1058–1060, e-print: `hep-lat/0110156`.

[37] A. Hasenfratz, *Spatial correlation of the topological charge in pure SU(3) gauge theory and in QCD*, Phys. Lett. **B476** (2000), 188–192, e-print: `hep-lat/9912053`.

[38] A. Hasenfratz and F. Knechtli, *Flavor symmetry and the static potential with hypercubic blocking*, Phys. Rev. **D64** (2001), 034504, e-print: `hep-lat/0103029`.

[39] A. Hasenfratz and F. Knechtli, *Four flavor finite temperature phase transition with HYP action: Where is the first order endpoint?*, (2001), e-print: `hep-lat/0105022`.

[40] A. Hasenfratz and F. Knechtli, *Simulation of dynamical fermions with smeared links*, Comput. Phys. Commun. **148** (2002), 81–86, e-print: `hep-lat/0203010`.

[41] A. Hasenfratz and C. Nieter, *Instanton content of the SU(3) vacuum*, Phys. Lett. **B439** (1998), 366–372, e-print: `hep-lat/9806026`.

[42] P. Hasenfratz and F. Niedermayer, *Perfect lattice action for asymptotically free theories*, Nucl. Phys. **B414** (1994), 785–814, e-print: `hep-lat/9308004`.

[43] P. Hasenfratz, *The theoretical background and properties of perfect actions*, (1998), e-print: `hep-lat/9803027`.

[44] E.M. Ilgenfritz, M.L. Laursen, G. Schierholz, M. Muller-Preussker, and H. Schiller, *first evidence for the existence of instantons in the quantized SU(2) lattice vacuum*, Nucl. Phys. **B268** (1986), 693.

[45] E.M. Ilgenfritz and E.V. Shuryak, *Chiral symmetry restoration at finite temperature in the instanton liquid*, Nucl. Phys. **B319** (1989), 511.

[46] E.M. Ilgenfritz and E.V. Shuryak, *Quark induced correlations between instantons drive the chiral phase transition*, Phys. Lett. **B325** (1994), 263–266, e-print: `hep-ph/9401285`.

[47] Y. Iwasaki, K. Kanaya, S. Kaya, S. Sakai, and T. Yoshie, *Finite temperature transitions in lattice QCD with Wilson quarks: Chiral transitions and the influence of the strange quark*, Phys. Rev. **D54** (1996), 7010–7031, e-print: `hep-lat/9605030`.

[48] E. Jones et al., *SciPy – Scientific tools for Python*, URL `http://scipy.org`.

[49] F. Karsch, *Lattice QCD at high temperature and density*, (2001), e-print: `hep-lat/0106019`.

[50] F. Karsch, *Lattice results on QCD thermodynamics*, Nucl. Phys. **A698** (2002), 199–208, e-print: `hep-ph/0103314`.

[51] F. Knechtli and A. Hasenfratz, *Dynamical fermions with fat links*, Phys. Rev. **D63** (2001), 114502, e-print: `hep-lat/0012022`.

[52] J.B. Kogut, *QCD in Extreme Environments*, (2002), e-print: `hep-lat/0208077`.

[53] H. Leutwyler and A. Smilga, *Spectrum of Dirac operator and role of winding number in QCD*, Phys. Rev. **D46** (1992), 5607–5632.

[54] M. Luscher, *Topology of lattice gauge fields*, Commun. Math. Phys. **85** (1982), 39.

[55] J.W. Negele, *Understanding hadron structure using lattice QCD*, Nucl. Phys. **A699** (2002), 18–25, e-print: `hep-lat/0107010`.

[56] C. Nieter, *Instantons and Chiral Symmetry on the Lattice*, Ph.D. thesis, University of Colorado, Boulder, 1999.

[57] M. Ninomiya, *No Go theorem for lattice chiral fermions. (Talk)*, (1981), In *Tokyo 1981, Proceedings, Quark and Lepton Physics*, 124- 127.

[58] R.K. Pathria, *Statistical Mechanics*, second ed., Butterworth Heinemann, 1996.

[59] M.E. Peskin and D.V. Schroeder, *An introduction to Quantum Field Theory*, Addison Wesley, 1995.

[60] P. Peterson, *F2PY – Fortran to Python interface generator*, URL `http://cens.ioc.ee/projects/f2py2e`.

[61] A. Phillips and D. Stone, *Lattice gauge fields, principal bundles and the calculation of topological charge*, Commun. Math. Phys. **103** (1986), 599–636.

[62] R.D. Pisarski and F. Wilczek, *Remarks on the chiral phase transition in chromodynamics*, Phys. Rev. **D29** (1984), 338–341.

[63] A.M. Polyakov, *Compact gauge fields and the infrared catastrophe*, Phys. Lett. **B59** (1975), 82–84.

[64] F. Pérez, *IPython – An enhanced Interactive Python shell*, URL `http://www-hep.colorado.edu/ fperez/ipython`.

[65] P. Ramachandran, *The MayaVi Data Visualizer*, URL `http://mayavi.sourceforge.net`.

[66] H.J. Rothe, *Lattice Gauge Theories, an Introduction.*, 2nd ed., World Scientific Lecture Notes in Physics, vol. 59, World Scientific, 1997.

[67] J. Sakurai, *Modern Quantum Mechanics*, Addison Wesley, 1994.

[68] T. Schafer and E.V. Shuryak, *Interacting instanton liquid in QCD at zero and finite temperature*, Phys. Rev. **D53** (1996), 6522–6542, e-print: `hep-ph/9509337`.

[69] T. Schafer and E.V. Shuryak, *Instantons in QCD*, Rev. Mod. Phys. **70** (1998), 323–426, e-print: `hep-ph/9610451`.

[70] T. Schafer, E.V. Shuryak, and J.J.M. Verbaarschot, *The Chiral phase transition and instanton - anti-instanton molecules*, Phys. Rev. **D51** (1995), 1267–1281, e-print: `hep-ph/9406210`.

[71] W.J. Schroeder, K.M. Martin, L.S. Avila, and C. Law, *The Visualization Toolkit User's Guide, Version 4.0*, Kitware, Inc., 2001.

[72] B. Sheikholeslami and R. Wohlert, *Improved continuum limit lattice action for QCD with Wilson fermions*, Nucl. Phys. **B259** (1985), 572.

[73] M.A. Shifman (ed.), *Instantons in Gauge Theories*, World Scientific, 1994.

[74] E. Shuryak, *How the quantum mechanics of the Yang-Mills fields may help us understand the RHIC puzzles*, (2002), e-print: `hep-ph/0205031`.

[75] E.V. Shuryak, *Why is a nucleon bound?*, Nucl. Phys. **A606** (1996), 201–214, e-print: `hep-ph/9603354`.

[76] E.V. Shuryak and M. Velkovsky, *The Instanton density at finite temperatures*, Phys. Rev. **D50** (1994), 3323–3327, e-print: `hep-ph/9403381`.

[77] E.V. Shuryak and J.J.M. Verbaarschot, *QCD instantons at finite temperature. 1. Gluonic interactions and the fermion determinant*, Nucl. Phys. **B364** (1991), 255–282.

[78] G. 't Hooft, *Computation of the quantum effects due to a four-dimensional pseudoparticle*, Phys. Rev. **D14** (1976), 3432–3450.

[79] G. 't Hooft, *Symmetry breaking through Bell-Jackiw anomalies*, Phys. Rev. Lett. **37** (1976), 8–11.

[80] M. Teper, *Instantons in the quantized SU(2) vacuum: a lattice Monte Carlo investigation*, Phys. Lett. **B162** (1985), 357.

[81] A.I. Vainshtein, V.I. Zakharov, V.A. Novikov, and M.A. Shifman, *ABC of instantons*, Sov. Phys. Usp. **24** (1982), 195.

[82] G. van Rossum, *The Python Programming Language*, URL `http://www.python.org`.

[83] M. Velkovsky and E.V. Shuryak, *A Mean Field Approach To The Instanton-Induced Effect Close To The QCD Phase Transition*, Phys. Rev. **D56** (1997), 2766–2777, e-print: `hep-ph/9603234`.

[84] M. Velkovsky and E.V. Shuryak, *QCD with large number of quarks: Effects of the instanton anti-instanton pairs*, Phys. Lett. **B437** (1998), 398–402, e-print: `hep-ph/9703345`.

[85] K.G. Wilson, *Renormalization group and critical phenomena. 1. Renormalization group and the Kadanoff scaling picture*, Phys. Rev. **B4** (1971), 3174–3183.

[86] K.G. Wilson, *Renormalization group and critical phenomena. 2. Phase space cell analysis of critical behavior*, Phys. Rev. **B4** (1971), 3184–3205.

[87] K.G. Wilson, *Confinement of quarks*, Phys. Rev. **D10** (1974), 2445–2459.